Exploring the dynamics of blocking TDP-43 SUMOylation during cellular stress and recovery

Jenny Zhang

Thesis submitted to the University of Ottawa in partial fulfillment of the requirements for the Master's degree in Neuroscience

Department of Cellular and Molecular Medicine

Faculty of Medicine

University of Ottawa

DEDICATION

I dedicate this thesis to the entire ALS community: those living with ALS, their caregivers, and the basic scientists, clinicians, and healthcare professionals who support them. I recognize and honor the significant challenges they face and their unwavering hope, and I am deeply grateful to everyone who works tirelessly to improve the lives of those affected.

ACKNOWLEDGEMENTS

First and foremost, I would like to thank my parents, Tony Zhang and Lucy Hu, for their unwavering love and support throughout my life. Your kindness and diligence not only provided me with a solid foundation but also taught me the importance of perseverance and hard work. I would also like to express gratitude to my brothers, Justin and Jaden, whose intelligence and curiosity have inspired me throughout my academic career.

To Dr. Maxime Rousseaux, thank you for your continuous support and mentorship during my time in the lab. Your guidance has shaped me as a trainee and helped me overcome challenges as the first TMM BSc-MSc integrated student in the Rousseaux lab. I am incredibly thankful for the opportunities you have given me to learn various cool techniques and attend conferences, which have helped me grow as a scientist.

I am incredibly grateful for my mentor, Dr. Terry Suk. I have become more knowledgeable and confident in the ALS field because of your patience and constructive feedback. I appreciate the time and effort you have invested in helping me grow as a researcher, and I consider myself extremely fortunate to have had you as my mentor throughout my time in the lab. Thank you for being an inspiration and for making a lasting impact on my academic journey.

To Steve Callaghan, your efficiency and organization have been crucial in keeping our lab running smoothly. I appreciate your willingness to help with any concerns or questions and for ensuring we have the resources to carry out our research effectively.

I would like to thank Dr. Derrick Gibbings and Dr. Trinkle-Mulcahy, who served on my thesis advisory committee. Your guidance and feedback challenged me to think critically. I am also grateful to the CBIA core staff, Dr. Chloë Van Oostende-Triplet and Liyuan Wang for their

technical assistance with microscopy. I would also like to acknowledge Dr. David Taylor for his support and guidance throughout our lab's journey.

I am grateful to the entire lab team for creating a supportive and collaborative environment. Lastly, I would like to thank my friends and my partner, who have continued to celebrate and support my accomplishments.

FUNDING

I would like to express my gratitude for the funding provided by **Brain Canada** through the **ALS Rising Stars program in memory of Madeleine Blanc**. Additionally, I am deeply thankful to the **Canadian Institute of Health Research (CIHR)** for their financial support through the **Canada Graduate Scholarships-Master's (CGS-M)** program. I would also like to thank the **University of Ottawa** for their Admission and Excellence scholarships. These contributions have helped me successfully complete this project, share my work with the ALS Community at the ALS Canada and Motor Neurone Disease conferences, and grow as an early career researcher.

TABLE OF CONTENTS

ABSTRACT

Amyotrophic Lateral Sclerosis (ALS) is a fatal neurodegenerative disease in which an RNA-binding protein called TDP-43 mislocalizes and accumulates in the cytoplasm[1–3]. Increasingly, the cellular stress response is linked with ALS, whereby disruption of various stress-related pathways can lead to the aberrant accumulation of TDP-43[1,4,5]. Despite this strong connection between stress pathways and TDP-43, the exact mechanisms that act on TDP-43 remain elusive. Our lab previously found that, in response to stress, TDP-43 is modified by Small Ubiquitin-like Modifiers (SUMO) through a process called SUMOylation[6]. This modification accumulates during prolonged stress and surprisingly continues to accumulate during recovery before being cleared by the proteasome[6]. We mapped the site of SUMOylation at lysine 408 (K408) and generated a knock-in mouse model to study the consequences of blocking endogenous TDP-43 SUMOylation by mutating K408 to an arginine (R; TDP-43$^{K408R/K408R}$)[6].

In neuronal cultures, we observed that blocking TDP-43 SUMOylation delayed the clearance of G3BP1-positive stress granules and led to the accumulation of nuclear TDP-43 recovery bodies during recovery. Following repeated stress and recovery, we observed further impairment of clearance and re-activation of stress granules and the significant accumulation of nuclear TDP-43 recovery bodies during the later stress and recovery time points. We identified a subset of nuclear TDP-43 recovery bodies that co-localized with an RNA-binding motif protein called RBM-45, doing so at a higher degree in TDP-43$^{K408R/K408R}$ neurons.

To observe the contribution of SUMOylation to TDP-43 dynamics in real time, we generated HEK293T cells expressing TDP-43 tagged with mStayGold – a brighter and more photostable green fluorescent protein[7] – for live-cell imaging. Following repeated stress and recovery, we observed changes in TDP-43 localization in TDP-43$^{K408R/K408R}$ cells and alterations in TDP-43

mobility at later stress and recovery time points. Overall, our data suggests that blocking TDP-43 SUMOylation during acute stress and recovery led to dysfunctions in the cellular stress response and accumulation of nuclear TDP-43. These effects are exacerbated following repeated stress and recovery events, leading to cytoplasmic TDP-43 aggregation.

LIST OF ABBREVIATIONS

ALS	Amyotrophic Lateral Sclerosis
ANOVA	Analysis of Variance
ATXN2	Ataxin 2
CNS	Central Nervous System
CTD	C-terminal Domain
CTF	C-terminal Fragment
CRISPR	Clustered Regularly Interspaced Short Palindromic Repeats
C9ORF72	Chromosome 9 open reading frame 72
DAPI	4’,6-diamidino-2-phenylindol
DNA	Deoxyribonucleic Acid
DSB	Double-stranded Break
EGFP	Enhanced Green Fluorescent Protein
EIF2a	Eukaryotic translation initiation factor 2A
ER	Endoplasmic Reticulum
E1Fa	Human Elongation Factor 1 alpha
fALS	Familial ALS
FUS	Fused in Sarcoma

GFP	Green Fluorescent Protein
GWAS	Genome Wide Association Studies
G3BP1	G3BP Stress Granule Assembly Factor 1
HEK293T	Human Embryonic Kidney Cells
HHV	Human Herpesvirus
hnRNPs	Heterogeneous Nuclear Ribonucleoproteins
HOA	Homo-oligomerization Association
HSPA1L	Heat Shock Protein Family A Member 1 Like
HSP-70	Heat Shock Protein 70kDa
IF	Immunofluorescence
IP	Immunoprecipitation
iPSCs	Induced Pluripotent Stem Cells
ISR	Integrated Stress Response
LCD	Low Complexity Domain
LLPS	Liquid-Liquid Phase Separation
LOF	Loss-of-Function
lncRNA	Long Non-Coding RNA

MG132	Carbobenzoxy-l-leucyl-l-leucyl-1-leucinal
mRNA	Messenger RNA
mStayGold	Monomeric StayGold
NEAT1	Nuclear Enriched Abundant Transcript 1
NES	Nuclear Export Signal
NLS	Nuclear Localization Signal
NSBs	Nuclear Stress Bodies
NTD	N-terminal Domain
PARylation	Poly ADP-ribosylation
P-bodies	Processing Bodies
PML	PML Nuclear Body Scaffold
PSPC-1	Paraspeckle Component 1
PTM	Post Translational Modification
P62	Protein 62kDa (also known as SQSTM1)
RBM-45	RNA-Binding Motif 45
RNA	Ribonucleic Acid
RRM1	RNA Recognition Motif 1

RRM2	RNA Recognition Motif 2
sALS	Sporadic ALS
SENPs	Sentrin-specific Proteases
SGs	Stress Granules
SOD1	Zn/Cn Superoxide Dismutase
SQSTM1	Sequestosome 1 (p62)
STMN2	Stathmin-2
STUbLs	SUMO Targeted Ubiquitin Ligase
SUMO	Small Ubiquitin-like Modifier
TARDBP	Transactive response element DNA-binding protein of 43 kDa
TBI	Traumatic Brain Injury
TDP-43	Protein Encoded by TARDBP Gene
TIA1	Tial Cytotoxic Granule-associated RNA Binding Protein
UBC9	Ubiquitin-Conjugating Enzyme E2I
UBI-1	Ubiquitin-1
UBQLN2	Ubiquilin-2
UNC13A	Uncoordinated-13

UPS	Ubiquitin Proteosome System
UTR	3’ Untranslated Region
WB	Western Blot
WT	Wild Type

1. INTRODUCTION: AMYOTROPHIC LATERAL SCLEROSIS

1.1. Background on ALS

1.1.1. Clinical presentation and progression

Amyotrophic Lateral Sclerosis (ALS), also referred to as Lou Gehrig's disease, is a progressive and fatal neurodegenerative disease that affects approximately 1000 Canadians every year[8,9]. ALS is characterized by the gradual loss of motor neurons in the central nervous system (CNS), leading to muscle weakness, paralysis, and eventually death due to respiratory failure within 2-5 years post- diagnosis[9–12]. Loss of upper motor neurons that connect the motor cortex to the spinal cord leads to spasticity, while the loss of lower motor neurons that connect the spinal cord to the muscles leads to atrophy and fasciculations[9,13]. Despite extensive research, there is currently no cure for ALS. Existing management strategies, such as FDA-approved drugs riluzole and edaravone[14,15], are used to improve ALS symptoms and may extend survival by a few months. However, the treatment of symptoms does not halt or reverse the progression of ALS. For these reasons, a gap exists in our understanding of the pathological mechanisms underlying motor neuron degeneration, which makes it challenging to develop therapeutics that can effectively treat the disease.

1.1.2. ALS aggregates

A key pathological hallmark of almost all ALS patients (97%) is the accumulation of abnormal protein aggregates in motor neurons predominantly in the spinal cord and motor cortex[3,9,16]. These aggregates consist of misfolded and post-translationally modified proteins, such as phosphorylated and ubiquitinated TAR DNA-binding protein 43 (TDP-43), superoxide dismutase protein (SOD1), and Sequestosome 1 (SQSTM1 or p62)[1–3,17]. These cytoplasmic

inclusions in neurons can disrupt protein functions, impair protein degradation systems, and activate cellular stress pathways ultimately leading to cell death[4,18,19]. Other than ALS, protein aggregation has also been reported to lead to neuronal dysfunction in Alzheimer's disease (amyloid beta plaques)[20], and Parkinson's disease (alpha-synuclein)[21], among others.

1.2 Genetic vs Sporadic ALS

1.2.1. Genetic forms of ALS

About 10% of all cases are familial ALS (fALS) due to inherited mutations. Over the past two decades, GWAS and exome sequencing studies have identified ~30 ALS-linked genes[9,11,22,23]. The most well-known and studied include *SOD1* (Superoxide Dismutase 1), *FUS* (Fused in Sarcoma), *C9ORF72* (Chromosome 9 open reading frame 72), and *TARDBP* (Transactive response element DNA-binding protein of 43 kDa).

Among these mutations, *SOD1* was the first identified ALS-linked gene and is responsible for about 12% of fALS cases and 1-2% of sALS cases[24]. This form of ALS presents with the formation of *SOD1* protein aggregates without the ubiquitinated TDP-43 protein[25]. Mutations in *FUS*, an RNA binding protein, cause about 4% of fALS and 1% of sALS cases[24,25]. Similar to *SOD1* mutations, *FUS* mutations do not present with TDP-43 pathology, instead, FUS is found to aggregate in the cytoplasm. Moreover, *C9ORF72* is the most common genetic cause of ALS and accounts for approximately 40% of fALS and 7% of sALS[24,26,27]. Mutations in *C9ORF72* consist of a hexanucleotide repeat expansion, which leads to the formation of toxic RNA foci and dipeptide repeat proteins[27–30]. Finally, mutations in *TARDBP* gene, encoding for the protein TDP-43, accounts for 4% of fALS and 1% of sALS cases. TDP-43 pathology is characterized by the loss of TDP-43 RNA-binding in the nucleus and the accumulation of TDP-43 aggregates in the

cytoplasm[24,31–33]. Collectively, these mutations have been shown to converge on common pathways such as cellular stress response, DNA damage, and nucleoplasmic shuttling which provides insight into key pathways implicated in disease[23,24,34].

1.2.2. Sporadic forms of ALS

Unlike fALS, the cause of sALS that accounts for the majority (~90%) of ALS cases remains unclear. While there is no direct evidence linking the environment with ALS, studies have proposed several environmental risk factors that may be associated with the onset and progression of sALS.

Epidemiological studies have shown that intense physical activity is linked to a higher risk of developing ALS. Specifically, professional athletes involved in high-contact sports like football, soccer and military personnel are diagnosed with ALS more frequently[35–37]. In addition, there are proposed links between individuals who have experienced traumatic brain injuries (TBIs) with the risk to develop ALS[38,39].

Exposure to heavy metals such as lead, mercury, arsenic, iron, and selenium have been correlated with an increased risk of developing ALS[40]. Environmental toxins like pesticides and chemicals have also been correlated with disease[41]. Additionally, studies found that viral infections of enterovirus D8, Human Herpesvirus 6 (HHV-6), and Human Herpesvirus 8 (HHV-8) are present in the spinal cords of patients diagnosed with ALS[42–45].

Therefore, ALS is a highly heterogeneous disease where the accumulation of genetic predisposition, environmental factors, and aging-related stressors contribute to disease pathogenesis. Thus, exploring genes and proteins involved in sALS and fALS will provide insight into molecular mechanisms underlying ALS.

2. MOLECULAR MECHANISMS IN ALS: TDP-43 PATHOLOGY

2.1. TDP-43: Structure and Function as an RNA-binding Protein

TDP-43, encoded by the *TARDBP* gene, is a conserved and ubiquitously expressed nuclear RNA/DNA binding protein that is essential for mRNA processing, splicing, nucleocytoplasmic transport, and translational regulation[46–48]. Among these various functions, TDP-43 plays a predominant role in the suppression of cryptic exon inclusions during RNA splicing[49]. With TDP-43 depleted in the nucleus, cryptic exons become included in mRNA leading to truncated or no protein production. For example, studies have shown that the loss of TDP-43 function in neurons and induced pluripotent stem cells (iPSCs) causes cryptic mis-splicing in *UNC13A,* causing the downregulation of UNC13A protein[50,51]. Interestingly, patients with *UNC13A* Single Nucleotide Polymorphisms (SNPs) can exacerbate cryptic exon inclusion upon TDP-43 loss-of-function (LOF). Similarly, TDP-43 LOF can lead to the inclusion of *STMN2* cryptic exon in neurons which has been shown to compromise neuronal growth and function[52,53]. TDP-43 also regulates its own expression by binding to the 3' untranslated region (UTR) to repress cryptic exon inclusion to maintain protein levels and prevent the production of aberrant transcripts[54]. When this feedback loop is dysregulated, too little or excessive TDP-43 can be produced, which can drive TDP-43 pathology. Although TDP-43 is primarily nuclear, it is also present in the cytoplasm and mitochondria to regulate the stability of mRNA, autophagy, and mitochondrial function[55].

As seen in figure 1, TDP-43 is a protein of 414-amino acids with a globular N-terminal domain (NTD), two-folded RNA recognition motifs (RRM1 and RRM2), a bipartite nuclear localization sequence (NLS) adjacent to the first RNA recognition motif, a nuclear export signal (NES), and an unstructured C-terminal domain (CTD)[56]. The N-terminal domain facilitates protein-protein interactions and plays a role in TDP-43 oligomerization[57]. The two RNA-binding

domains, RRM1 and RRM2, mediate high-affinity binding to UG-rich and TG-rich motifs of RNA and DNA sequences. The NLS and NES are critical for shuttling TDP-43 between the nucleus and cytoplasm[48,58]. The CTD is a low complexity domain (LCD) that is intrinsically disordered and required for splicing and interaction with other proteins such as hnRNPs, UBQLN2, and FUS[59,60]. This domain can form beta-sheet structures which are characteristic of pathogenic aggregation. Remarkably, all known human mutations in TDP-43 that cause fALS (i.e., Q331K mutation) are found within the CTD[61]. Thus, these CTD mutations could impair TDP-43 liquid-liquid phase separation (LLPS) and are highly prone to aggregation[62]. N-terminally cleaved forms of TDP-43, known as TDP-35 (~35kDa) and TDP-25 (~25kDa) have been identified in ALS-associated aggregates within patient brains and are thought to play a major role in driving aggregation propensity[63]

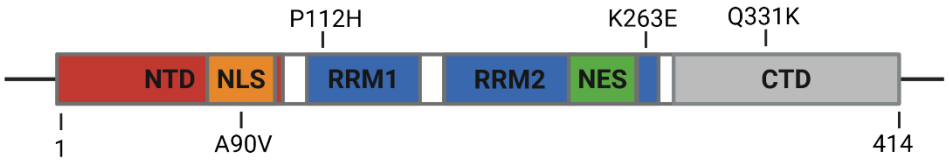

Figure 1. TDP-43 Structure. Schematic representation of TDP-43 domain structures, showing the N-terminal domain (NTD) with a bipartite nuclear localization signal (NLS), two RNA recognition motifs (RRM1 and RRM2), a nuclear export signal (NES), and a C-terminal domain (CTD). Identified TDP-43 mutations are labeled within the domains of TDP-43 (A90V, P112H, K263E, Q331K).

2.2. TDP-43 and its implications in ALS: Composition and formation of aggregates

Cytoplasmic TDP-43 aggregates are found in almost all (97%) ALS patients, regardless of their mutational status[9]. TDP-43 pathology is characterized by the nuclear-to-cytoplasmic mislocalization and accumulation of cytoplasmic aggregates[1,4,50,51] (Figure 2). These aggregates are mostly found in the CNS, including the motor neurons within the primary motor cortex, prefrontal cortex, and spinal cord[9]. Besides the CNS, pathological TDP-43 inclusions have also been found in fibroblasts and skeletal muscle fibers of ALS patients[64,65]. Notably, these pathogenic aggregates differ from the myo-granules. In regenerating skeletal muscle, TDP-43 forms transient, amyloid-like myo-granules that play a physiological role in muscle repair[66]. However, research suggests that an increased formation or impaired clearance of functional myo-granules could lead to pathological cytoplasmic TDP-43 aggregates observed in disease.

At later stages of TDP-43 pathogenesis, TDP-43 aggregates are composed of hyperphosphorylated, ubiquitinated, and cleaved forms of TDP-43, including its C-terminal fragments (CTF) of TDP-35 and TDP-25[2,3]. They also contain the ALS-linked ubiquitin autophagic adaptor Sequestosome (SQSTM1, also known as p62) for the degradation of misfolded proteins through the autophagy pathway[67]. Notably, many of these modifications are typically observed at the end stages of the disease or following multiple cellular insults (e.g., overexpression of TDP-43 combined with additional stressors) to fully manifest. However, the early modification of TDP-43 that leads to its mislocalization and aggregation remains poorly understood. Thus, studying the early mechanisms underlying TDP-43 pathology is crucial for identifying therapeutic targets and developing effective treatments for ALS.

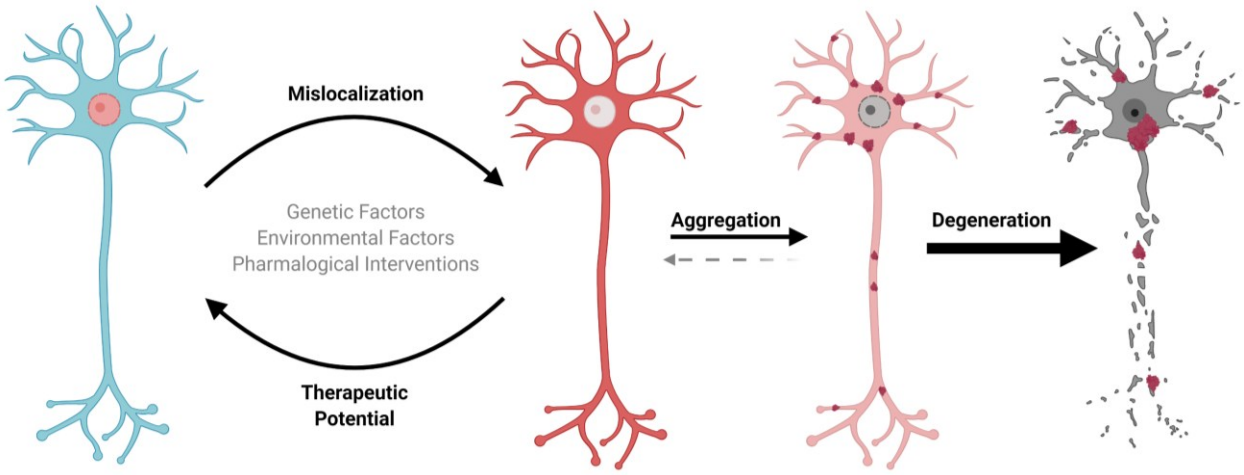

Figure 2. TDP-43 pathology: mislocalization, aggregation and neurodegeneration. Under normal conditions, TDP-43 (red) is primarily located in the nucleus. However, genetic mutations and/or environmental factors can lead to the mislocalization and aggregation of TDP-43, eventually resulting in neurodegeneration. This figure is adapted from **Suk and Rousseaux (2020).**

2.3. Cellular Stress Response

The cellular stress response encompasses a broad range of molecular changes that occur when the cells encounter stressful conditions[68]. These stressors can include oxidative stress, DNA damage, unfolded proteins, viral infection, Endoplasmic Reticulum (ER) stress, chemical stress, and heat shock responses[69,70]. In response to these acute insults, cells activate various stress response pathways, such as the integrated stress response (ISR). The ISR is a conserved response in eukaryotes that activates Eukaryotic Translation Initiation Factor 2A (eIF2a). Upon eIF2a activation, Activating Transcription Factor 4 (ATF4) is translocated into the nucleus to upregulate the transcription of stress-response genes essential for recovery from stress. In addition, eIF2a

activation triggers the formation of membraneless organelles known as stress granules (SG) that transiently sequester and stall mRNA translation as a protective response to stress[71,72]. Their assembly is initiated by nucleators such as G3BP1 or TIA1, which then further promotes the recruitment of additional RNA-binding proteins containing IDRs. Once the stress is recovered, SGs disassemble to allow for translation to resume. Extensive research has shown a strong link between the cellular stress response and ALS[1,4,5]. TDP-43 has been shown to play a critical role in cellular stress response pathways, including DNA damage. For instance, upon UV-induced DNA double-stranded breaks (DSB), TDP-43 facilitates the recruitment of DNA damage complexes to repair DSBs.

2.4. TDP-43 Pathology

2.4.1. TDP-43 mislocalization and aggregation

A variety of stressors including oxidative, osmotic, and heat shock have been used to study TDP-43 pathology[73]. For example, sodium arsenite treatment (oxidative stress) leads to TDP-43 mislocalization, formation of stress granules, and impairs TDP-43 nuclear splicing functions in neuroblastoma cells, patient-derived fibroblasts and motor neurons differentiated from iPSCs[74]. Other studies have used D-sorbitol (hyperosmotic treatment) to model conditions of ionic imbalance and observed TDP-43 nuclear-to-cytoplasmic mislocalization and aggregation[73]. Heat shock is another commonly used stressor that can induce TDP-43 pathology[75]. These studies indicate how different types of cellular stress converge to study TDP-43 mislocalization and aggregation. Therefore, cellular stress models are critical and provide a window to observe and study early features of TDP-43 pathogenesis.

Following stress, TDP-43 is found to localize to transient cytoplasmic membraneless organelles known as stress granules, which facilitate cell survival by stalling mRNA translation[4,5,73,75]. Stress granules consist primarily of RNA and ribonucleoproteins, such as G3BP1 and TIA1[76]. TDP-43 normally stabilizes *G3BP1* transcripts and plays a critical role in regulating the dynamics of stress granule formation and disassembly, where the depletion of nuclear TDP-43 impairs the formation of stress granules[77,78]. This indicates a key role for TDP-43 and G3BP1 in the regulation of this cell survival mechanism. Following acute stress, TDP-43 translocates from the nucleus to the cytoplasm to promote the assembly of stress granules and disassembly upon recovery[5,71]. However, under prolonged stress, the cell can no longer properly recover from the insult. As a result, stress granules can undergo an aberrant phase transition and promote the formation of solid protein aggregates, eventually leading to cell death[79].

2.4.2. TDP-43 nuclear bodies and loss-of-function

Beyond localizing to cytoplasmic structures, TDP-43 is also recruited to various subcellular compartments within the nucleus. Various types of cellular stress (i.e. oxidative, heat shock) have been found to stimulate the formation of TDP-43 into nuclear bodies, which is thought to play a protective role in the cell. Recent studies have identified a form of nuclear body called paraspeckles that interacts with TDP-43. Paraspeckles contain a long noncoding RNA called Nuclear Enriched Abundant Transcript 1 (*NEAT1*) that acts as a scaffold to recruit a variety of RNA-binding proteins[80,81]. Normally, paraspeckles help regulate gene expression by sequestering proteins and RNA. However, the loss of nuclear TDP-43 is sufficient to stimulate paraspeckle hyper-assembly in neurons, possibly as a compensatory mechanism[81]. Studies have identified an increase in paraspeckle formation in the spinal motor neurons of ALS patients with TDP-43 pathology[81]. This suggests that paraspeckles may be serving a protective role by sequestering

pathological TDP-43 and RNA processing. Moreover, under conditions of proteotoxic stress or ATP depletion, TDP-43 has been found to assemble into anisosomes, which are structures composed of RNA-free TDP-43 oligomers forming a dense shell around a liquid-like core enriched with a family of heat shock proteins (HSP-70)[82]. Anisosomes form when TDP-43 loses its ability to bind to RNA due to disease-associated mutations or post-translational modifications (i.e., acetylation) that impair RNA binding. They are thought to serve a protective function by sequestering misfolded TDP-43 and their liquid-like properties are maintained through its direct interaction with HSP70. Additionally, recent studies have identified co-localization of TDP-43 with RNA-binding motif-45 protein (RBM-45) aggregates in the motor neurons of ALS patients[83]. During acute stress, RBM-45 incorporates into nuclear stress bodies (NSBs), and chronic stress can lead to the irreversible accumulation of nuclear RBM-45 inclusions. TDP-43 also localizes to other various nuclear structures in response to stress, such as PML bodies. However, the functions of these nuclear inclusions remain elusive[84].

2.5. TDP-43 post-translational modifications: Focus on SUMOylation

2.5.1. Overview of post-translational modifications in TDP-43

Post-translational modifications (PTMs), including ubiquitination and phosphorylation, have been found to regulate TDP-43 in disease states leading to aggregation. Particularly, abnormal hyperphosphorylation at serine 403 and 404 (S403/404) and serine 409 and 410 (S409/410) has been found to impair degradation pathways, leading to a build-up of TDP-43 aggregates[3].

While the most commonly studied PTMs include phosphorylation and ubiquitination, there are also new studies suggesting that acetylation and poly(ADP-ribosyl)ation (PARylation) also regulate TDP-43[85,86]. Acetylation of lysine residues within the RRMs of TDP-43 has been

shown to disrupt RNA-binding and promote cytoplasmic accumulation[87]. Similarly, PARylation has been shown to promote the recruitment of TDP-43 to stress granules and alter its LLPS properties[85]. Another PTM known as SUMOylation is highly conserved and essential in which SUMO (small ubiquitin-like modifier) molecules covalently bind to lysine residues on a target protein[88,89]. This SUMOylation process is catalyzed by a cascade of enzymes that begin with the activation of SUMO proteins by an E1 ligase. SUMOs are then transferred to the sole E2 ligase, UBC9, which is essential for SUMOylation. Then, SUMOylation of the target protein can often be stabilized by E3 ligases by promoting their interaction. Much like ubiquitination, SUMOylation is a reversible process where SUMO-specific proteases (SENPs) can remove the SUMO group from the substrate[90].

2.5.2. SUMOylation: Mechanism and biological significance

SUMOylation is a key regulatory mechanism governing many cellular processes, including nuclear-cytosolic transport, protein solubility, DNA damage repair, and cellular stress responses[91,92]. SUMO is present as two isoforms: SUMO1 and SUMO2/3, which each have independent and overlapping roles in cellular processes. SUMO1 is the most commonly studied isoform that is involved in nuclear transport, solubility, and apoptosis[93,94]. However, SUMO2 and SUMO3 exhibit 97% protein sequence homology and are often referred to as SUMO2/3[89,95]. This isoform forms poly-SUMO chains, which are involved in more dynamic regulations, including the cellular stress responses and targeting protein for degradation[96]. The latter activity is mediated primarily by SUMO-targeted ubiquitin ligases (STUbLs), which specifically target and ubiquitylate poly-SUMO2/3 modified proteins[97,98]. Increasing evidence suggests that SUMOylation plays a critical role in cellular stress responses. Upon stress, SUMO2/3 has been

reported to conjugate with a variety of target proteins[99]. Understanding the interplay between cell stress and SUMOylated proteins would provide insight into the regulatory pathways involved.

3. PRELIMINARY DATA: TDP-43 SUMOYLATION

3.1. TDP-43 is SUMOylated dynamically during cellular stress and recovery

Oxidative stress via sodium arsenite treatment is the most commonly and widely used cellular stress model to study TDP-43 mislocalization and aggregation *in vitro*. Thus, our lab examined whether TDP-43 becomes SUMOylated in response to sodium arsenite stress. Using immunoprecipitation assay to immunoprecipitate proteins bound to HA-SUMO under denaturing conditions to break apart non-covalent bonds, we found that TDP-43 becomes SUMOylated by SUMO2[6].

To investigate the dynamics of TDP-43 SUMOylation, we conducted a time-course assay by stressing the cells with sodium arsenite for 1 hour and allowing the cells to recover from stress. Surprisingly, we observed an increase in SUMOylated TDP-43 during the initial hour of recovery before its degradation by the proteasome during the third hour of recovery[6] (Figure 3A). This suggests that TDP-43 SUMOylation may play an important role in efficient recovery from cell stress. Previous studies have shown that TDP-43 interacts with RNF4, which is a ubiquitin ligase that targets SUMOylated proteins for polyubiquitination and subsequent degradation through the ubiquitin-proteasome system (UPS)[98]. To further investigate whether the UPS is responsible for clearing SUMOylated TDP-43 in the recovery phase post-stress, we treated cells with the proteasome inhibitor MG132 and found that SUMOylated TDP-43 persisted and is not cleared, suggesting that TDP-43 SUMOylation is marked for ubiquitin proteasomal degradation[6]. Treatment with MG132 alone did not induce SUMOylation of TDP-43. Overall, these findings

suggest that TDP-43 becomes SUMOylated dynamically in the cellular stress response, which in turn promotes ubiquitin-mediated degradation during recovery. Therefore, SUMOylation seems to be a critical mechanism for maintaining TDP-43 proteostasis[6].

Using GPS-SUMO, we predicted two SUMOylation sites on TDP-43: K136 and K408[6]. First, K136 is found in the first RNA recognition motif and is thought to be targeted by SUMO1. K408 is in the C-terminal domain of TDP-43. We performed a GFP-Trap SUMOylation assay and expressed TDP-43-GFP that blocked the K136 and K408 sites by mutating the lysine to an arginine residue. We observed that TDP-43 K136R did not alter TDP-43 SUMOylation, however, TDP-43 K408R significantly reduced TDP-43 SUMOylation suggesting TDP-43 is SUMOylated primarily at lysine 408[6] (Figure 3B).

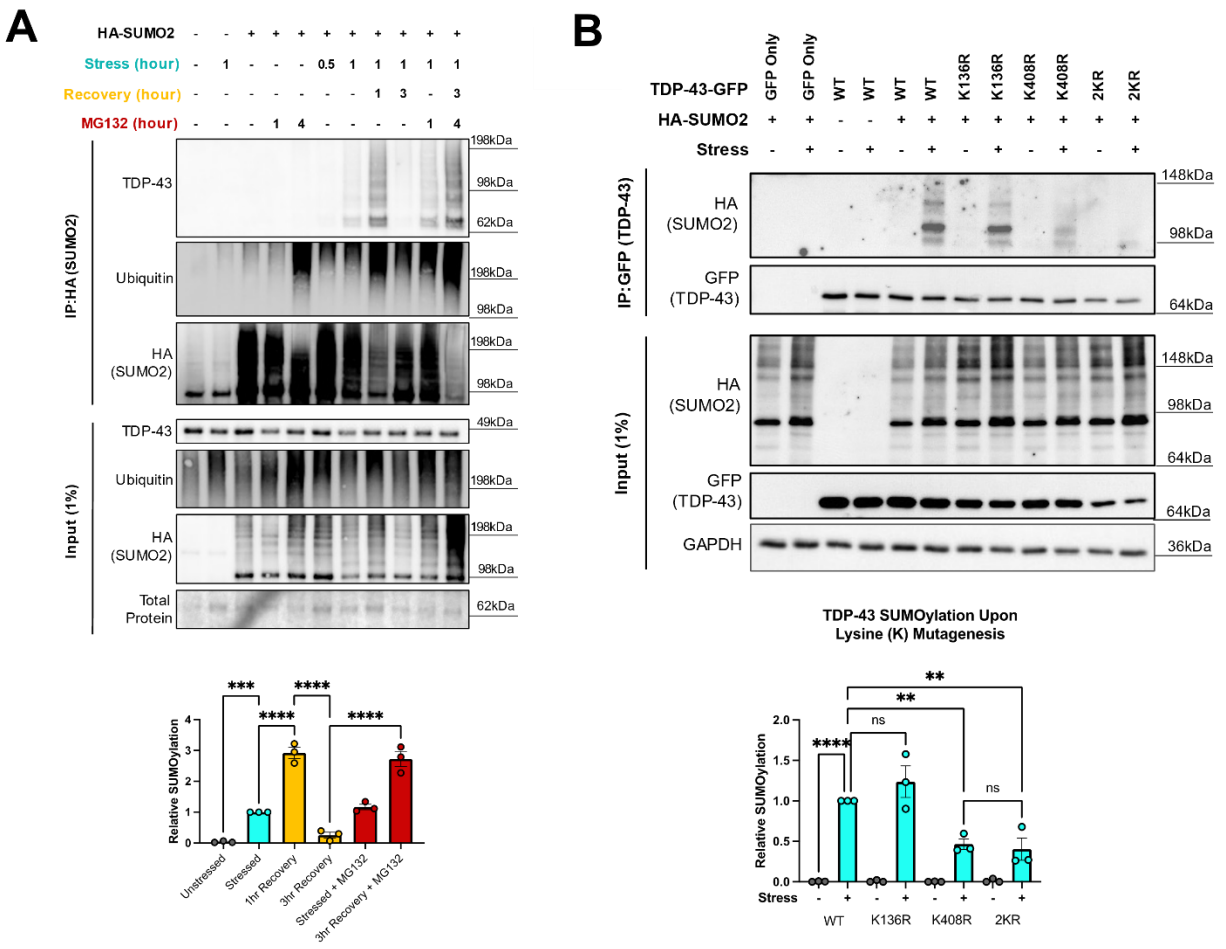

Figure 3. SUMOylation dynamically regulates TDP-43 upon stress and recovery. (A) Immunoprecipitation (IP) of HA-SUMO2 conjugates from cells subjected to stress and recovery conditions, followed by immunoblotting for TDP-43, ubiquitin, and HA-SUMO2. Input controls (1%) for TDP-43, ubiquitin, HA-SUMO2, and total protein are shown. Conditions include unstressed, 1 hour stress (250µM), 1-hour recovery, 3-hour recovery, and stress/recovery with MG132 treatment (2µM). Quantification of relative SUMOylation levels under the indicated conditions. Data are presented as mean ± SEM. Statistical significance between groups is indicated as follows: ***p<0.0005 and ****p<0.0001, 1-Way ANOVA with Fischer's LSD test. **(B)** Representative GFP-Trap SUMOylation assay to confirm the site of TDP-43 SUMOylation during 1 hour of sodium arsenite stress (250µM). 1-way ANOVA with Fischer's LSD test data presented

as mean ± SEM, *p<0.005, **** p<0.0001. **Data, analysis, and figures were generated by Dr. Terry Suk from Suk et al. 2025 Molecular Neurodegeneration.**

3.2. Generation and characterization of the knock-in mouse model (K408R)

To determine the implications of the loss of TDP-43 SUMOylation, our lab generated a SUMO-deficient (Tdp-43$^{K408R/K408R}$) knock-in mouse model using CRISPR-Cas9 to block endogenous Tdp-43 from being SUMOylated[6]. We found that the Tdp-43$^{K408R/K408R}$ mice present with some mild behavioral deficits including cognitive abnormalities. Histology of these mice also showed pathological hallmarks, such as Tdp-43 mislocalization in the spinal cord and increased phosphorylated Tdp-43 in the cortex[6]. However, we do not understand the mechanisms of how SUMOylation may be linked to this pathology, such as whether it plays a role in mislocalization, solubility, or other aspects of pathology. The histology of the Tdp-43$^{K408R/K408R}$ mice only allows us to observe Tdp-43 at a fixed time point, which makes it difficult to investigate the specific role SUMOylation plays during pathogenesis.

Additionally, current research primarily focuses on TDP-43 pathogenesis in response to acute cellular stress. However, how TDP-43 pathology is affected after the removal of stress (recovery phase) is poorly understood. By blocking SUMOylation of TDP-43 and observing the consequences during cell stress and recovery, we will better understand the implications of TDP-43 SUMOylation in ALS pathogenesis. This study will help us better understand how TDP-43 and SUMOylation play a role in response to cellular stressors, which may uncover specific pathways that could serve as therapeutic targets in TDP-43 proteinopathies.

4. HYPOTHESIS

Loss of SUMOylation alters TDP-43 localization, solubility, and cellular stress response mechanisms during stress and recovery.

5. AIMS

1) Assess how the loss of TDP-43 SUMOylation affects the cellular stress response during acute and repeated stress.
2) Characterize how SUMOylation affects TDP-43 dynamics and mobility during repeated stress and recovery.

6. CONTRIBUTIONS TO THE PROJECT

Generation of the knock-in K408R mouse model was completed by Dr. Terry Suk (PhD graduate, Rousseaux lab, University of Ottawa) in collaboration with The Center for Phenogenomics (SickKids). Generation and characterization of HA-SUMO2 HEK293T cell lines were completed by Dr. Terry Suk (PhD graduate, Rousseaux Lab, University of Ottawa). Primary murine embryo cortical neurons were collected, dissected, and dissociated by Dr. Terry Suk and Ben Nguyen (PhD candidate, Rousseaux Lab, University of Ottawa). Acute stress and recovery (Figure 4A and B) immunofluorescence experiment, analysis and figure generation were performed by Dr. Terry Suk. Generation of lentiviral HSPA1L-mScarlet3 was performed by Dr. Terry Suk. The completion of all other experiments, including their data analysis and figure generation, was completed by myself.

7. METHODS

1. Immunofluorescence in primary cortical neurons

As stated in the Suk et al paper: “Micro Coverglass #1.5 coverslips (Electron Microscopy Sciences) coverslips were washed in 2M HCl overnight at 55 °C, washed 5 times in sterile H2O, then pre-coated with poly-D-lysine (50 μg/mL) overnight at 37 °C, then washed with distilled water three times and air-dried at room temperature for at least 2 hours. Primary mouse cortical neurons were seeded at 75,000-100,000 cells per coverslip and cultured as described above. On day 7, neurons were fixed for 10 minutes using 10% phosphate buffered formalin (Fisher Chemical, SF100-4) followed by 3 x 5-minutes washes in 1 mL of 1X PBS. Neurons were blocked in 500 μL of blocking buffer (1% Triton X-100, 10% cosmic calf serum in 1X PBS) for 1 hour, then incubated in 300 μL of primary antibody diluted in blocking buffer overnight at 4 °C. The following day, the neurons were washed for 5 x 5-minutes in 1 mL of 1X PBS then incubated in 300 μL of secondary antibody diluted in blocking buffer for 2 hours at room temperature. Neurons were then washed in 1 mL 1X PBS, then stained with DAPI for 10 minutes at room temperature followed by 4 x 5- minutes washes in 1X PBS before being mounted using antifade fluorescence mounting media (Dako, S3023). Z-stack images were obtained on a Zeiss AxioObserverZ1 LSM800 Confocal Microscope at 40× magnification with a 2× digital zoom through a Z distance of 10-12 μm per image using optimal spacing per slice with dimensions set to 1024 x 1024 pixels with 4X averaging per frame. At least 50 cells were imaged and quantified per replicate. For TDP-43 foci co-localization, Z-stack images were obtained on a Zeiss AxioObserver Z1 LSM880 AiryScan confocal microscope at 63x magnification with 3X digital zoom at 512 x 512 resolution. At least 10 cells presenting with TDP-43 foci were imaged per replicate. Images were analyzed and quantified using ImageJ.”

2. Generation of TDP-43-mStayGold and TDP-43-EGFP stable HEK293T cell lines.

To generate TDP-43-mStayGold (WT and TDP-$43^{K408R/K408R}$) and TDP-43-EGFP (WT and TDP-$43^{K408R/K408R}$) plasmids, TDP-43-mStayGold constructs were synthesized in pENTR vectors through TwistBioscience on Addgene. The pENTR TDP-43-EGFP constructs (WT and K408R) were obtained from the Rousseaux lab. Using Gateway cloning, TDP-43-mStayGold and TDP-43-EGFP were cloned into pLEX307 plasmids to allow for constitutive expression. Following the manufacturer's protocol, the LR Clonase II enzyme mix was used for the recombination reactions. Reaction mixtures were incubated at 25°C for 1 hour and then transformed into STBL3 cells. Positive clones were selected on LB agar plates supplemented with 1ug/ml ampicillin antibiotics. Plasmids were purified using a plasmid purification kit and sequenced using Sanger sequencing to validate the insert and the presence of the TDP-$43^{K408R/K408R}$ mutation.

HEK293T cells were cultured in DMEM supplemented with 10% fetal bovine serum (FBS) and 1% antibiotic-antimycotic (100x) and maintained at 37 °C with 5% CO_2. For lentiviral packaging, HEK293T cells were seeded at a density of 2.5 × 10^6 cells per 10 cm dish 24 hours before transfection. Cells were transfected with the pLEX307 TDP-43 plasmids (WT and TDP-$43^{K408R/K408R}$), along with the packaging plasmids psPAX2 (Gift from Didier Trono, Addgene #12259) and pMD2.G (Gift from Didier Trono, Addgene #12260). The transfection mixture was incubated with cells for 5 hours, after which the media was replaced with fresh DMEM containing 10% FBS and 1% antibiotic-antimycotic (100x). Viral supernatant was collected 48- and 72-hours post-transfection, pooled, and filtered through a 0.45 μm filter to remove cellular debris. The filtered viral media was concentrated by ultracentrifugation at 100,000 × g for 2 hours at 4°C. The resulting viral pellet was resuspended in sterile 1X phosphate-buffered saline (PBS) and stored at −80°C until use.

HEK293T cells were seeded at a density of 1.0 × 10^6 cells per well in a 6-well plate. Cells were infected with the concentrated lentivirus carrying pLEX307 TDP-43 plasmids (WT and TDP-$43^{K408R/K408R}$). After 24 hours, the viral media was replaced with fresh DMEM containing 10% FBS and 1% antibiotic-antimycotic (100x). The stable cell lines were validated by fluorescence microscopy and western blot to confirm the expression of TDP-43-mStayGold and TDP-43-EGFP (WT and TDP-$43^{K408R/K408R}$).

3. TDP-43 colocalization with HSPA1L

As stated in the Suk et al paper: "HSPA1L colocalization experiment was designed similar to previous approaches that identified TDP-43 forming anisosomes in response to stress. HSPA1L-mRuby2 was designed and synthesized in a pTwist-Lenti-Puro backbone (Twist Bioscience). Next, the pTwist-Lenti HSPA1L-mRuby2 plasmid was packaged into lentivirus by co-transfection of psPAX2 (Gift from Didier Trono, Addgene #12259), and pMD2-G (Gift from Didier Trono, Addgene #12260) at equimolar concentrations into HEK293T cells. After 24 hours, media was changed and discarded. Media was collected 48 hour and 72 hours post-transfection. Viral media was filtered through a 0.45 μm filter then concentrated by centrifugation at 100,000g for 2 hours at 4 °C and the pellet was resuspended in 1X PBS. Cortical primary neurons were cultured as previously described and lentiviral infection was performed at the time of plating (0 DIV). Cells were cultured to 7 DIV then were stressed with 250 μM sodium arsenite for 1 hour and recovered for 3 hours to induce TDP-43 foci formation. Cells were fixed in 10% formalin for 10 minutes and immunofluorescent staining was performed for TDP-43 as described above. Z-stack images were obtained on a Zeiss AxioObserver Z1 LSM880 AiryScan confocal microscope at 63x magnification with 3X digital zoom at 512 x 512 resolution. At least 10 cells presenting with TDP-

43 foci and HSPA1L foci were imaged per replicate. Images were analyzed and quantified using ImageJ."

4. Western blot

As stated in the Suk et al paper: "Western blot analysis Protein sample prepared in Laemmli loading buffer was loaded onto 8% polyacrylamide gel, TGx Mini-PROTEAN 4-15% precast gel (BioRad), or Bolt Bis-Tris Plus Mini-Protein Gel 4- 12% (Invitrogen) and run at 100-140 constant voltage in Tris-Glycine or MES buffer for their respective gels. Proteins were transferred onto a 0.45 µm nitrocellulose membrane at a constant 340 mA for 2 hours at 4 °C. The membranes were blocked in 10% milk diluted in TBS-T washed 5 x 5 minutes in TBS-T then incubated in primary antibody overnight (table S5). The following day the membranes were washed for 5 x 5 minutes in TBS-T, then incubated in secondary antibody for 1-2 hours at room temperature. Finally, the secondary antibody is washed 5 x 5 minutes in TBS-T before being imaged using chemiluminescence Clarity Western ECL or Clarity Max Western ECL on an LAS4000 (GE). Densitometry was performed using the volumes function of the ImageLab (BioRad) software."

5. Photobleaching Decay Assay and Quantifications

To assess photobleaching dynamics, WT TDP-43-mStayGold and TDP-43-EGFP HEK293T stable cell lines were imaged using an LSM880 confocal microscope (Zeiss) equipped with a 488 nm laser. Cells were seeded onto 8-well glass chamber slides (Thermofischer, CAT# 171080) and maintained in DMEM supplemented with 10% FBS and 1% antibiotic-antimycotic (100x) at 37°C with 5% CO2 prior and during imaging using an environmental chamber. The 488 nm laser was set to 50% power intensity, and images were captured every 500 ms over a 3-minute duration, resulting in a total of 360 frames per acquisition. Photobleaching dynamics were monitored, and

fluorescence decay was analyzed post-acquisition using Zeiss Zen software. Normalized fluorescence intensity curves were generated to assess the photostability of TDP-43-mStayGold and TDP-43-EGFP HEK293T cell lines.

6. Fluorescence Recovery After Photobleaching (FRAP) Assay and Quantifications

To investigate the mobility of TDP-43 during cellular stress and recovery, Fluorescence Recovery After Photobleaching (FRAP) was performed. HEK293T stable cell lines expressing TDP-43-mStayGold (WT and TDP-43$^{K408R/K408R}$) were seeded onto 8-well glass chamber slides (Thermofischer, CAT# 171080) and maintained in DMEM supplemented with 10% FBS and 1% antibiotic-antimycotic (100x) at 37°C with 5% CO_2 prior and during imaging using an environmental chamber. FRAP experiments were conducted with a Zeiss LSM880 AiryScan microscope with 63x oil objective at 512 x 512 resolution at 37°C and 5% CO2 equipped with a 488 nm argon laser. Following repeated 30-minute stress and 30-minute recoveries, a small ROI (1/4 of the nucleus) of TDP-43 in the nucleus was photobleached using 50% laser power, followed by imaging at 250 ms intervals for 2 minutes to monitor fluorescence recovery. The FRAP data was quantified using the Zen software. The time series of fluorescence intensity was calculated, and the intensity of the background (area with no cells) was subtracted from the intensity of the photobleached ROI. The intensity of the background was also subtracted from the intensity of a non-photobleached ROI. The fluorescence intensity of the photobleached region was normalized to the non-photobleached region to account for fluctuations in fluorescence intensity. The intensity of the 5 pre-bleached ROI was normalized to 1 to achieve the maximum value of intensity and normalized to 0 upon bleaching to achieve the minimum value of intensity. The Area Under the Curve (AUC) of each graph was calculated and plotted using GraphPad Prism to show total fluorescence recovered over time. Then, the averaged relative intensity and standard error were

plotted to calculate the mobility of TDP-43 recovered over time. At least 1 cell was imaged per replicate and quantified a total of 4 biological replicates per genotype.

7. Live-Cell Imaging Stress and Recovery Assay

To determine changes in TDP-43 localization during stress and recovery, live-cell imaging was performed to monitor TDP-43 nuclear and cytoplasmic intensity in real time. HEK293T stable cell lines expressing TDP-43-mStayGold (WT and TDP-43$^{K408R/K408R}$) were seeded onto 8-well glass chamber slides (Thermofischer, CAT# 171080) and maintained in DMEM supplemented with 10% FBS and 1% antibiotic-antimycotic (100x) at 37°C with 5% CO2. Imaging was conducted with a Zeiss LSM880 AiryScan microscope with 63x oil objective at 1024 x 1024 resolution at 37°C and 5% CO2 equipped with a 488 nm argon laser. Images were acquired at 2.5-minute intervals over a 30-minute stress period, followed by a 30-minute recovery period in sodium arsenite-free media. During imaging, cells were maintained at 37°C with 5% CO2 using an environmental chamber. Time-lapse images were analyzed using ImageJ. The average nuclear and cytoplasmic fluorescence intensity for each cell was measured, and background fluorescence was subtracted. At least 5-6 cells were imaged per replicate and quantified a total of 5 biological replicates per genotype.

8. RESULTS

8.1. Loss of TDP-43 SUMOylation affects stress granule dynamics following cellular stress and recovery.

Treatment of cells with cellular stressors (i.e., sodium arsenite) is used to study the cellular stress response through stress granule dynamics. Since TDP-43 is crucial for the formation of stress granules (G3BP1-positive foci), we investigated their formation and disassembly during stress and recovery in neurons. Using immunofluorescence (IF), we observed that stress granules in TDP-$43^{K408R/K408R}$ and WT neurons form to the same degree, but there is a significant delay in stress granule clearance during the first hour of recovery in the TDP-$43^{K408R/K408R}$ mutant (Figure 4A). Eventually, the cells recover similarly to the WT cells during the third hour of recovery. This suggests that K408R neurons exhibit early impaired recovery from stress.

We then explored whether repeated short insults could further impair the stress response, especially when cells are not allowed to fully recover between stresses. We designed a paradigm where the neurons were stressed for 30 minutes with sodium arsenite and then recovered for 30 minutes before receiving the next insult. This was done a total of 3 times over 3 hours. In WT neurons, stress granules form during the first stress and persist during the first recovery. With more rounds of stress, more cells form stress granules, but with subsequent recoveries, the proportion of cells with stress granules slightly decreases. This suggests the cells are trying to recover, but each new stress adds onto the previous effects without allowing the cells to fully recover. Conversely, in TDP-$43^{K408R/K408R}$ neurons, stress granules start forming within the first 30 minutes of stress, but their recovery and re-assembly during later stresses do not occur properly (Figure 4B).

We then observed TDP-43 subcellular distribution during acute and repeated stress. Upon acute stress, we found that the loss of SUMOylation led to a significant accumulation of nuclear TDP-43 foci (which we have termed nuclear TDP-43 “recovery” bodies) during the 3-hour recovery time point (Figure 4C). During repeated stress and recovery, the loss of SUMOylation led to a significant increase in the proportion of cells with nuclear TDP-43 recovery bodies, specifically after the third round of stress and recovery (Figure 4D). This indicates that the loss of SUMOylation not only affects nuclear TDP-43 distribution upon acute stress but also leads to the accumulation of nuclear TDP-43 with repeated stress events. However, the nature and function of these nuclear TDP-43 recovery bodies remain unknown. Finally, we analyzed the proportion of cells with TDP-43 mislocalization following repeated stress and recovery and did not find any statistical significance (Figure 4E).

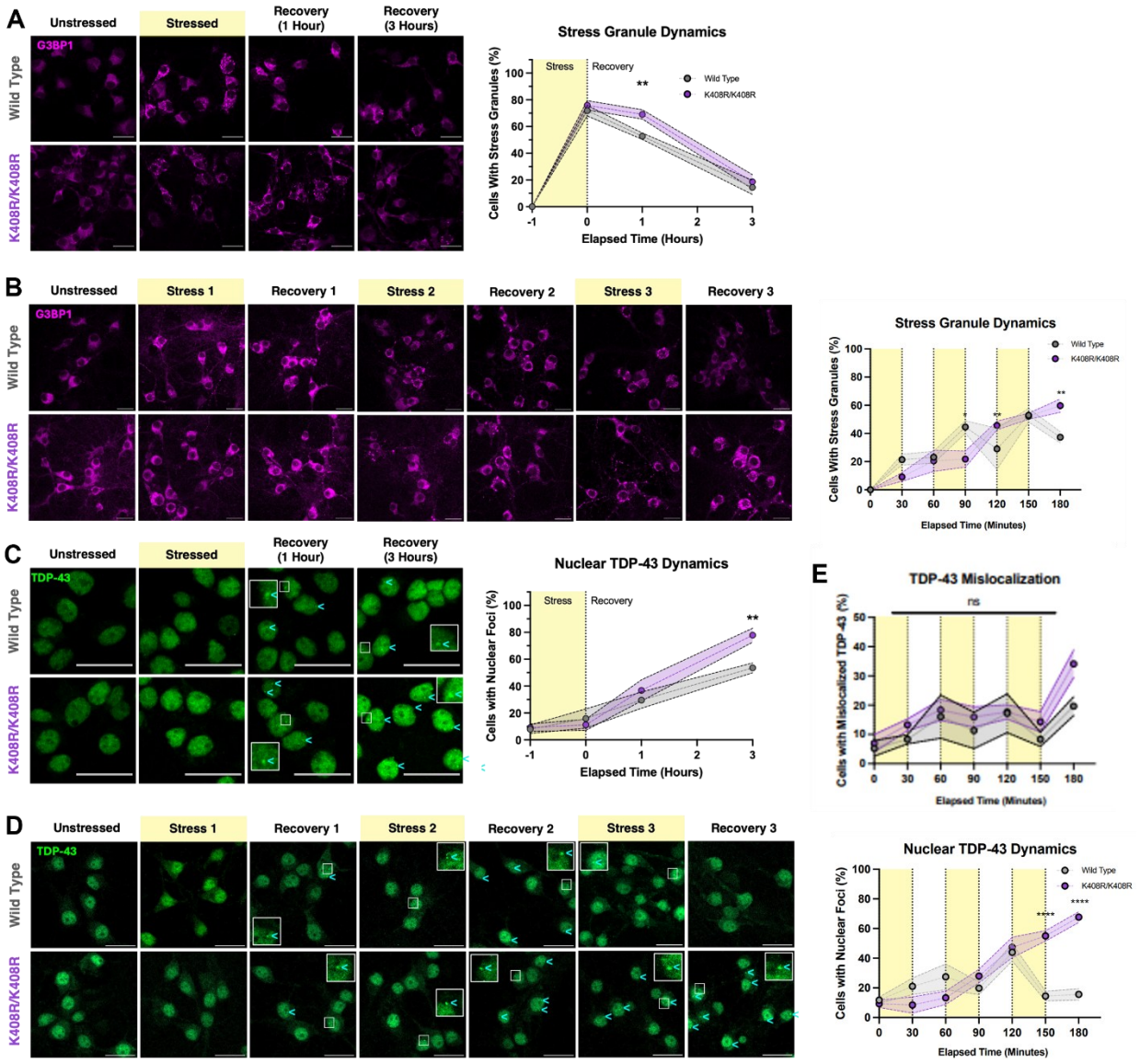

Figure 4. Loss of TDP-43 SUMOylation impairs the cellular stress response in neurons. **(A)** Representative images and quantification of G3BP1 stress granule dynamics in mouse primary cortical neurons (7 DIV) following 1 hour of 250 μM sodium arsenite stress, then 1-hour and 3-hour recovery. G3BP1 contrast was set for optimal visualization of stress granules. Scale Bar = 25μm, N = 5, 2-way ANOVA with Fischer's LSD test. Data presented as mean ± SEM, **p<0.005. For each replicate, at least 50 cells were imaged and quantified. **(B)** Representative images and quantification of G3BP1 stress granule dynamics in mouse primary cortical neurons (7 DIV)

following 30-minute repeated stress (yellow-shaded regions) with 250 μM sodium arsenite treatment and 30-minute recoveries (white-shaded regions), repeated 3 times. Scale Bar = 25μm, N = 3, 2-way ANOVA with Fischer's LSD test. Data presented as mean ± SEM, *p<0.05, **p<0.005. For each replicate, at least 50 cells were imaged and quantified. **(C)** Representative images and quantifications of TDP-43 nuclear foci formation in mouse primary cortical neurons (7 DIV) following 1 hour of 250 μM sodium arsenite stress, then 1-hour and 3-hour recovery. Cyan arrowheads denote cells with nuclear TDP-43 foci. Scale Bar = 25μm, N = 5, 2-way ANOVA with Fischer's LSD test. Data presented as mean ± SEM, **p<0.005. For each replicate, at least 50 cells were imaged and quantified. **(D)** Representative images and quantification of TDP-43 nuclear foci formation in mouse primary cortical neurons (7 DIV) following 30-minute repeated stress (yellow-shaded regions) with 250μM sodium arsenite treatment and 30-minute recoveries (white-shaded regions), repeated 3 times. Cyan arrowheads denote cells with nuclear TDP-43 foci. Scale Bar = 25μm, N = 3, 2-way ANOVA with Fischer's LSD test. Data presented as mean ± SEM, ****p<0.0001. For each replicate, at least 50 cells were imaged and quantified. (**E)** Quantification of primary cortical neurons with TDP-43 mislocalization following 30-minute repeated stress (yellow-shaded regions) with 250 μM sodium arsenite treatment and 30-minute recoveries (white-shaded regions), repeated 3 times. N = 3, 2-way ANOVA with Fischer's LSD test. Data presented as mean ± SEM, ns (not significant). **Data generated alongside Dr. Terry Suk and Ben Nguyen.**

8.2. A subset of RBM-45-positive nuclear foci co-localize with TDP-43 upon cellular recovery.

Various types of cellular stress (i.e., oxidative, heat shock) have been found to stimulate the formation of TDP-43 into nuclear bodies. We have tested many markers of nuclear foci related

to cellular stress and recovery such as paraspeckles, anisosomes, ubiquitin and RBM-45. TDP-43 is found to regulate paraspeckles, where the loss of nuclear TDP-43 is sufficient to stimulate paraspeckle formation[81]. Furthermore, TDP-43 has been identified to form spherical shells with a liquid core of Heat Shock Proteins (HSPs) called "anisosomes", which occurs when TDP-43 loses its ability to bind to RNA[82]. Ubiquitination is another hallmark of TDP-43 aggregates in disease, as the Ubiquitin Proteosome System (UPS) is thought to be one of the primary mechanisms of TDP-43 clearance[98]. Finally, *RBM-45* has been identified as a potential risk gene for ALS and forms nuclear and cytoplasmic aggregates in ALS[100].

We performed an IF assay to assess the co-localization of TDP-43 with nuclear markers: PSPC-1 for paraspeckles, UBI-1 for ubiquitin, RBM-45, and overexpressed HSPA1L-mRuby for anisosomes. HSPA1L-mRuby was designed and synthesized in a pTwist-Lenti-Puro backbone (Twist Bioscience) and visualized through lentiviral transduction of HSPA1L-mRuby2. We found that these foci are not anisosomes or paraspeckles, nor did they colocalize with ubiquitin (Figures 5A-C). However, preliminary data show that some nuclear TDP-43 foci contain RBM-45 but have significantly higher co-localization in the TDP-43$^{K408R/K408R}$ cells (Figure 5D).

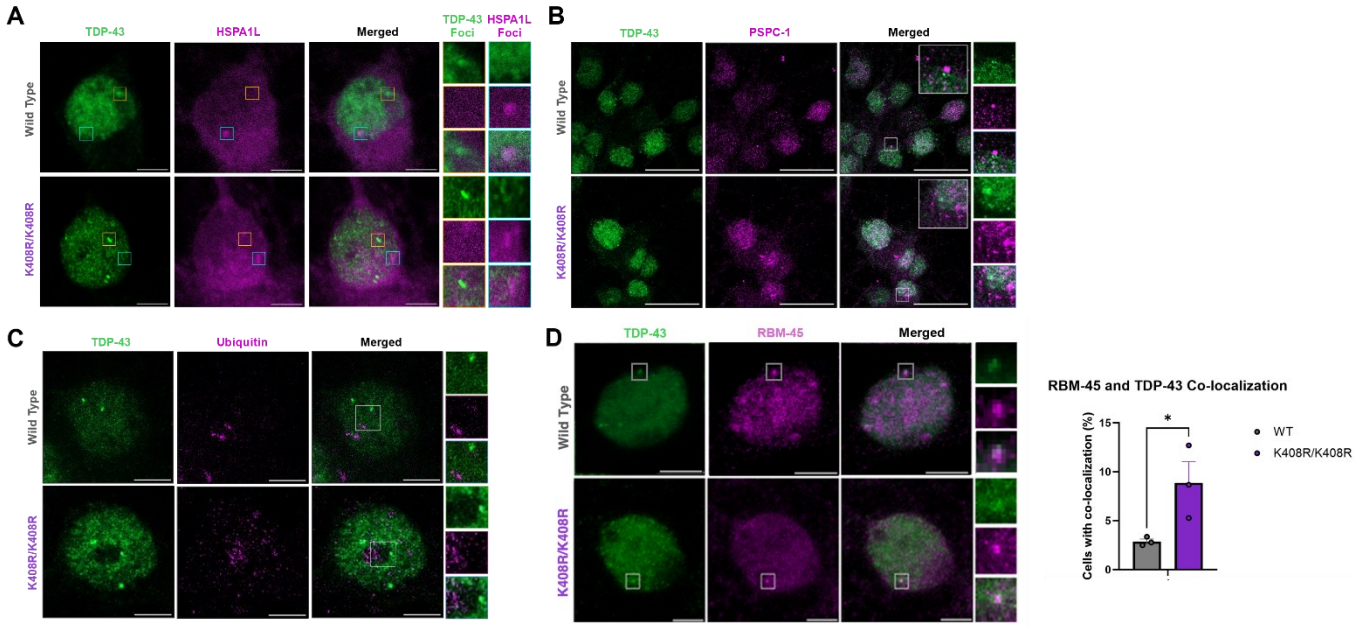

Figure 5. Identifying nuclear foci markers that co-localize with TDP-43 upon recovery. **(A-D)** Representative immunofluorescent images of primary cortical neurons (7 DIV) treated with 250 µM sodium arsenite for 1 hour then recovered for 3 hours to induce TDP-43 foci formation to analyze co-localization with nuclear markers: (**A)** HSPA1L was visualized through lentiviral transduction of HSPA1L-mRuby2 (N = 3); **(B)** Paraspeckle marker PSPC-1 (N = 3); **(C)** Ubiquitin (N = 3). **(D)** Preliminary data for RBM-45 (N = 3). Scale bar = 5µm. Unpaired T-test. Data presented as mean ± SEM, *p<0.05. At least 10 cells positive for TDP-43 foci and foci of interest were imaged and analyzed per biological replicate.

8.3. Characterizing TDP-43-StayGold WT vs K408R in HEK293T cell lines.

Live-cell imaging is critical for studying real-time TDP-43 dynamics and how the loss of SUMOylation affects its localization and the cellular stress response. Unlike imaging fixed cells, live-cell imaging can capture real-time subcellular distribution of the same cells at short time scale

resolutions over long periods of time, which can provide us an in-depth understanding of the role of SUMOylation in TDP-43 pathology.

Monomeric StayGold (E138D), also called mStayGold, is a genetically engineered green fluorescent protein derived from *Cyanobacterial Phycobiliproteins*[7]. This protein is designed for higher signal intensity with improved time resolution and extended timescale imaging compared to traditional fluorescent proteins like GFP. To visualize TDP-43 in real time, we generated lentiviral constructs expressing TDP-43-EGFP and TDP-43-mStayGold under the constitutive EF1a promoter. Stable HEK293T cell lines were established for both WT and TDP-43$^{K408R/K408R}$ variants (Figures 6A and B).

Using live-imaging, we validated that TDP-43-mStayGold is approximately two-fold brighter and showed greater signal intensity compared to TDP-43-EGFP. We also show that TDP-43 mStayGold is roughly equivalent to endogenous TDP-43 with respect to localization in the nucleus (Figure 6B). Western blot analysis confirmed that the mStayGold fusion does not alter TDP-43 protein levels compared to EGFP (Figure 6C). To validate that TDP-43-mStayGold is more photostable than TDP-43-EGFP, we performed a photobleaching assay. As expected, the live-cell images reveal that TDP-43-EGFP is almost completely photobleached between 90 and 120 seconds, while TDP-43-mStayGold maintains its signal intensity and brightness (Figure 6D). These findings support that mStayGold is an optimal fluorescent tag for studying TDP-43 dynamics in live cells.

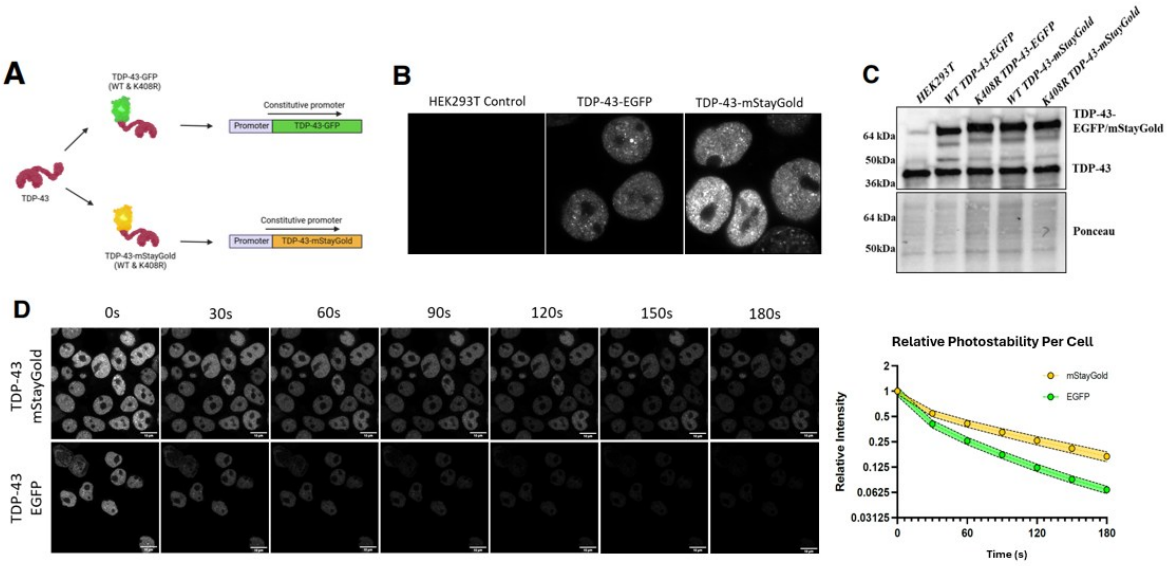

Figure 6. Characterizing TDP-43-mStayGold versus TDP-43-EGFP in HEK293T cells. (**A)** Generation of stable cell line (HEK293T) expressing TDP-43-EGFP and TDP-43-mStayGold using the constitutive expression lentivirus (pLEX307 backbone) for both WT and TDP-43$^{K408R/K408R}$ variants. (**B)** Confocal images of control, TDP-43-EGFP and TDP-43-mStayGold to assess baseline intensity of cells. (**C)** Representative western blot to observe endogenous TDP-43, TDP-43-mStayGold and TDP-43-EGFP protein levels. (**D)** Representative images and quantifications of photobleaching decay assay using confocal laser scanning microscope. Cells were imaged at 50% laser power in 30-second intervals over a total time course of 3 minutes to quantify the relative rate of decay between TDP-43-EGFP and TDP-43-mStayGold. Scale bar = 10µm. The graph shows the photobleaching decay curves for TDP-43-mStayGold (yellow) and TDP-43-EGFP (green). Fluorescence intensity (log2 scale) is normalized at time 0 for both mStayGold and EGFP and plotted as a function of time (seconds).

8.4. Loss of SUMOylation may alter TDP-43 subcellular distribution following repeated stress and recovery.

Overexpression models of TDP-43 have been widely used to investigate nuclear depletion, nuclear-to-cytoplasmic mislocalization, and aggregation[101–103]. Previous work shows that the overexpression of WT TDP-43 or mutants (e.g., Q331K, M337V, A315T) in HEK293 and primary neurons leads to cytoplasmic accumulation, association with stress granules, and the formation of TDP-43 aggregates[103–105]. These models are also commonly used to study PTMs including phosphorylation and ubiquitin. Even more, stress conditions can further enhance these phenotypes in cell culture.

Therefore, using laser scanning confocal microscopy, we observed the subcellular localization of the WT versus TDP-43$^{K408R/K408R}$ HEK293T stable cell lines in live time using repeated sodium arsenite stress and recovery. We treated the cells with sodium arsenite over a course of 30 minutes of stress, then 30-minute recovery for 3 repeated cycles, imaging in 2.5-minute intervals. Following repeated rounds of stress and recovery, WT cells maintained their nuclear localization throughout (Figure 7). While we did not observe any statistical significance when we quantified broad TDP-43 mislocalization in TDP-43$^{K408R/K408R}$ mutant cells, we noticed the formation of cytoplasmic TDP-43 inclusions following repeated stress and recovery (Figure 7). We also observed variability in TDP-43$^{K408R/K408R}$ suggesting changes occurring in TDP-43 localization. Further analysis is needed to quantify the number and size of cytoplasmic TDP-43 foci between WT and TDP-43$^{K408R/K408R}$ cells.

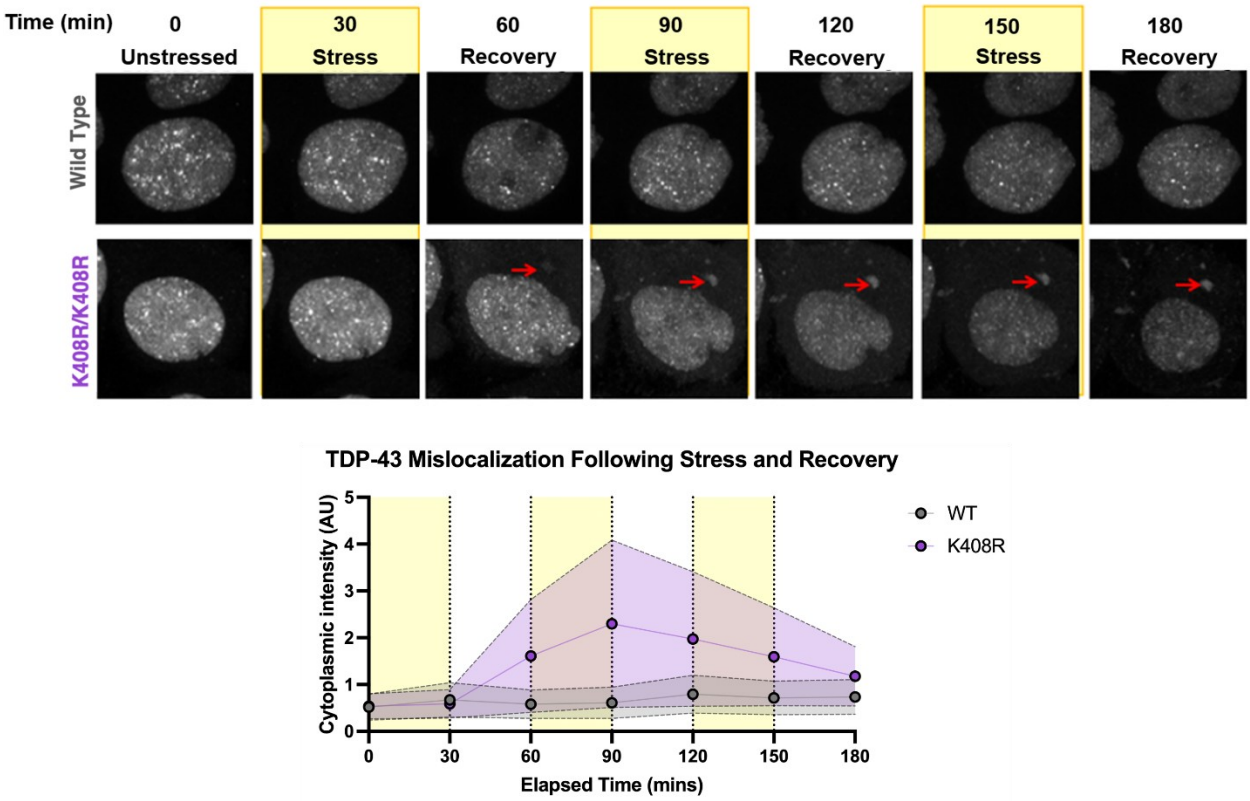

Figure 7. SUMOylation does not affect TDP-43 dynamics during repeated stress and recovery. (A) Representative confocal laser scanning microscopy images and quantification of HEK293T cells expressing TDP-43-StayGold (WT and TDP-43$^{K408R/K408R}$) following 30-minute repeated stress with 250 µM sodium arsenite treatment and 30-minute recoveries, repeated 3 times. The graph shows the cytoplasmic intensity of TDP-43 over time in minutes, following repeated rounds of stress (yellow-shaded regions) and recovery (white-shaded regions). The red arrowheads denote cytoplasmic TDP-43 inclusions. Data are presented as mean ± SEM, 2-Way ANOVA, N = 5, not significant. At least 5 cells were imaged and quantified per replicate (total of 25 cells per genotype).

8.5. Cytoplasmic TDP-43 inclusions co-localize with G3BP1 stress granules upon recovery in TDP-43$^{K408R/K408R}$ HEK293T stable cell line.

Following the live-cell imaging experiment, we questioned whether these cytoplasmic TDP-43 inclusions are G3BP1-positive in the TDP-43$^{K408R/K408R}$ cell lines. Using IF, we co-stained for TDP-43 and G3BP1 during the third repeated recovery. We observed a significantly higher proportion of TDP-43 inclusions co-localizing with G3BP1-positive stress granules (Figure 8). These findings suggest that the loss of SUMOylation may enhance the association between TDP-43 and stress granules. Further investigation would be required to determine whether TDP-43 is localized within stress granules or whether TDP-43 has aggregated and interacts with G3BP1 through protein-protein interactions.

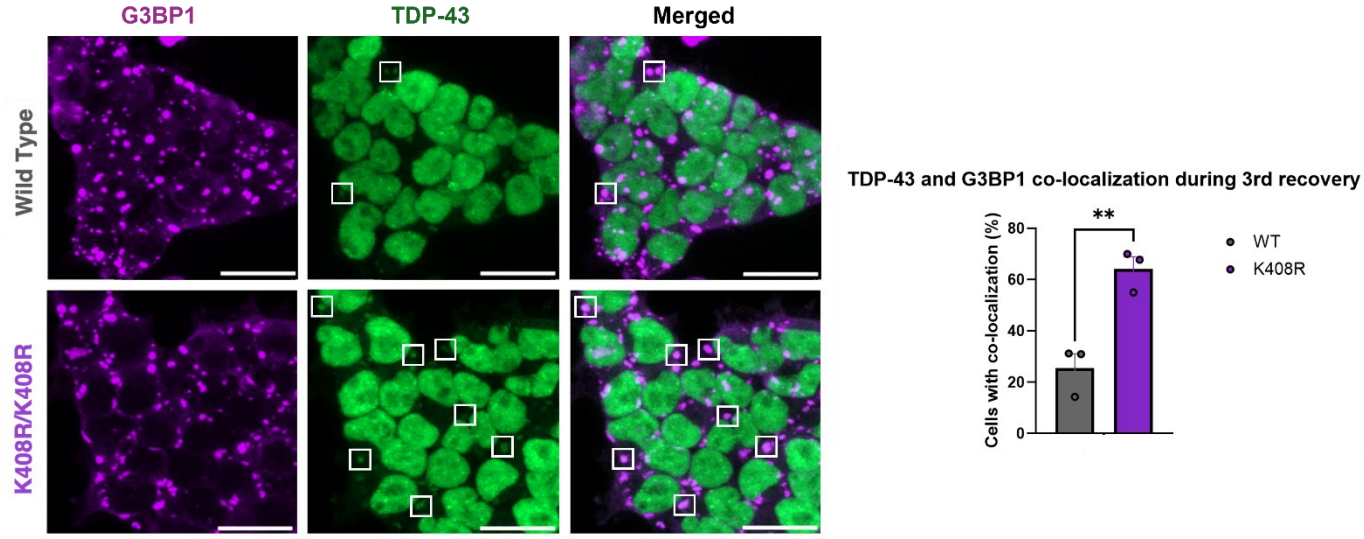

Figure 8. Cytoplasmic TDP-43 inclusions colocalize with G3BP1 stress granules during recovery. Representative images of WT and TDP-43$^{K408R/K408R}$ cells stained for G3BP1 and TDP-43. White boxes highlight regions of TDP-43 and G3BP1 co-localization. Scale bars represent 25µm. The bar graph quantifies the percentage of cells showing TDP-43 and G3BP1 co-localization during the third recovery period and shows a significant increase in co-localization in

TDP-43$^{K408R/K408R}$ cells compared to WT. Data is presented as mean ± SEM, **p<0.005, unpaired T-test data, N = 3.

8.6. Loss of SUMOylation may not affect nuclear TDP-43 mobility following repeated stress and recovery.

SUMOylation is well characterized to play roles in regulating protein solubility. Since we observed an increase in nuclear TDP-43 recovery bodies in TDP-43$^{K408R/K408R}$ neurons, we sought to determine whether SUMOylation affects TDP-43 mobility following repeated stress and recovery. Using Fluorescence Recovery After Photobleaching (FRAP), we photobleached 1/4 of the nucleus (where TDP-43 is localized) at 50% laser power. Fluorescence recovery of TDP-43 was monitored at 250 ms intervals post 30 minutes of stress and post 30 minutes of recovery. The total fluorescence intensity of the experiment was quantified using the Zen software. The intensity of the photobleached ROI was normalized to the non-photobleached region to account for fluctuations in fluorescence intensity. The intensity of the 5 pre-bleached images was normalized to 1 to achieve the maximum value of intensity and normalized to 0 upon bleaching to achieve the minimum value of intensity.

Comparative FRAP analysis between the initial stress and recovery cycle versus the third cycle showed differences in the mobility and recovery kinetics of WT TDP-43 and the K408R mutant within the photobleached ROI under repeated stress and recovery conditions (Figure 9A). To quantitatively assess these differences in TDP-43 mobility, we used GraphPad Prism to calculate and plot the Area Under the Curve (AUC) for each recovery curve, which reflects both the total fluorescence recovery and the overall mobility of TDP-43 over time. A higher AUC value

indicates a faster complete recovery, suggesting a higher mobility of TDP-43. Conversely, a lower AUC indicates less complete recovery, which suggests a lower mobility of TDP-43. We did not notice any changes in TDP-43 mobility between genotypes upon repeated stress and recovery (Figure 9B). However, we observed a significant decrease in TDP-43 mobility at the later stress and recovery time points. This indicates that the loss of SUMOylation does not affect the immediate mobility of TDP-43 during repeated stress and recovery but affects TDP-43 mobility at later time points following repeated stress exposures.

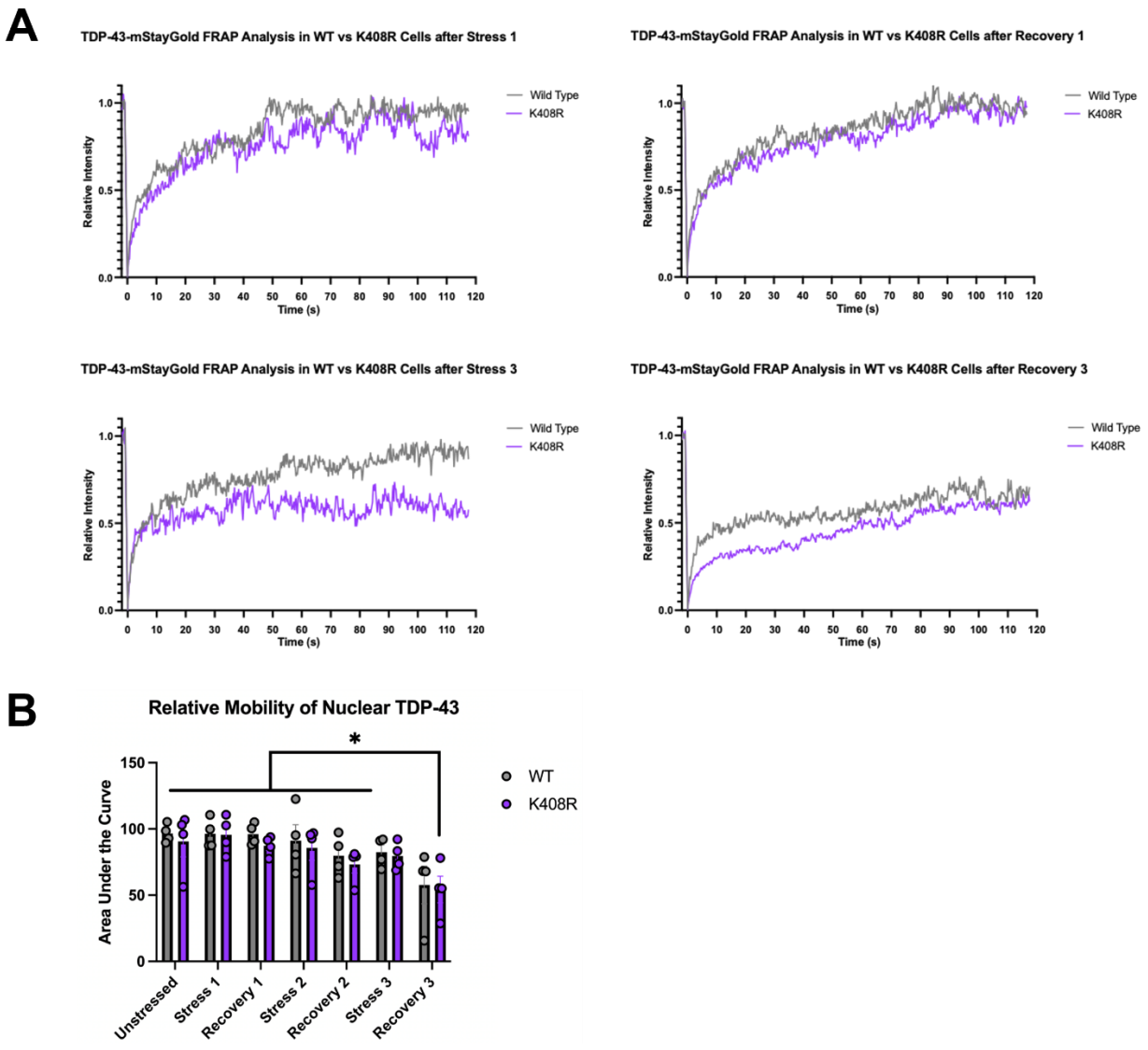

Figure 9. SUMOylation does not affect TDP-43 mobility during repeated stress and recovery. **(A)** Fluorescence recovery after photobleaching (FRAP) analysis of nuclear TDP-43 dynamics in live cells. Each panel compares the recovery profiles of WT TDP-43 (grey) and the K408R mutant (purple) over time upon stress 1, recovery 1, stress 3 and recovery 3 with 250 μM sodium arsenite treatment, normalized to pre-bleach fluorescence. Data points represent the mean fluorescence intensity from N = 4 (**B)** Relative Area Under the Curve (AUC) of each curve from panel A of WT and TDP-$43^{K408R/K408R}$ cells following 30-minute repeated stress with 250 μM sodium arsenite treatment and 30-minute recoveries, repeated 3 times. The bar graphs depict the area under the curve (AUC) for WT and K408R cells calculated using GraphPad Prism. Data are presented as mean ± SEM *$p<0.05$. N = 4. 2-way ANOVA with Fischer's LSD test. At least 1 cell was imaged and analyzed per replicate.

9. DISCUSSION

Summary of findings:

Our study aims to determine how the loss of TDP-43 SUMOylation with the K408R mutation affects the cellular stress response, including stress granule dynamics, TDP-43 subcellular localization, and protein mobility. Since SUMOylation of TDP-43 protects the cell from stress allowing for proper recovery, we found that loss of SUMOylation results in failed recovery from cellular stress. Upon acute stress, we observed impaired cellular stress response through delayed clearance of G3BP1 stress granules and accumulation of nuclear TDP-43 recovery bodies upon recovery. Following repeated rounds of stress, the formation and disassembly of stress granules were further exacerbated and led to the accumulation of nuclear TDP-43 foci, resulting in cytoplasmic TDP-43 aggregates in the K408R neurons. These findings support that stress-dependent SUMOylation is a critical regulator of TDP-43 proteostasis during cellular recovery. The combined effects of loss of SUMOylation and accumulation of cellular stress led to dysfunction in the stress response and formation of cytoplasmic TDP-43 aggregates.

Nuclear TDP-43 recovery bodies are RBM-45-positive.

Although TDP-43 has been found to associate with well-known nuclear bodies such as paraspeckles or anisosomes, our study identifies novel nuclear TDP-43 recovery bodies that are distinct in composition. While previous studies have primarily focused on nuclear body formation upon stress, our finding highlights the importance of exploring TDP-43 subcellular distribution during the recovery phase. Among the nuclear markers we tested, we found that a subset of these recovery bodies is RBM-45-positive, especially a greater proportion of co-localization in the K408R neurons. Family-based exome sequencing studies have found *RBM-45* as a candidate gene

for ALS and FTD[100]. However, no specific *RBM-45* mutation has been widely reported or validated. Thus, future genetic studies are needed to define mutations in *RBM-45* that cause ALS.

RBM-45 is a highly conserved RNA-binding protein with an RNA recognition motif (RRMs) and a homo-oligomerization (HOA) domain that mediates self-association and interaction with other RBPs[83]. This protein is highly expressed during neuronal development, differentiation, and proliferation. Although its biological functions are poorly understood, several studies have suggested that RBM-45 plays an important role in regulating splicing and nuclear-cytoplasmic shuttling RBP that interacts with TDP-43 and several other ALS-associated proteins like FUS, Matrin-3 and hnRNPA1[83]. However, upon mutation or stress conditions, *in vitro* studies have demonstrated that nuclear and cytoplasmic RBM-45 aggregates co-localize with TDP-43, ubiquitin, and stress granules. These aggregates have also been identified in ALS patients in motor neurons and glial cells in the CNS. Even more, patients harboring the C9ORF72 repeat expansion have a higher density of RBM-45-positive inclusions. Beyond the nervous system, RBM-45 also influences viral mRNA splicing in parvovirus B19 infection and has been linked to changes in lipid metabolism in cancer[106,107].

The co-localization of TDP-43 with RBM-45 inclusions suggests a potential interaction or shared pathway between these two proteins in the cellular stress response. We hypothesize that the formation of nuclear bodies act as hubs for RNA-binding proteins involved in recovery pathways. If the required SUMOylation of TDP-43 is lost, its clearance via the UPS may be compromised, leading to the accumulation of TDP-43 within nuclear bodies. Alternatively, given that both TDP-43 and RBM-45 play roles in RNA splicing, these RNA-binding proteins may be upregulating the splicing of stress-response genes to facilitate recovery from stress. However, further experiments should be performed to validate the interaction between TDP-43 and RBM-45. It is also important

to consider that the increased co-localization in K408R neurons may simply be a consequence of the higher number of foci. Thus, further quantification is needed by normalizing the proportion of cells with co-localization to the proportion of cells with TDP-43 foci, rather than the total number of cells.

Future steps are to characterize the components of these recovery bodies to understand the molecular pathways that are engaged during cellular stress and recovery. For example, we can perform split-Bio-ID coupled with mass spectrometry, which involves biotinylating and isolating proteins that interact with nuclear TDP-43 recovery bodies. In addition, we could identify interactors or post-translational modifications that are lost or gained when SUMOylation is blocked. Moreover, future studies could utilize live-cell imaging to monitor the subcellular localization of RBM-45 fused to RFP and TDP-43 tagged with mStayGold to assess the mobility of these nuclear bodies via FRAP compared to TDP-43 foci in the absence of RBM-45. Since both proteins play roles in RNA splicing, we could use quantitative PCR (qPCR) to detect changes in splicing patterns associated with the formation of these nuclear recovery bodies, providing insight into TDP-43 LOF phenotypes. By characterizing the composition of nuclear recovery bodies, we would be able to identify which proteins or RNA interact with TDP-43 during the early stages of stress recovery. Consequently, identifying the proteins that may facilitate cellular recovery from stress could lead to potential molecular targets for therapeutic intervention.

Repeated stress and recovery paradigm: Failure of G3BP1 stress granule assembly and disassembly.

Our repeated stress paradigm is critical for understanding neurodegenerative disease progression because it closely mimics the chronic, repetitive insults that neurons experience *in*

vivo (i.e., infections or physical injuries), rather than just a single acute stress and recovery event. A recent study shows SGs retain a biochemical memory of stress, and the memory continues to form even after the removal of stress and persists for 6-9 hours[108]. Therefore, this model allows us to observe how loss of SUMOylation exacerbates the cumulative effects of cellular stress without allowing the cells to fully recover, including dysfunction of stress granule clearance and re-activation, accumulation of nuclear TDP-43 recovery bodies, and cytoplasmic inclusions which are features seen in ALS.

Defects in stress granule dynamics have been implicated in the pathological aggregation of TDP-43 in ALS models. Multiple studies have shown that mutations in TDP-43, FUS and hnRNPA1 impair LLPS of stress granules, leading to aggregation[109–111]. Prolonged or repeated stress has been shown to overwhelm proteasomal clearance and autophagy pathways, impairing the disassembly of stress granules[112,113]. Consistent with these findings, our results indicate that repeated cycles of stress and recovery lead to an accumulation of persistent SGs, which is further exacerbated with the loss of TDP-43 SUMOylation.

Repeated stress and recovery paradigm: TDP-43 mislocalization and aggregation.

In our endogenous TDP-43 stress and recovery paradigm, we did not observe any significant mislocalization differences between WT and K408R neurons. However, when we overexpressed TDP-43 in HEK293Ts, we observed an accumulation of cytoplasmic TDP-43 aggregates. This discrepancy in TDP-43 localization may be explained by the use of different cell types and the amount of protein expressed.

Firstly, primary neurons are highly specialized non-dividing cells that tightly regulate protein expression and efficiently manage stress. However, HEK293T cells are immortalized cells

with simple protein quality control and may have less-regulated stress responses. Secondly, the overexpression of TDP-43 in cell lines introduces an additional "stress" that can overwhelm these quality-control systems. The combined burden of repeated stress recovery cycles and artificially high TDP-43 levels led to the mislocalization and the accumulation of TDP-43 aggregates. These findings align with other studies that have reported TDP-43 aggregation in cells with either overexpression or a mutated NLS, which promotes cytoplasmic mislocalization[101–103,114].

In the overexpression system, our data did not reach statistical significance when analyzing broad TDP-43 mislocalization in the K408R cells. This lack of significance could be due to under-sampling the number of cells, as 25 cells per replicate may be insufficient. Further detailed analysis is needed to quantify the number and size of cytoplasmic TDP-43 foci between WT and K408R cells, rather than broad mislocalization of TDP-43.

Although we did not reach significance, we visually observed an increase in TDP-43 aggregates in the K408R cells. There are several hypotheses that could explain an increase in cytoplasmic inclusions: Firstly, the loss of SUMOylation could prevent nuclear clearance via the UPS pathway. As a result, TDP-43 may translocate from the nucleus to the cytoplasm to find alternative degradation mechanisms within the cytoplasm. Secondly, previous findings in our lab show that the loss of SUMOylation promotes phosphorylation of TDP-43, possibly as a compensatory mechanism that may initially be protective but can eventually promote cytoplasmic aggregation[6]. Lastly, TDP-43 localizes to stress granules upon initial stress, however, TDP-43 eventually becomes aggregated in the cytoplasm as cells struggle to recover. Future studies should investigate whether the cytoplasmic TDP-43 co-localizes with stress granules and changes in stress granule number or size during repeated stress events.

Limitations:

While TDP-43 overexpression models are widely used to study its role in disease, there are several limitations. Firstly, it can lead to abnormally high levels of TDP-43 which could lead to non-specific toxicity and disrupt normal TDP-43 functions.[103,115]. Secondly, overexpression can force TDP-43 accumulation that does not capture the progressive nature of TDP-43 pathology[116]. They also may differ in composition, solubility and PTMs compared to aggregates in human disease[116].

Repeated stress and recovery paradigm: TDP-43 nuclear mobility.

Studies have shown that cellular stress can alter the dynamic interactions of TDP-43 with its nuclear environment. Using single-molecule tracking and biochemical assays, previous research demonstrated that TDP-43 is capable of recovering mobility after short arsenic-stress insults, while longer stress leads to an increase in immobility of TDP-43 in the nucleus and cytoplasm[117]. Similar to their findings, our FRAP data indicate that while the immediate mobility of TDP-43 remains unaltered, repeated stress induced a change in TDP-43 dynamics. This alteration could be due to an enhanced interaction of TDP-43 with other nuclear complexes or proteins, which could decrease protein mobility. Alternatively, TDP-43 could be phase transitioning from a liquid-like state to a more gel-like state through changes in LLPS.

Although there was no statistically significant difference in AUC between WT and K408R TDP-43 mobility, a marked difference in fluorescence recovery was observed when comparing stress condition 1 versus stress condition 3, as well as recovery condition 1 versus recovery condition 3 (Figure 9B). Therefore, it may be helpful to quantify this data using alternative parameters, such as half time or diffusion coefficient, which could provide a better representation

of alterations in TDP-43 mobility between genotypes. The half time (t½) is the time required for the fluorescence intensity in the bleached ROI to recover to 50% of its initial pre-bleach value, which reflects the kinetics of TDP-43 movement into the bleached area. The diffusion coefficient (D) is a parameter that quantifies how rapidly TDP-43 disperses within the nucleus. By calculating these parameters, we can more accurately characterize and compare the diffusion rate and overall kinetics of TDP-43 movement.

Additionally, SUMOylation is a generally short-lived modification and highly dynamic post-translational modification[117]. By our estimates, only 1% of TDP-43 is SUMOylated following stress. Given this transient nature, the photobleached region may predominantly target the non-SUMOylated fraction. This would potentially mask any differences in TDP-43 mobility between WT and K408R cells. To resolve this issue, we could express SUMOylated TDP-43 constitutively. A recent study generated a p53-SUMO fusion construct and showed that the protein fusion led to increased cytoplasmic localization[118]. Following this technique and the Suk et al paper, we could utilize the generated fusion of SUMO2 at the end of the C-terminal domain of TDP-43, as lysine 408 is six amino acids from the terminus. This fusion ensures consistent and precise SUMOylation near the desired site. Other studies have promoted SUMOylation of proteins by overexpressing E1 and E2 ligases such as Ubc9 to increase overall SUMOylation in the cell. However, overexpressing SUMO and its pathway may lead to pleiotropic effects, such as an increase in overall SUMOylated proteins or multiple SUMOylation sites on TDP-43. For example, overexpressing SUMO-1 or -2 in *C.elegans* disrupted movement and reproduction, suggesting that elevated SUMOylation can disrupt normal cellular functions[119]. Other studies have generated phospho-mimetics by mutating serine/threonine with aspartate/glutamate or employing acetyl-mimetic mutations in which lysine residues are substituted with glutamine[120,121]. However, this approach cannot be applied to

SUMOylation because SUMO molecules are too large which makes it difficult to mimic through single amino acid substitutions. While the SUMO fusion may appear advantageous among the other options, it also has its downsides. SUMO fusion relies on overexpressing TDP-43 and SUMO2 which can lead to cellular toxicity and does not accurately reflect endogenous conditions.

10. FUTURE DIRECTIONS AND CONCLUSION

In this initial study, we focused on the robust stressor sodium arsenite to elicit SUMOylated TDP-43 responses. However, there are several more clinically relevant insults, including heat shock, DNA damage, and C9ORF72 dipeptide repeats, that could be used to explore how TDP-43 SUMOylation plays roles in response to different stressors. For instance, SUMOylation has been shown to regulate DNA damage[122]. Inducing DNA damage via targeted ultraviolet light to generate DSBs will allow us to observe how SUMOylation affects real-time TDP-43 recruitment to sites of damage. Furthermore, testing more ALS-linked relevant stressors (i.e., C9ORF72 dipeptide repeats, a genetic cause of ALS)[123] would provide insight into whether the loss of TDP-43 SUMOylation and function leads to ALS-like pathology.

Future *in vivo* studies could investigate TDP-43 localization, LOF, and neuronal activity in K408R mice to monitor TDP-43 dynamics in real time. AAV vectors would be used to express fluorescently tagged TDP-43, such as using the TDP-43-mStayGold constructs or TDPREG (TDP-43 nuclear LOF construct). Recently, Wilkins et al. developed TDPREG, a cryptic reporter construct designed to track TDP-43 LOF activities by incorporating a splicing cassette containing a cryptic exon normally suppressed by TDP-43[124]. Normally, this exon is skipped and prevents protein production. However, when there is TDP-43 LOF, the exon is included during mRNA splicing, leading to the expression of a reporter protein specifically in affected cells. Future studies

could employ this construct to determine how TDP-43 SUMOylation affects its splicing function. For real-time visualization of TDP-43 dynamics in live mice, we will perform two-photon imaging of TDP-43 dynamics in WT vs K408R mice, under basal conditions or stressed conditions (i.e. aging, C9ORF72 repeats, heat shock, physical exercise). In parallel, assessing neuronal activity using calcium imaging or electrophysiology in K408R mice could reveal whether loss of TDP-43 SUMOylation correlates with synaptic transmission or behavioural deficits. Beyond imaging assays, transcriptomics, proteomics, and metabolomics in cells exposed to stress would allow us to track changes across multiple levels of regulation to understand the mechanisms that contribute to ALS pathogenesis.

Taken together, these studies will provide mechanistic insight into how blocking TDP-43 SUMOylation can alter TDP-43 localization, mobility and lead to pathology during stress and recovery *in vitro* and *in vivo*. By blocking SUMOylation of TDP-43 (K408R) and observing the consequences during cell stress and recovery, we will better understand the implications of SUMOylation in ALS pathogenesis. Ultimately, outcomes of this project can provide insight into the early and sequential mechanisms of ALS pathogenesis, which may provide insight into whether SUMOylation may serve as a target to therapeutically modify TDP-43 in disease.

11. APPENDIX I

References Cited

1. Suk, T. R. & Rousseaux, M. W. C. The role of TDP-43 mislocalization in amyotrophic lateral sclerosis. *Mol Neurodegener* **15**, 45 (2020).

2. Arai, T. *et al.* TDP-43 is a component of ubiquitin-positive tau-negative inclusions in frontotemporal lobar degeneration and amyotrophic lateral sclerosis. *Biochem Biophys Res Commun* **351**, 602–611 (2006).

3. Neumann, M. *et al.* Ubiquitinated TDP-43 in Frontotemporal Lobar Degeneration and Amyotrophic Lateral Sclerosis. *Science (1979)* **314**, 130–133 (2006).

4. Gasset-Rosa, F. *et al.* Cytoplasmic TDP-43 De-mixing Independent of Stress Granules Drives Inhibition of Nuclear Import, Loss of Nuclear TDP-43, and Cell Death. *Neuron* **102**, 339-357.e7 (2019).

5. Mann, J. R. *et al.* RNA Binding Antagonizes Neurotoxic Phase Transitions of TDP-43. *Neuron* **102**, 321-338.e8 (2019).

6. Suk, T. R. *et al.* A stress-dependent TDP-43 SUMOylation program preserves neuronal function. *Mol Neurodegeneration* **20**, 38 (2025)

7. Ivorra-Molla, E. *et al.* A monomeric StayGold fluorescent protein. *Nat Biotechnol* **42**, 1368–1371 (2024).

8. ALS Society of Canada. About ALS. (2018).

9. Hardiman, O. *et al.* Amyotrophic lateral sclerosis. *Nat Rev Dis Primers* **3**, 17071 (2017).

10. Chiò, A. *et al.* Prognostic factors in ALS: A critical review. *Amyotrophic Lateral Sclerosis* **10**, 310–323 (2009).

11. Taylor, J. P., Brown, R. H. & Cleveland, D. W. Decoding ALS: from genes to mechanism. *Nature* **539**, 197–206 (2016).

12. Mayo Clinic. Amyotrophic lateral sclerosis (ALS). *2024*.

13. Gordon, P. H., Mitsumoto, H. & Hays, A. P. Amyotrophic Lateral Sclerosis. *Science of Aging Knowledge Environment* **2003**, (2003).

14. Hinchcliffe, M. & Smith, A. Riluzole: real-world evidence supports significant extension of median survival times in patients with amyotrophic lateral sclerosis. *Degener Neurol Neuromuscul Dis* **Volume 7**, 61–70 (2017).

15. The ALS Association. Medications for Treating ALS. *ALS Association* (2025).

16. Wales, S. *et al.* Seminar Amyotrophic lateral sclerosis. *The Lancet* **377**, 942–955 (2011).

17. Jo, M. *et al.* The role of TDP-43 propagation in neurodegenerative diseases: integrating insights from clinical and experimental studies. *Exp Mol Med* **52**, 1652–1662 (2020).

18. Lee, Y.-B. *et al.* Cytoplasmic TDP-43 is involved in cell fate during stress recovery. *Hum Mol Genet* **31**, 166–175 (2021).

19. Luan, W. *et al.* Early activation of cellular stress and death pathways caused by cytoplasmic TDP-43 in the rNLS8 mouse model of ALS and FTD. *Mol Psychiatry* **28**, 2445–2461 (2023).

20. Knopman, D. S. *et al.* Alzheimer disease. *Nat Rev Dis Primers* **7**, 33 (2021).

21. Goedert, M. Alpha-synuclein and neurodegenerative diseases. *Nat Rev Neurosci* **2**, 492–501 (2001).

22. Nguyen, H. P., Van Broeckhoven, C. & van der Zee, J. ALS Genes in the Genomic Era and their Implications for FTD. *Trends in Genetics* **34**, 404–423 (2018).

23. Ghasemi, M. & Brown, R. H. Genetics of Amyotrophic Lateral Sclerosis. *Cold Spring Harb Perspect Med* **8**, a024125 (2018).

24. Akçimen, F. *et al.* Amyotrophic lateral sclerosis: translating genetic discoveries into therapies. *Nat Rev Genet* **24**, 642–658 (2023).

25. Mackenzie, I. R. A. *et al.* Pathological TDP-43 distinguishes sporadic amyotrophic lateral sclerosis from amyotrophic lateral sclerosis with *SOD1* mutations. *Ann Neurol* **61**, 427–434 (2007).

26. Renton, A. E. *et al.* A Hexanucleotide Repeat Expansion in C9ORF72 Is the Cause of Chromosome 9p21-Linked ALS-FTD. *Neuron* **72**, 257–268 (2011).

27. DeJesus-Hernandez, M. *et al.* Expanded GGGGCC Hexanucleotide Repeat in Noncoding Region of C9ORF72 Causes Chromosome 9p-Linked FTD and ALS. *Neuron* **72**, 245–256 (2011).

28. Gendron, T. F. *et al.* Antisense transcripts of the expanded C9ORF72 hexanucleotide repeat form nuclear RNA foci and undergo repeat-associated non-ATG translation in c9FTD/ALS. *Acta Neuropathol* **126**, 829–844 (2013).

29. Donnelly, C. J. *et al.* RNA Toxicity from the ALS/FTD C9ORF72 Expansion Is Mitigated by Antisense Intervention. *Neuron* **80**, 415–428 (2013).

30. Ash, P. E. A. *et al.* Unconventional Translation of C9ORF72 GGGGCC Expansion Generates Insoluble Polypeptides Specific to c9FTD/ALS. *Neuron* **77**, 639–646 (2013).

31. Benajiba, L. *et al. TARDBP* mutations in motoneuron disease with frontotemporal lobar degeneration. *Ann Neurol* **65**, 470–473 (2009).

32. Corrado, L. *et al.* High frequency of *TARDBP* gene mutations in Italian patients with amyotrophic lateral sclerosis. *Hum Mutat* **30**, 688–694 (2009).

33. Conforti, F. L. *et al.* TARDBP gene mutations in south Italian patients with amyotrophic lateral sclerosis. *J Neurol Neurosurg Psychiatry* **82**, 587–588 (2011).

34. Suzuki, N., Nishiyama, A., Warita, H. & Aoki, M. Genetics of amyotrophic lateral sclerosis: seeking therapeutic targets in the era of gene therapy. *J Hum Genet* **68**, 131–152 (2023).

35. Chapman, L., Cooper-Knock, J. & Shaw, P. J. Physical activity as an exogenous risk factor for amyotrophic lateral sclerosis: a review of the evidence. *Brain* **146**, 1745–1757 (2023).

36. Mattsson, P., Lönnstedt, I., Nygren, I. & Askmark, H. Physical fitness, but not muscle strength, is a risk factor for death in amyotrophic lateral sclerosis at an early age. *J Neurol Neurosurg Psychiatry* **83**, 390–394 (2012).

37. McKay, K. A. *et al.* Military service and related risk factors for amyotrophic lateral sclerosis. *Acta Neurol Scand* **143**, 39–50 (2021).

38. Franz, C. K. *et al.* Impact of traumatic brain injury on amyotrophic lateral sclerosis: from bedside to bench. *J Neurophysiol* **122**, 1174–1185 (2019).

39. Chen, H., Richard, M., Sandler, D. P., Umbach, D. M. & Kamel, F. Head Injury and Amyotrophic Lateral Sclerosis. *Am J Epidemiol* **166**, 810–816 (2007).

40. Ash, P. E. A. *et al.* Heavy Metal Neurotoxicants Induce ALS-Linked TDP-43 Pathology. *Toxicological Sciences* **167**, 105–115 (2019).

41. Andrew, A. *et al.* Pesticides applied to crops and amyotrophic lateral sclerosis risk in the U.S. *Neurotoxicology* **87**, 128–135 (2021).

42. Sola, P. *et al.* New Insights into the Viral Theory of Amyotrophic Lateral Sclerosis: Study on the Possible Role of Kaposi's Sarcoma-Associated Virus/Human Herpesvirus 8. *Eur Neurol* **47**, 108–112 (2002).

43. Sola, P., Merelli, E., Levani, M., Giovannetti, R. & Barozzi, P. Human herpes virus 6 (HHV-6) in amyotrophic lateral sclerosis: a polymerase chain reaction (PCR) study. *Eur J Neurol* **3**, 315–318 (1996).

44. Berger, M. M. *et al.* Detection and cellular localization of enterovirus RNA sequences in spinal cord of patients with ALS. *Neurology* **54**, 20–20 (2000).

45. McCormick, A. L., Brown, R. H., Cudkowicz, M. E., Al-Chalabi, A. & Garson, J. A. Quantification of reverse transcriptase in ALS and elimination of a novel retroviral candidate. *Neurology* **70**, 278–283 (2008).

46. Freibaum, B. D., Chitta, R. K., High, A. A. & Taylor, J. P. Global Analysis of TDP-43 Interacting Proteins Reveals Strong Association with RNA Splicing and Translation Machinery. *J Proteome Res* **9**, 1104–1120 (2010).

47. Colombrita, C. *et al.* TDP-43 is recruited to stress granules in conditions of oxidative insult. *J Neurochem* **111**, 1051–1061 (2009).

48. Ayala, Y. M. *et al.* Structural determinants of the cellular localization and shuttling of TDP-43. *J Cell Sci* **121**, 3778–3785 (2008).

49. Ling, J. P., Pletnikova, O., Troncoso, J. C. & Wong, P. C. TDP-43 repression of nonconserved cryptic exons is compromised in ALS-FTD. *Science (1979)* **349**, 650–655 (2015).

50. Brown, A.-L. *et al.* TDP-43 loss and ALS-risk SNPs drive mis-splicing and depletion of UNC13A. *Nature* **603**, 131–137 (2022).

51. Ma, X. R. *et al.* TDP-43 represses cryptic exon inclusion in the FTD–ALS gene UNC13A. *Nature* **603**, 124–130 (2022).

52. Baughn, M. W. *et al.* Mechanism of *STMN2* cryptic splice-polyadenylation and its correction for TDP-43 proteinopathies. *Science (1979)* **379**, 1140–1149 (2023).

53. Krus, K. L. *et al.* Loss of Stathmin-2, a hallmark of TDP-43-associated ALS, causes motor neuropathy. *Cell Rep* **39**, 111001 (2022).

54. Ayala, Y. M. *et al.* TDP-43 regulates its mRNA levels through a negative feedback loop. *EMBO J* **30**, 277–288 (2011).

55. Huang, C., Yan, S. & Zhang, Z. Maintaining the balance of TDP-43, mitochondria, and autophagy: a promising therapeutic strategy for neurodegenerative diseases. *Transl Neurodegener* **9**, 40 (2020).

56. Buratti, E. Multiple roles of TDP-43 in gene expression, splicing regulation, and human disease. *Frontiers in Bioscience* **13**, 867 (2008).

57. Jo, M. *et al.* The role of TDP-43 propagation in neurodegenerative diseases: integrating insights from clinical and experimental studies. *Exp Mol Med* **52**, 1652–1662 (2020).

58. Archbold, H. C. *et al.* TDP43 nuclear export and neurodegeneration in models of amyotrophic lateral sclerosis and frontotemporal dementia. *Sci Rep* **8**, 4606 (2018).

59. Afroz, T. *et al.* Functional and dynamic polymerization of the ALS-linked protein TDP-43 antagonizes its pathologic aggregation. *Nat Commun* **8**, 45 (2017).

60. Lim, L., Wei, Y., Lu, Y. & Song, J. ALS-Causing Mutations Significantly Perturb the Self-Assembly and Interaction with Nucleic Acid of the Intrinsically Disordered Prion-Like Domain of TDP-43. *PLoS Biol* **14**, e1002338 (2016).

61. Van Deerlin, V. M. *et al.* TARDBP mutations in amyotrophic lateral sclerosis with TDP-43 neuropathology: a genetic and histopathological analysis. *Lancet Neurol* **7**, 409–416 (2008).

62. Gopal, P. P., Nirschl, J. J., Klinman, E. & Holzbaur, E. L. F. Amyotrophic lateral sclerosis-linked mutations increase the viscosity of liquid-like TDP-43 RNP granules in neurons. *Proceedings of the National Academy of Sciences* **114**, (2017).

63. Arai, T. *et al.* Phosphorylated and cleaved TDP-43 in ALS, FTLD and other neurodegenerative disorders and in cellular models of TDP-43 proteinopathy. *Neuropathology* **30**, 170–181 (2010).

64. Riancho, J. *et al.* ALS-derived fibroblasts exhibit reduced proliferation rate, cytoplasmic TDP-43 aggregation and a higher susceptibility to DNA damage. *J Neurol* **267**, 1291–1299 (2020).

65. Cykowski, M. D. *et al.* Phosphorylated TDP-43 (pTDP-43) aggregates in the axial skeletal muscle of patients with sporadic and familial amyotrophic lateral sclerosis. *Acta Neuropathol Commun* **6**, 28 (2018).

66. Cutler, A. A., Ewachiw, T. E., Corbet, G. A., Parker, R. & Olwin, B. B. Myo-granules Connect Physiology and Pathophysiology. *J Exp Neurosci* **13**, (2019).

67. Gal, J., Ström, A.-L., Kilty, R., Zhang, F. & Zhu, H. p62 Accumulates and Enhances Aggregate Formation in Model Systems of Familial Amyotrophic Lateral Sclerosis. *Journal of Biological Chemistry* **282**, 11068–11077 (2007).

68. Fulda, S., Gorman, A. M., Hori, O. & Samali, A. Cellular Stress Responses: Cell Survival and Cell Death. *Int J Cell Biol* **2010**, 1–23 (2010).

69. Galluzzi, L., Yamazaki, T. & Kroemer, G. Linking cellular stress responses to systemic homeostasis. *Nat Rev Mol Cell Biol* **19**, 731–745 (2018).

70. Wang, Y.-C. *et al.* Severe cellular stress drives apoptosis through a dual control mechanism independently of p53. *Cell Death Discov* **8**, 282 (2022).

71. Yan, X. *et al.* Intra-condensate demixing of TDP-43 inside stress granules generates pathological aggregates. Preprint at https://doi.org/10.1101/2024.01.23.576837 (2024).

72. Lee, Y.-B. *et al.* Cytoplasmic TDP-43 is involved in cell fate during stress recovery. *Hum Mol Genet* **31**, 166–175 (2021).

73. Dewey, C. M. *et al.* TDP-43 Is Directed to Stress Granules by Sorbitol, a Novel Physiological Osmotic and Oxidative Stressor. *Mol Cell Biol* **31**, 1098–1108 (2011).

74. Ratti, A. *et al.* Chronic stress induces formation of stress granules and pathological TDP-43 aggregates in human ALS fibroblasts and iPSC-motoneurons. *Neurobiol Dis* **145**, 105051 (2020).

75. Colombrita, C. *et al.* TDP-43 is recruited to stress granules in conditions of oxidative insult. *J Neurochem* **111**, 1051–1061 (2009).

76. Hofmann, S., Kedersha, N., Anderson, P. & Ivanov, P. Molecular mechanisms of stress granule assembly and disassembly. *Biochimica et Biophysica Acta (BBA) - Molecular Cell Research* **1868**, 118876 (2021).

77. Khalfallah, Y. *et al.* TDP-43 regulation of stress granule dynamics in neurodegenerative disease-relevant cell types. *Sci Rep* **8**, 7551 (2018).

78. Sidibé, H. *et al.* TDP-43 stabilizes *G3BP1* mRNA: relevance to amyotrophic lateral sclerosis/frontotemporal dementia. *Brain* **144**, 3461–3476 (2021).

79. Mateju, D. *et al.* An aberrant phase transition of stress granules triggered by misfolded protein and prevented by chaperone function. *EMBO J* **36**, 1669–1687 (2017).

80. Wang, C. *et al.* Stress Induces Dynamic, Cytotoxicity-Antagonizing TDP-43 Nuclear Bodies via Paraspeckle LncRNA NEAT1-Mediated Liquid-Liquid Phase Separation. *Mol Cell* **79**, 443-458.e7 (2020).

81. Shelkovnikova, T. A. *et al.* Protective paraspeckle hyper-assembly downstream of TDP-43 loss of function in amyotrophic lateral sclerosis. *Mol Neurodegener* **13**, 30 (2018).

82. Yu, H. *et al.* HSP70 chaperones RNA-free TDP-43 into anisotropic intranuclear liquid spherical shells. *Science (1979)* **371**, (2021).

83. Collins, M., Li, Y. & Bowser, R. RBM45 associates with nuclear stress bodies and forms nuclear inclusions during chronic cellular stress and in neurodegenerative diseases. Preprint at https://doi.org/10.1101/856880 (2019).

84. Jung, K. H. *et al.* Nuclear bodies protect phase separated proteins from degradation in stressed proteome. Preprint at https://doi.org/10.7554/eLife.88237.1 (2023).

85. Duan, Y. *et al.* PARylation regulates stress granule dynamics, phase separation, and neurotoxicity of disease-related RNA-binding proteins. *Cell Res* **29**, 233–247 (2019).

86. Cohen, T. J. *et al.* An acetylation switch controls TDP-43 function and aggregation propensity. *Nat Commun* **6**, 5845 (2015).

87. Garcia Morato, J. *et al.* Sirtuin-1 sensitive lysine-136 acetylation drives phase separation and pathological aggregation of TDP-43. *Nat Commun* **13**, 1223 (2022).

88. Celen, A. B. & Sahin, U. Sumoylation on its 25th anniversary: mechanisms, pathology, and emerging concepts. *FEBS J* **287**, 3110–3140 (2020).

89. Ilic, D., Magnussen, H. M. & Tirard, M. Stress - Regulation of SUMO conjugation and of other Ubiquitin-Like Modifiers. *Semin Cell Dev Biol* **132**, 38–50 (2022).

90. XU, Z. & AU, S. W. N. Mapping residues of SUMO precursors essential in differential maturation by SUMO-specific protease, SENP1. *Biochemical Journal* **386**, 325–330 (2005).

91. Hendriks, I. A. *et al.* Site-specific characterization of endogenous SUMOylation across species and organs. *Nat Commun* **9**, 2456 (2018).

92. Guerrero, F., Ciragan, A. & Iwaï, H. Tandem SUMO fusion vectors for improving soluble protein expression and purification. *Protein Expr Purif* **116**, 42–49 (2015).

93. Evdokimov, E., Sharma, P., Lockett, S. J., Lualdi, M. & Kuehn, M. R. Loss of SUMO1 in mice affects RanGAP1 localization and formation of PML nuclear bodies, but is not lethal as it can be compensated by SUMO2 or SUMO3. *J Cell Sci* **121**, 4106–4113 (2008).

94. Pichler, A. & Melchior, F. Ubiquitin-Related Modifier SUMO1 and Nucleocytoplasmic Transport. *Traffic* **3**, 381–387 (2002).

95. Enserink, J. M. Sumo and the cellular stress response. *Cell Div* **10**, 4 (2015).

96. Cheng, X. Protein SUMOylation and phase separation: partners in stress? *Trends Biochem Sci* **48**, 417–419 (2023).

97. Han, J., Mu, Y. & Huang, J. Preserving genome integrity: The vital role of SUMO-targeted ubiquitin ligases. *Cell Insight* **2**, 100128 (2023).

98. Kumar, R., González-Prieto, R., Xiao, Z., Verlaan-de Vries, M. & Vertegaal, A. C. O. The STUbL RNF4 regulates protein group SUMOylation by targeting the SUMO conjugation machinery. *Nat Commun* **8**, 1809 (2017).

99. Saitoh, H. & Hinchey, J. Functional heterogeneity of small ubiquitin-related protein modifiers SUMO-1 versus SUMO-2/3. *Journal of Biological Chemistry* **275**, 6252–6258 (2000).

100. van der Zee, J. *et al.* Family-based exome sequencing identifies RBM45 as a possible candidate gene for frontotemporal dementia and amyotrophic lateral sclerosis. *Neurobiol Dis* **156**, 105421 (2021).

101. Yamashita, M. *et al.* Distinct pathways leading to TDP-43-induced cellular dysfunctions. *Hum Mol Genet* **23**, 4345–4356 (2014).

102. Guo, W. *et al.* An ALS-associated mutation affecting TDP-43 enhances protein aggregation, fibril formation and neurotoxicity. *Nat Struct Mol Biol* **18**, 822–830 (2011).

103. Barmada, S. J. *et al.* Cytoplasmic Mislocalization of TDP-43 Is Toxic to Neurons and Enhanced by a Mutation Associated with Familial Amyotrophic Lateral Sclerosis. *The Journal of Neuroscience* **30**, 639–649 (2010).

104. Colombrita, C. *et al.* TDP-43 is recruited to stress granules in conditions of oxidative insult. *J Neurochem* **111**, 1051–1061 (2009).

105. Igaz, L. M. *et al.* Expression of TDP-43 C-terminal Fragments in Vitro Recapitulates Pathological Features of TDP-43 Proteinopathies. *Journal of Biological Chemistry* **284**, 8516–8524 (2009).

106. Wang, C. *et al.* RBM45 reprograms lipid metabolism promoting hepatocellular carcinoma via Rictor and ACSL1/ACSL4. *Oncogene* **43**, 328–340 (2024).

107. Wang, J. *et al.* RNA Binding Motif Protein RBM45 Regulates Expression of the 11-Kilodalton Protein of Parvovirus B19 through Binding to Novel Intron Splicing Enhancers. *mBio* **11**, (2020).

108. Benman, W., Iyengar, P., Mumford, T., Huang, Z. & Bugaj, L. J. Multiplexed dynamic control of temperature to probe and observe mammalian cells. Preprint at https://doi.org/10.1101/2024.02.18.580877 (2024).

109. Molliex, A. *et al.* Phase Separation by Low Complexity Domains Promotes Stress Granule Assembly and Drives Pathological Fibrillization. *Cell* **163**, 123–133 (2015).

110. Patel, A. *et al.* A Liquid-to-Solid Phase Transition of the ALS Protein FUS Accelerated by Disease Mutation. *Cell* **162**, 1066–1077 (2015).

111. Conicella, A. E., Zerze, G. H., Mittal, J. & Fawzi, N. L. ALS Mutations Disrupt Phase Separation Mediated by α-Helical Structure in the TDP-43 Low-Complexity C-Terminal Domain. *Structure* **24**, 1537–1549 (2016).

112. Molliex, A. *et al.* Phase Separation by Low Complexity Domains Promotes Stress Granule Assembly and Drives Pathological Fibrillization. *Cell* **163**, 123–133 (2015).

113. Barmada, S. J. *et al.* Autophagy induction enhances TDP43 turnover and survival in neuronal ALS models. *Nat Chem Biol* **10**, 677–685 (2014).

114. Chou, C.-C. *et al.* TDP-43 pathology disrupts nuclear pore complexes and nucleocytoplasmic transport in ALS/FTD. *Nat Neurosci* **21**, 228–239 (2018).

115. Winton, M. J. *et al.* Disturbance of Nuclear and Cytoplasmic TAR DNA-binding Protein (TDP-43) Induces Disease-like Redistribution, Sequestration, and Aggregate Formation. *Journal of Biological Chemistry* **283**, 13302–13309 (2008).

116. Ling, S.-C., Polymenidou, M. & Cleveland, D. W. Converging Mechanisms in ALS and FTD: Disrupted RNA and Protein Homeostasis. *Neuron* **79**, 416–438 (2013).

117. Streit, L. *et al.* Stress induced TDP-43 mobility loss independent of stress granules. *Nat Commun* **13**, 5480 (2022).

118. Santiago, A., Li, D., Zhao, L. Y., Godsey, A. & Liao, D. p53 SUMOylation promotes its nuclear export by facilitating its release from the nuclear export receptor CRM1. *Mol Biol Cell* **24**, 2739–2752 (2013).

119. Rytinki, M. M. *et al.* Overexpression of SUMO perturbs the growth and development of Caenorhabditis elegans. *Cellular and Molecular Life Sciences* **68**, 3219–3232 (2011).

120. Cohen, T. J. *et al.* An acetylation switch controls TDP-43 function and aggregation propensity. *Nat Commun* **6**, 5845 (2015).

121. Wang, A. *et al.* A single N-terminal phosphomimic disrupts TDP-43 polymerization, phase separation, and RNA splicing. *EMBO J* **37**, (2018).

122. Sarangi, P. & Zhao, X. SUMO-mediated regulation of DNA damage repair and responses. *Trends Biochem Sci* **40**, 233–242 (2015).

123. Cook, C. N. *et al. C9orf72* poly(GR) aggregation induces TDP-43 proteinopathy. *Sci Transl Med* **12**, (2020).

124. Wilkins, O. G. *et al.* Creation of de novo cryptic splicing for ALS and FTD precision medicine. *Science (1979)* **386**, 61–69 (2024).

12. APPENDIX II

Table 1. Entry vectors for TDP-43 EGFP and TDP-43-mStayGold construct cloning

Gene Name	Antibiotic	Vector backbone	Additional cloning required?	Sequencing primer	Approx. size (bp)
pLEX307 TDP-43-mStayGold (WT)	Ampicillin	pEntr	Yes – cloned into pLEX307 construct	M13F	10358 bp
pLEX307 TDP-43-mStayGold (K408R)	Ampicillin	pEntr	Yes – cloned into pLEX307 construct	M13F	10358 bp
pLEX307 TDP-43-EGFP (WT)	Ampicillin	pEntr	Yes – cloned into pLEX307 construct	M13F	10426 bp
pLEX307 TDP-43-EGFP (K408R)	Ampicillin	pEntr	Yes – cloned into pLEX307 construct	M13F	10426 bp

Table 2. Antibodies

Antibody	Company	Catalog no.	Species	Dilution
TDP-43 (C-terminal)	Proteintech	12892-1-AP	Rabbit polyclonal	IF: 1:250
G3BP1	Santa Cruz Biotechnology	Sc-81940	Mouse monoclonal	IF: 1:1000
PSPC-1	Santa Cruz Biotechnology	Sc-374181	Mouse monoclonal	IF: 1:200
UBI-1	ThermoFischer	13-1600	Mouse monoclonal	IF: 1:250
RBM-45	Santa Cruz Biotechnology	Sc-515495	Mouse monoclonal	IF: 1:100
Alexa Fluor 488, Secondary	ThermoFischer	A-11034	Rabbit	IF: 1:1000
Alexa Fluor 568, Secondary	ThermoFischer	A10037	Mouse	IF: 1:1000
Rabbit-HRP	Jackson ImmunoResearch (Cedarlane)	711-035-152	Rabbit	IF: 1:1000

13. APPENDIX III

Permission to reprint published manuscripts

Suk, T.R., Part, C.E., **Zhang, J.L.**, Nguyen, T.T., Heer, M.M., Caballero-Gómez, A., Grybas, V.S., McKeever, P.M., Nguyen, B., Ali, T., Callaghan, S.M., Woulfe, J.M., Robertson, J., and Rousseaux, M.W.C. A stress-dependent TDP-43 SUMOylation program preserves neuronal function. (2025) – Molecular Neurodegeneration **20**. DOI: https://doi.org/10.1186/s13024-025-00826-z

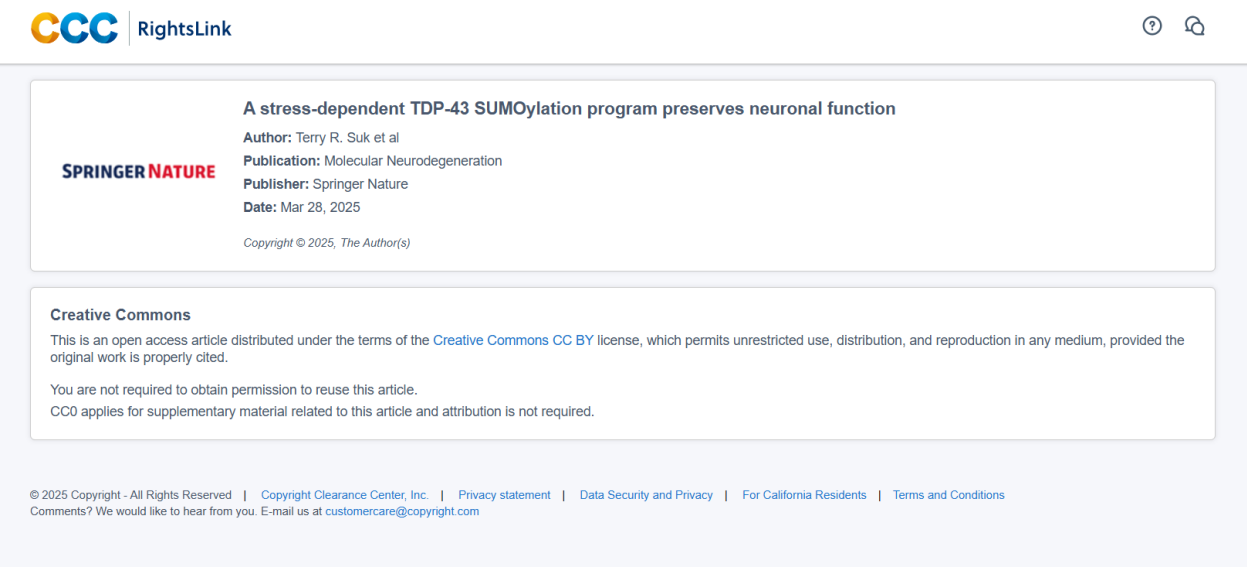

CCC RightsLink

SPRINGER NATURE

A stress-dependent TDP-43 SUMOylation program preserves neuronal function

Author: Terry R. Suk et al
Publication: Molecular Neurodegeneration
Publisher: Springer Nature
Date: Mar 28, 2025

Copyright © 2025, The Author(s)

Creative Commons

This is an open access article distributed under the terms of the Creative Commons CC BY license, which permits unrestricted use, distribution, and reproduction in any medium, provided the original work is properly cited.

You are not required to obtain permission to reuse this article.
CC0 applies for supplementary material related to this article and attribution is not required.

Suk, T.R. and Rousseaux, M.W.C. The role of TDP-43 mislocalization in amyotrophic lateral sclerosis. (2020) – Molecular Neurodegeneration **15**. DOI: https://doi.org/10.1186/s13024-020-00397-1

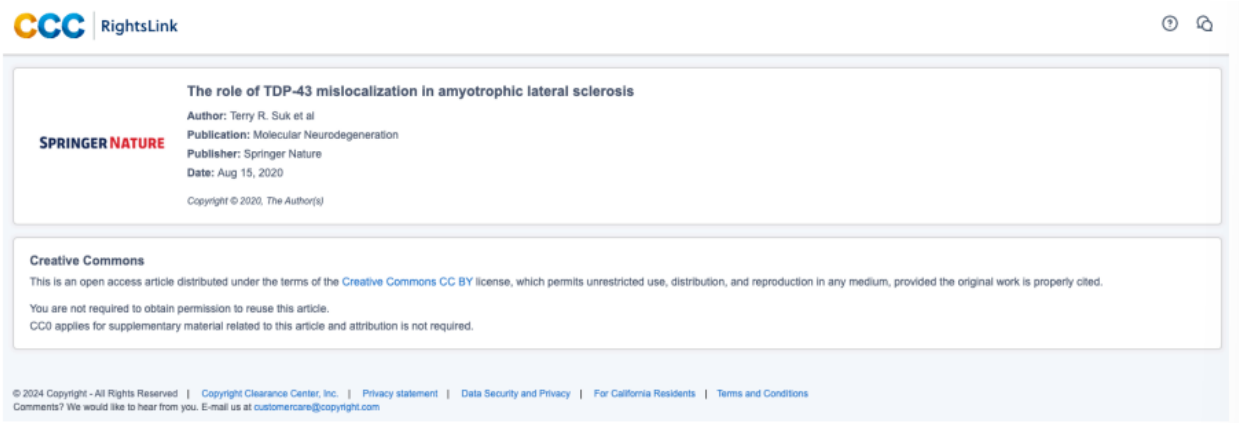

14. APPENDIX IV

Appended Articles

Suk, T.R., Part, C.E., Zhang, J.L. et al. A stress-dependent TDP-43 SUMOylation program preserves neuronal function. Mol Neurodegeneration **20**, 38 (2025). https://doi.org/10.1186/s13024-025-00826-z

Contribution: I performed immunofluorescence assays, confocal microscopy, and analysis. My overall contribution was ~8-10%

Suk et al. Molecular Neurodegeneration (2025) 20:38
https://doi.org/10.1186/s13024-025-00826-z

Molecular Neurodegeneration

RESEARCH ARTICLE Open Access

A stress-dependent TDP-43 SUMOylation program preserves neuronal function

Terry R. Suk[1,2,3,4], Caroline E. Part[1,2,3,4], Jenny L. Zhang[1,2,3,4†], Trina T. Nguyen[1,2,3,4†], Meghan M. Heer[1,2,3,4], Alejandro Caballero-Gómez[1,2,3,4], Veronica S. Grybas[1,2,3,4], Paul M. McKeever[5], Benjamin Nguyen[1,2,3,4], Tahir Ali[1,2,3,4], Steve M. Callaghan[1,2,3,4], John M. Woulfe[1,2,6,7,8], Janice Robertson[5] and Maxime W. C. Rousseaux[1,2,3,4*]

Abstract

Amyotrophic Lateral Sclerosis (ALS) and Frontotemporal Dementia (FTD) are overwhelmingly linked to TDP-43 dysfunction. Mutations in TDP-43 are rare, indicating that the progressive accumulation of exogenous factors – such as cellular stressors – converge on TDP-43 to play a key role in disease pathogenesis. Post translational modifications such as SUMOylation play essential roles in response to such exogenous stressors. We therefore set out to understand how SUMOylation may regulate TDP-43 in health and disease. We find that TDP-43 is regulated dynamically via SUMOylation in response to cellular stressors. When this process is blocked in vivo, we note age-dependent TDP-43 pathology and sex-specific behavioral deficits linking TDP-43 SUMOylation with aging and disease. We further find that SUMOylation is correlated with human aging and disease states. Collectively, this work presents TDP-43 SUMOylation as an early physiological response to cellular stress, disruption of which may confer a risk for TDP-43 proteinopathy.

Keywords ALS, FTD, TDP-43, SUMOylation, Pathology, Mouse Model, Post Translational Modifications, Stress

Introduction

Altered proteostasis is one of the key hallmarks of aging and is particularly prevalent in neurodegenerative diseases [1]. Despite the highly heterogenous nature of neurodegenerative diseases – likely owing to the extreme genetic and environmental diversity acting upon individuals – a select few proteins are recurringly implicated in pathology [2]. TDP-43 is an essential RNA binding protein notorious for its involvement in neurodegenerative diseases including Amyotrophic Lateral Sclerosis (ALS) and Frontotemporal Dementia (FTD). In a diseased state, TDP-43 is found mislocalized from the nucleus and aggregated in the cytoplasm of neurons within the central nervous system (CNS) in ~ 97% and ~ 45% of ALS and FTD cases, respectively [3, 4]. Additionally, ALS and FTD exist on a clinical and genetic spectrum linked by TDP-43 dysfunction often referred together as ALS/FTD [5]. Beyond ALS/FTD, TDP-43 pathology is increasingly

† Jenny L. Zhang and Trina T. Nguyen contributed equally to this work.

*Correspondence:
Maxime W. C. Rousseaux
max.rousseaux@uottawa.ca
[1] University of Ottawa Brain and Mind Research Institute, Ottawa, ON, Canada
[2] Department of Cellular and Molecular Medicine, University of Ottawa, Ottawa, ON, Canada
[3] Eric Poulin Center for Neuromuscular Diseases, Ottawa, ON, Canada
[4] Ottawa Institute of Systems Biology, Ottawa, ON, Canada
[5] Tanz Centre for Research in Neurodegenerative Diseases, University of Toronto, Toronto, ON, Canada
[6] The Ottawa Hospital Research Institute, the Ottawa Hospital, Ottawa, ON, Canada
[7] Department of Pathology and Laboratory Medicine, University of Ottawa, Ottawa, ON, Canada
[8] Department of Biochemistry, Microbiology, and Immunology, University of Ottawa, Ottawa, ON, Canada

linked to other neurological disorders including Limbic-predominant Age-related TDP-43 Encephalopathy (LATE), Alzheimer's Disease (AD), Chronic Traumatic Encephalopathy (CTE), and Stroke [6–9]. Thus, TDP-43 pathology has garnered much attention to better understand the causes of these diseases and to uncover potential routes of therapeutic intervention.

The accumulation of cytoplasmic TDP-43 aggregates is considered a late-stage event in neurodegeneration. Increasing evidence suggests that the partial mislocalization or complete depletion of TDP-43 from the nucleus to the cytoplasm is an early event in ALS/FTD pathogenesis, functioning independently – however tightly associated – with aggregation [10–16]. As a result, recent efforts have focused on the outcomes of TDP-43 mislocalization as early markers of dysfunction and/or mechanisms driving disease. Indeed, loss of function due to mislocalization of TDP-43 causes aberrant cryptic splicing in genes including *STMN2* and *UNC13A* that drive the progression of ALS [12–15, 17]. To wit, cryptic mis-splicing of *STMN2* was recently found to correlate strongly with TDP-43 pathology [18, 19]. Additionally, once in the cytoplasm, TDP-43 can exert additional toxicity through gain of function effects by sequestering critical proteins into cytoplasmic aggregates thus disrupting crucial pathways leading to cellular demise [11, 20]. Together, dysregulation of TDP-43 is sufficient to drive neuronal dysfunction ultimately leading to neurodegeneration. However, the mechanisms instigating TDP-43 pathogenesis remain convoluted.

Despite the overwhelming prevalence of TDP-43 pathology in ALS/FTD and related diseases, mutations in the gene encoding TDP-43 (*TARDBP*) are only present in less than 1% of all ALS and FTD cases [21]. It is becoming evident that not one, but many genetic and/or environmental factors affect pathways converging on TDP-43 in ALS/FTD. Many ALS/FTD causative genes exert toxicity by disruption of key pathways such as nucleocytoplasmic transport and cellular stress responses [22]. The cellular stress response is a critical pathway tightly linked to ALS/FTD and TDP-43 supported via genetic, experimental, and epidemiological evidence [23–36]. On the one hand, ALS/FTD-linked mutations disrupting various steps of the stress response pathways converge on the dysregulation of TDP-43 resulting in pathology [23–25, 30–33, 36]. On the other hand, exogenous insults such as aging, head injuries, viral infections, and other exposures may confer susceptibility or precipitate ALS/FTD and can serve as pre-clinical models of TDP-43 proteinopathy [8, 37–39]. Motor neurons, the primary vulnerable cell type in ALS, are thought to be particularly susceptible to stress due to the high levels of excitotoxicity experienced throughout one's lifetime [40]. Indeed, prolonged cellular stress due to chronic stress exposure or failures in stress recovery can result in TDP-43 pathology [28, 41]. However, much less is known about the molecular pathways acting upon TDP-43 in the cell stress response and how they might be linked to age-related neurodegeneration. Uncovering these mechanisms will help to better understand how environmental insults that occur throughout aging converge on TDP-43 and cause susceptibility to disease.

Post translational modifications (PTMs) play key roles in regulating protein function and have been tightly linked to TDP-43 (dys)function and disease. TDP-43 is modified by an array of PTMs including phosphorylation, ubiquitination, acetylation, and polyADP-ribosylation [42–46]. Abnormal TDP-43 phosphorylation and ubiquitination are pathognomonic of ALS and TDP-43 related FTD [42]. Recent studies have suggested that SUMOylation – the covalent conjugation of a Small Ubiquitin-like Modifier (SUMO) to target lysine residues [47, 48] – by SUMO1 may have a role in regulating TDP-43 nucleocytoplasmic transport and RNA binding [49–51]. SUMO1 is best characterized for its roles in nucleocytoplasmic shuttling [52]. SUMO2 however is the only essential SUMO paralog and selectively plays roles in orchestrating cellular stress responses [53, 54]. SUMO2 has previously been observed in TDP-43 aggregates in vitro and is related with TDP-43 insolubility [55, 56]. However, it is unclear whether TDP-43 is a direct target of SUMO2 and what the implications are on TDP-43 function and disease pathogenesis.

Here, we show that TDP-43 is modified by SUMO2 selectively in response to cellular stressors. TDP-43 becomes SUMOylated within the nucleus early in response to stress, upstream of TDP-43 aggregation. Modification by SUMO2 is further correlated with dosage and duration of cellular stress and peaks during the recovery phase before it is cleared through the ubiquitin proteosome system. We further identified four E3 SUMO ligases that can modulate the levels of TDP-43 SUMOylation. We found that TDP-43 is SUMOylated by SUMO2 in a conserved region of the C-terminal domain at lysine (K) 408 directly adjacent to phosphorylation residues serine (S) 409/410 characteristically phosphorylated in TDP-43 aggregates. To understand the physiological consequences of blocking TDP-43 SUMOylation, we generated a knock in mouse model bearing a p.K408R point mutation in endogenous mouse *Tardbp* allele. Cortical neurons cultured from these mice display impaired stress recovery and accumulation of nuclear TDP-43. These mice do not show abnormalities in development but develop mild social and cognitive deficits as they age. Pathologically, we observe TDP-43 mislocalization and accumulation of phosphorylated TDP-43 in the spinal cord and significant denervation of neuromuscular

junctions in aged mice. As SUMOylation of TDP-43 plays a protective role in mice during aging, we assessed human brain samples and observed a positive correlation between global SUMOylation and age inferring an increased demand on SUMO-related pathways during aging. Finally, we observed significant increase in TDP-43 and SUMO2 interactions in the prefrontal cortex from individuals diagnosed with ALS/FTD compared to unaffected controls suggesting SUMOylation is actively engaged in regulating TDP-43 in disease states.

Results

TDP-43 is SUMOylated in the nucleus in a context specific manner

Various acute stressors including oxidative (sodium arsenite, $NaAsO_2$), hyperosmotic (D-sorbitol and sodium chloride), and heat shock have been demonstrated to induce TDP-43 mislocalization and aggregation in vitro, helping to uncover key mechanisms affected in disease [24, 57, 58]. As sodium arsenite is a commonly used stressor to interrogate TDP-43 alterations, we examined whether TDP-43 became SUMOylated in response to sodium arsenite treatment. Using an immunoprecipitation assay ("SUMOylation Assay", Fig. 1A) to immunoprecipitate HA-SUMO bound proteins under denaturing conditions to disrupt non-covalent protein interactions, we found that TDP-43 becomes SUMOylated by SUMO2 and can form polySUMO chains specifically in response to stress (Fig. 1B). Interestingly we found that sodium arsenite and heat shock stressors, but not hyperosmotic stress, induced TDP-43 SUMOylation suggesting that SUMOylation is a context specific modifier of TDP-43 (Fig. S1A). However, it remains unclear whether TDP-43 SUMOylation functions down a pathway shared by sodium arsenite and heat shock, or whether TDP-43 SUMOylation responds to a specific stress burden not met under hyperosmotic stress despite the formation of stress granules.

Previous reports have suggested that TDP-43 is SUMOylated under native conditions by SUMO1 to regulate nucleocytoplasmic transport and RNA binding [49]. Strikingly, we found that TDP-43 SUMOylation was modified by SUMO2 and SUMO3 specifically under stressed conditions; consistent with the conserved roles of SUMO2 and SUMO3 in response to stress (Fig. S1B). Mature (covalently bound) SUMO2 and SUMO3 share nearly 100% amino acid homology making them difficult to differentiate and thus referred together as SUMO2/3. Since SUMO2 is the only essential and most abundantly expressed SUMO paralog in the CNS and sodium arsenite is commonly used to study TDP-43 pathobiology, we focused on TDP-43 SUMOylation by SUMO2 in response to sodium arsenite stress [53, 59].

To test whether TDP-43 SUMOylation is linked with disease-like states, we expressed ALS-linked mutant TDP-43 ($TDP\text{-}43^{Q331K}$) and found that TDP-43 SUMOylation was significantly increased compared to wild type TDP-43 (Fig. S1C). Next, we disrupted the nuclear localization sequence in TDP-43 ($TDP\text{-}43^{NLSmut}$) to mislocalize TDP-43 to the cytoplasm and found that in response to sodium arsenite, $TDP\text{-}43^{NLSmut}$ blocks SUMOylation indicating that nuclear localization is essential for TDP-43 SUMOylation (Fig. 1C,D). Classically, lysine (K) residues, in addition to arginine (R) residues, are critical components of a traditional NLS to enable the interaction with importins to facilitate nuclear import of proteins; but they may also be direct targets of SUMOylation [60]. To determine whether loss of TDP-43

(See figure on next page.)

Fig. 1 SUMOylation dynamically regulates nuclear TDP-43 in a stress-responsive manner. **A** Schematic of immunoprecipitation assays to detect TDP-43 SUMOylation. **B** Representative SUMOylation Assay western blot in HEK293T cells detecting TDP-43 SUMOylation specifically in response to 1 h sodium arsenite (250 µM) stress. * = SUMOylated TDP-43, ** = PolySUMOylated TDP-43. **C** Schematic of TDP-43-GFP Nuclear Localization Sequence (NLS) variants and representative florescent microscopy analysis of their subcellular localization. (Scale bar = 10 µm). Yellow amino acids represent those critical for PY-NLS function. Teal arginine residue was mutated from the native HNRNPA1. **D** Representative GFP-trap SUMOylation assay in HEK293T cells detecting loss of SUMOylation in response to TDP-43 mislocalization in response to 1 h sodium arsenite stress (250 µM). ($N = 3$) RM One-Way ANOVA with Fisher's LSD test. Data presented as mean ± SEM relative to stressed TDP-43-GFP (WT) condition, * $p < 0.05$, ** $p < 0.005$, *** $p < 0.0005$. Grey bar = Unstressed, Cyan bar = Stressed. **E** Representative image and quantification of relative proximity ligation signal between TDP-43 and SUMO2/3 in murine primary cortical neuron cultures (7 DIV) in response to 1 h sodium arsenite (250 µM) treatment. Scale bar = 20 µm. ($N = 4$ per condition) Unpaired T-test data presented as mean ± SEM, *** $p < 0.0005$ **F** Representative SUMOylation Assay in HEK293T cells of TDP-43 SUMOylation dynamics during stress (250 µM sodium arsenite) and recovery demonstrating a dependency on the ubiquitin proteosome for clearance of polySUMOylated TDP-43 by treatment with proteasome inhibitor MG132 (2 µM). ($N = 3$) RM One-Way ANOVA with Fisher's LSD test. Data presented as mean ± SEM relative to 1 h stressed condition, * $p < 0.05$, ** $p < 0.005$, *** $p < 0.0005$, **** $p < 0.0001$. Grey Bar = Unstressed, Cyan Bar = Stressed, Yellow Bar = Post stress recovery, Red Bar = MG132 inhibitor added. **G** Schematic and representative GFP-Trap SUMOylation assay in HEK293T cells screening for potential E3 ligases regulating TDP-43 SUMOylation in response to 1 h sodium arsenite stress (250 µM). ($N = 3$) RM One-Way ANOVA with Fisher's LSD test. Data presented as mean ± SEM relative to stressed control without sgRNA, *** $p < 0.0005$, **** $p < 0.0001$. Light Grey Bar = Control or insignificant change from stressed condition, Dark Grey Bar = Positive control, Cyan Bar = Significantly different than stressed condition

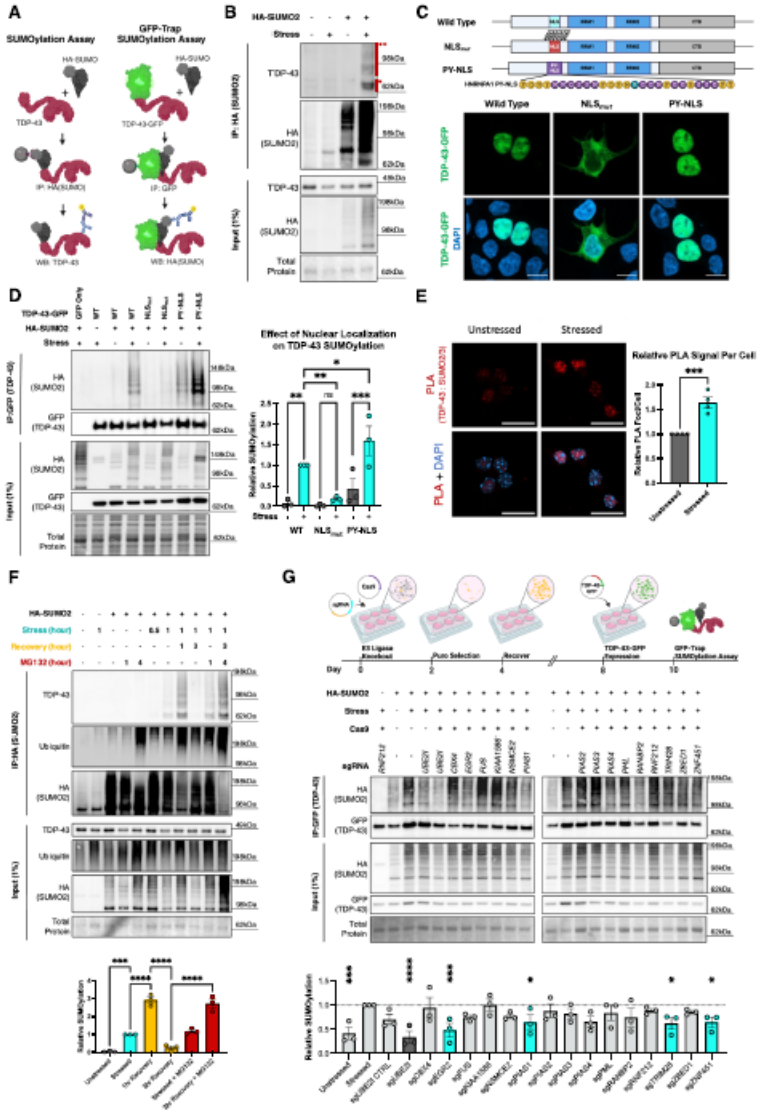

Fig. 1 (See legend on previous page.)

SUMOylation is mediated through loss of nuclear localization or disruption of lysine (K) residues in the NLS, we sought to restore TDP-43 localization to rescue TDP-43 SUMOylation. We surveyed the literature to identify a NLS that functions independent of lysine (K) residues. Previous studies have demonstrated that the RNA binding protein HNRNPA1 contains a non-conventional PY-NLS to facilitate nuclear localization [61, 62]. We expressed a chimeric TDP-43 where the native NLS was replaced with an HNRNPA1 PY-NLS (TDP-43^{PY-NLS}) and found that TDP-43^{PY-NLS} localizes to the nucleus reflecting wild type TDP-43 (Fig. 1C). By performing a GFP-Trap SUMOylation assay we found that TDP-43^{PY-NLS} rescues the loss of SUMOylation observed when expressing TDP-43^{NLSmut} indicating that nuclear localization, and not the lysine (K) residues within the NLS, is required for stress-dependent TDP-43 SUMOylation (Fig. 1D).

Finally, we aimed to validate our findings and visualize the interaction between TDP-43 and SUMO2 in primary cortical neurons. As TDP-43 and SUMO2 are widely expressed throughout the nucleus, co-localization analysis is challenging to infer SUMOylation events (Fig. S1D). To visualize the interaction between TDP-43 and SUMO2/3 we performed a proximity ligation assay (PLA) in murine primary cortical neurons cultures (Fig. 1E, Fig. S1E). We found that in response to sodium arsenite there is a significant increase in PLA signal between endogenous TDP-43 and SUMO2/3 in the nucleus. Taken together, SUMOylation may be an important mechanism regulating nuclear TDP-43 upstream of mislocalization in response to stress.

SUMOylation is an early event in response to stress and helps clear TDP-43 through the ubiquitin proteasome system during recovery

Prolonged cellular stress in vitro leads to mislocalization of TDP-43 and progressive transition into insoluble aggregates resembling aspects of pathology observed in disease [16, 28, 31, 33, 63]. As TDP-43 SUMOylation occurs within the nucleus upstream of nuclear egress, we postulated that SUMOylation would occur upstream of aggregation during prolonged sodium arsenite stress. To test this hypothesis, we performed a time course assay to characterize the dynamics of TDP-43 SUMOylation during prolonged treatment with sodium arsenite. We observed that TDP-43 becomes readily SUMOylated in the first 15–30 min of the acute stress response upstream of the accumulation of RIPA-insoluble, phosphorylated TDP-43 (Fig. S1F). Furthermore, we observed an increase in TDP-43 SUMOylation that linearly correlated with the duration of stress ($R^2 = 0.6922$, $p < 0.0001$). To determine whether SUMOylation occurs in response to relative stress intensity, we performed a dose response assay and found that TDP-43 SUMOylation is proportional to relative stress intensity (Fig. S1G). Therefore, the increase in TDP-43 SUMOylation during prolonged stress is likely due to an increased stress burden over time.

To determine the fate of SUMOylated TDP-43, we performed a stress-recovery time-course assay where cells were stressed with sodium arsenite for up to 1 h, then allowed cells to recover after washout. For the first hour during stress recovery, we observed an ~ threefold increase in TDP-43 SUMOylation indicating that TDP-43 continues to be SUMOylated and polySUMOylated during the early stages of stress recovery (Fig. 1F). Furthermore, SUMOylated TDP-43 was not detectable after 3 h of recovery, suggesting that most of the clearance occurs between 2–3 h post stress. TDP-43 is known to interact with the SUMO-Targeted Ubiquitin Ligase RNF4 which can polyUbiquitinate SUMOylated proteins to be degraded through the UPS [64]. To determine whether the UPS functions to clear SUMOylated TDP-43 during stress recovery, we treated cells with the proteasome inhibitor MG132 and monitored TDP-43 SUMOylation during stress and recovery. We observed that inhibiting the UPS system by MG132 treatment prevented clearance of SUMOylated TDP-43 during post-stress recovery indicating that SUMOylated TDP-43 is marked for degradation by the UPS pathway. Importantly, treatment with MG132 for 1 or 4 h was not sufficient to induce TDP-43 SUMOylation by itself, consistent with the stress-selective nature inducing TDP-43 SUMOylation. Taken together, TDP-43 SUMOylation occurs early in the stress response which then leads to ubiquitin-targeted clearance during stress recovery demonstrating SUMOylation may be an important mechanism regulating nuclear TDP-43 proteostasis.

Stress-dependent TDP-43 SUMOylation is mediated by select E3 SUMO ligases

E3 SUMO ligases are important mediators for SUMOylation of select substrates and enable spatiotemporal regulation of this modification. Thus, they may represent critical modulators of TDP-43 SUMOylation. To identify potential E3 SUMO ligases that may regulate TDP-43 SUMOylation, we first performed a literature search to identify potential ligases with evidence of mediating SUMOylation. We prioritized 15 candidate E3 SUMO ligases and using a dual sgRNA/Cas9 approach generated knockout cell lines for each of the candidate ligases and performed GFP-Trap SUMOylation assays to test the effects on TDP-43 SUMOylation (Fig. 1G) [65–79]. As a positive control, we knocked out the sole E2 SUMO ligase, UBC9 (encoded by *UBE2I*), which led to a near complete loss of TDP-43 SUMOylation demonstrating

the functionality of the approach. We identified four SUMO E3 ligases whose knockout consistently reduced the levels of stress-induced TDP-43 SUMOylation: *EGR2 (KROX20), PIAS1, TRIM28 (KAP1),* and *ZNF451 (ZATT).* EGR2 is linked to the neuromuscular disorder Charcot Marie Tooth Disease and is an immediate early gene rapidly reacting to external cellular stimuli aligning with the early response of TDP-43 SUMOylation upon stress [66, 80]. PIAS1 is a canonical, highly conserved E3 SUMO ligase known to play roles in cellular stress responses [81]. TRIM28 is also a well characterized E3 SUMO ligase which is a predicted interactor of SUMOylated TDP-43 based on the GPS-SUMO2.0 algorithm [77, 82, 83]. ZNF451 is characterized as a stress dependent E3 SUMO ligase specifically promoting poly-SUMOylation with SUMO2/3. It is sometimes referred to as an "E4 SUMO elongase" which complements our data that TDP-43 is polySUMOylated in response to stress [68, 79]. Identification of these putative TDP-43 SUMO ligases supports the robustness of stress-induced TDP-43 SUMOylation and adds layers of nuance into the regulation of TDP-43 with variable routes of modulating TDP-43 functions.

TDP-43 SUMOylation occurs in a conserved region of the C-terminal domain

SUMOylation occurs at lysine (K) residues often residing within a consensus SUMOylation motif, Ψ-K-x-D/E (Ψ = large hydrophobic residue, x = any amino acid), however it is increasingly recognized that SUMOylation at lysine residues in non-consensus motifs is not uncommon and plays significant roles in regulating protein function [82]. Using GPS-SUMO (https://sumo.biocuckoo.cn/) to predict likely SUMOylation sites on TDP-43, we identified a consensus SUMOylation motif within the first RNA recognition motif at K136 – thought to be the site targeted by SUMO1 – and a non-consensus SUMOylation motif within the C-terminal domain at K408 [82, 83].

To map the residue of stress induced TDP-43 SUMOylation, we expressed TDP-43 mutating the candidate lysine (K) residues to arginine (R) residues to maintain similar charge and structure of the native amino acid sequence while blocking SUMOylation: K136R, K408R, and K136R/K408R "2KR". By performing a GFP-trap SUMOylation assay, we observed that TDP-43^{K136R} did not block sodium arsenite-induced TDP-43 SUMOylation (Fig. 2A). Through fluorescent microscopy, we observed that TDP-43^{K136R} formed nuclear puncta with resemblance to RNA-binding deficient TDP-43 (5FL) (Fig. S2A). We predicted the structure of TDP-43 and TDP-43^{K136R} with AlphaFold3 in the presence of UG repeated RNA and found that K136R is predicted to slightly alter the tertiary structure of TDP-43 and affect the interaction with RNA (Fig. S2B and S2C). Thus, phenotypes observed in TDP-43^{K136R}, as reported by others, may be facilitated by loss of RNA binding functions independent of loss of SUMOylation [49–51]. In contrast, through GFP-trap SUMOylation assays we found that TDP-43^{K408R} mutant significantly reduced TDP-43 SUMOylation by ~ 50%, suggesting K408 is a major site of SUMOylation in response to sodium arsenite stress (Fig. 2A). Importantly, mining two independent unbiased mass spectrometry studies identifying sites of SUMOylation across the proteome in stressed and unstressed conditions also uncovered TDP-43 SUMOylation at K408, supporting our findings [84, 85]. Through florescent microscopy analysis, we found that expression of TDP-43^{K408R} did not induce nuclear TDP-43 puncta but instead led to a slight, albeit insignificant, increase in cells presenting with mislocalized TDP-43 (Fig. S3D). However, overexpression of TDP-43^{K408R} did not uniformly induce mislocalization in all cells, consistent with the dynamic nature of TDP-43 SUMOylation and the requirement of stress to introduce TDP-43 SUMOylation responses. Finally, TDP-43^{2KR} significantly reduced TDP-43 SUMOylation to the same extent as TDP43^{K408R} suggesting that K408 and not K136 is a target of stress-induced SUMOylation (Fig. 2A). We further observed that TDP-43^{2KR} expression is less stable than TDP-43^{K408R} likely due to the structural changes mediated by K136R. Taken together, K408 is a major target of stress-induced SUMOylation.

To address the evolutionary conservation of TDP-43 SUMOylation at K408, we aligned the amino acid sequences of TDP-43 with 300 orthologs from OrthoDB and found that human K408 is nearly completely conserved throughout jawed-vertebrates concurrent with the evolution of the C-terminal domain (Fig. 2B, Table S1). While this domain harbors the majority of ALS/FTD causing mutations, the residues surrounding K408 display considerably high levels of conservation (~ 86% pairwise identity) indicating that this motif may play important roles in regulating TDP-43 in vertebrates that may be altered by disease causing mutations (Fig. 2C, Table S1). Consistent with these findings, no missense variants have been identified that disrupt the SUMOylation motif (based on gnomAD v4.0 [86]) supporting its robust conservation in the healthy human population.

The residues surrounding TDP-43 K408, specifically S403, S404, S409, and S410 are characteristically phosphorylated in patients with TDP-43 proteinopathy [42]. To determine whether phosphorylation of TDP-43 at these serine residues interact with SUMOylation at K408, we expressed phospho-dead "4SA" TDP-43 (S403/404/409/410A) and observed that TDP-43^{4SA} does

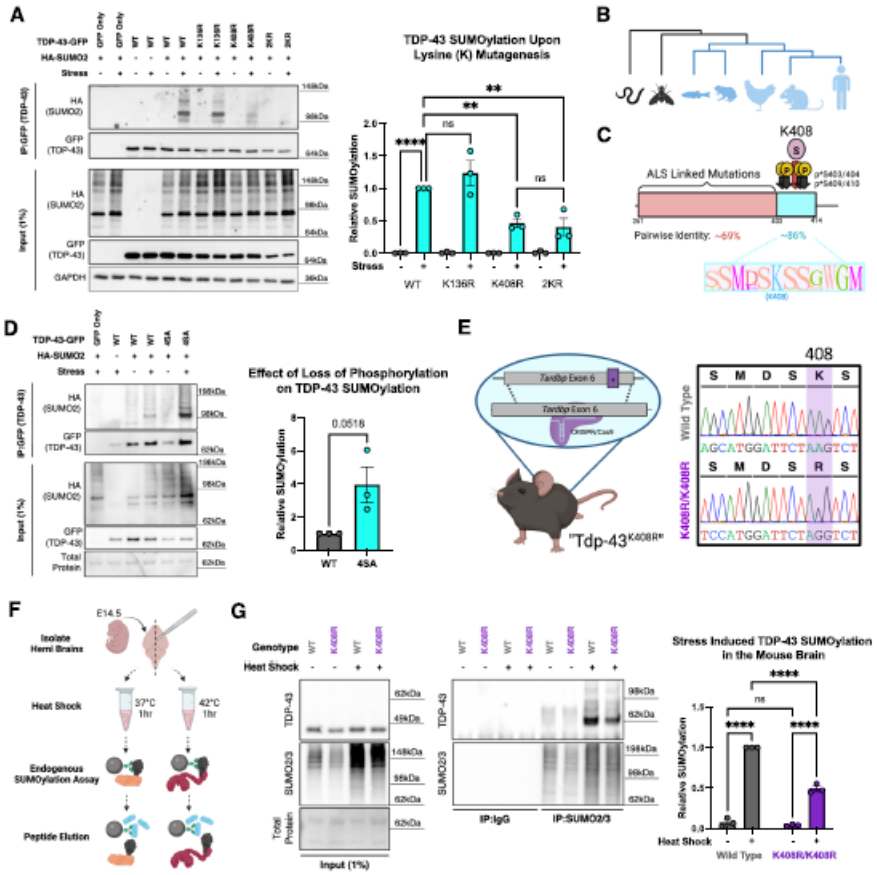

Fig. 2 TDP-43 is SUMOylated at K408 in a conserved region of the C-terminal domain. **A** Representative GFP-Trap SUMOylation assay in HEK293T cells to map the site of TDP-43 SUMOylation in response to 1 h sodium arsenite (250 µM) stress. One-Way ANOVA with Fisher's LSD test. Data presented as mean ± SEM relative to stressed TDP-43-GFP (WT) condition, ** $p < 0.005$, **** $p < 0.0001$. Grey Bar = Unstressed, Cyan Bar = Stressed. **B** Phylogenetic representation from alignment of representative TDP-43 paralogs highlighting the emergence and conservation of [human] K408 (Blue). **C** Pairwise identity of the [human] TDP-43 C-terminal domain from MUSCLE alignment of 300 amino acid sequences for TDP-43 paralogs from Humans to Actinopterygii from OrthoDB. Red represents the TDP-43 C-terminal domain (Intrinsically disordered domain). Cyan represents PTM- enriched region at the extreme C-terminus. **D** Representative GFP-Trap SUMOylation assay in HEK293T cells with phospho-dead TDP-43 "4SA" (S403/404/409/410A) highlighting antagonism between SUMOylation and phosphorylation. ($N = 3$) Unpaired T-test data presented as mean ± SEM. **E** Schematic and sanger sequencing of the TDP-43^{K408R} knock in mouse line. **F** Schematic of endogenous SUMOylation assay from embryonic mouse brains. **G** Validation of loss of stress-induced TDP-43 SUMOylation in the brains of embryonic TDP-43^{K408R} mice ex vivo. All mice presented are either wild type (WT) or homozygous for K408R (K408R/K408R). 2-Way ANOVA with Fisher's LSD test. Data presented as mean ± SEM relative to stressed WT condition, **** $p < 0.0001$

not lead to loss of SUMOylation following stress but rather appeared to promote an increase in its SUMOylation (Fig. 2D). Whether phosphorylation functions allosterically to remove SUMO2/3 at K408 or antagonistically to block the SUMOylation recognition site remains unclear. The independent modification by either phosphorylation or SUMOylation may serve as a mechanism to differentially regulate TDP-43 function independently or sequentially in response to stimuli. Thus, while TDP-43 phosphorylation has gained significant attention since its initial discovery [42] – in part due to the availability of phospho-specific antibodies – we now show that the C-terminal domain contains a conserved "PTM-enriched region" where SUMOylation at K408 may precede phosphorylation, revealing additional complexity and nuance to the stimulus-induced regulation of TDP-43.

C-terminal SUMO-mimetic destabilizes TDP-43

Promoting specific protein SUMOylation is rather difficult given the size of the SUMO molecule and the pleiotropy resulting from overexpressing SUMO proteins and their related machinery. To overcome this limitation and to mimic SUMOylation at K408, we expressed TDP-43-HA and TDP-43 with a C-terminal SUMO2 fusion (TDP-SUMO2-HA) in HEK293T cells. By western blot we found that C-terminal fusion of SUMO2 led to a significant reduction in TDP-43 levels (Fig. S3A). The reduction in TDP-43-SUMO2-HA suggesting that C-terminal fusion of SUMO2 destabilizes TDP-43 levels is consistent with our data showing that prolonged TDP-43 SUMOylation leads to its polyubiquitination and degradation (Fig. 1F). We further observed that overexpression of TDP-43-HA and TDP-43-SUMO2-HA both significantly increased phosphorylation of eIF2α compared to non-transfected controls despite significantly lower levels of TDP-43-SUMO2-HA.

Next, we aimed to gain insight into how C-terminal fusion of SUMO effects TDP-43 localization and stress response. We did not observe constitutive changes in TDP-43 localization suggesting that SUMO2 fusion does not drive TDP-43 nuclear export (Fig. S3B). By stressing cells for 1 h with sodium arsenite we observed that TDP-43-SUMO-HA cells could elicit a stress response and form stress granules similar to the TDP-43-HA counterpart (Fig. S3B). However, we found that stress granules were significantly larger in cells expressing TDP-43-SUMO2-HA compared to TDP-43-SUMO2-HA (Fig. S3B). In addition, we were surprised to find a significant increase in the proportion of stress granules colocalizing with TDP-43-SUMO2-HA compared to TDP-43-HA alone. Taken together this suggests that SUMOylation of TDP-43 at the C-terminus converges on stress response pathways involving stress granules and the integrated stress response (i.e. eIF2α pathway). However, whether TDP-43 SUMOylation is involved in the upstream regulation or downstream modulation of these pathways remains unclear.

Endogenous mutation of murine TDP-43 at K408 blocks stress-responsive TDP-43 SUMOylation in the mouse brain

To understand the cellular and physiological roles of TDP-43 SUMOylation at K408, we generated a knock in mouse model harboring a missense (c.1223 A>G) point mutation in the endogenous mouse *Tardbp* locus resulting in the expression of Tdp-43 bearing a p.K408R missense mutation (Fig. 2E, Fig. S4A,B). For simplicity herein, all genes/proteins will be referred to following their human nomenclature (e.g. mouse Tdp-43 versus human TDP-43, collectively "TDP-43"). Although TDP-43 and SUMO2 are independently essential for embryonic development, the "TDP-43^{K408R}" mice are born at normal mendelian ratios without gross impairment indicating that TDP-43 SUMOylation at K408 is not essential for murine development (Fig. S4C) [53, 87].

In order to validate that mutation of endogenous TDP-43 K408 blocks stress responsive TDP-43 SUMOylation in TDP-43^{K408R} mice, we designed an ex vivo approach to test endogenous stress responsive TDP-43 SUMOylation in the mouse brain (Fig. 2F). Briefly, we dissected mouse embryos at E14.5 and divided each brain into two hemispheres. Both hemispheres were maintained in neurobasal complete media for one hour, with one hemisphere at 37 °C as a control, and the complementary hemisphere was heat shocked at 42 °C. The brain hemispheres were lysed under denaturing conditions and endogenously SUMOylated proteins were immunoprecipitated using antibodies targeted against endogenous SUMO2/3. SUMOylated proteins were eluted using a synthetic peptide reflecting the antibody epitope to competitively elute SUMOylated proteins. We observed that this approach reliably detects endogenous TDP-43 SUMOylation in response to heat shock yielding a doublet band at ~65 kDa and a corresponding decrease by ~50% in TDP-43^{K408R} animals reflecting previous results in HEK293T cells (Figs. 1B, 2G). Thus, stress-induced TDP-43 SUMOylation is impaired in the TDP-43^{K408R} mouse brain.

TDP-43 SUMOylation at K408 supports cellular stress response and recovery in neurons

As TDP-43 SUMOylation responds to, and is cleared during cellular stress and recovery respectively, we posited that SUMOylated TDP-43 plays key roles in responding and recovering from stress. We cultured murine TDP-$43^{+/+}$ and TDP-$43^{K408R/K408R}$ primary cortical neurons and performed stress and recovery assays to determine

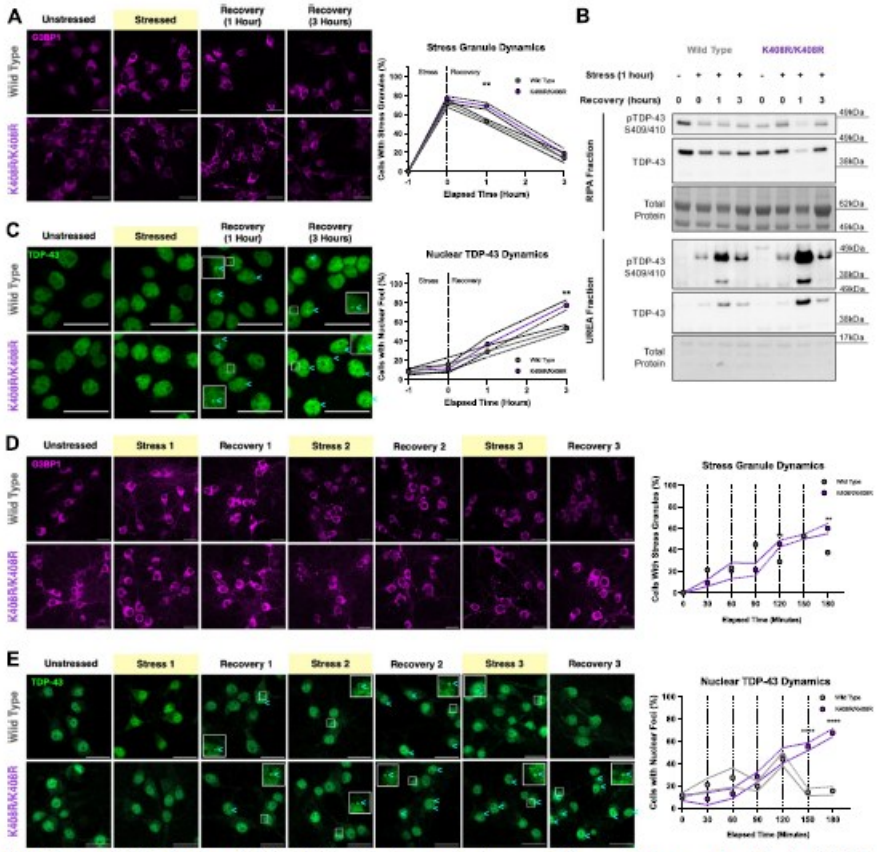

Fig. 3 Blocking TDP-43 SUMOylation at K408 impairs the cellular stress response in neurons. **A** Representative images and quantification of G3BP1 stress granule dynamics in mouse primary cortical neurons (7 DIV) during stress (1 h 250 µM sodium arsenite) and recovery. G3BP1 contrast was set for optimal visualization of stress granules. Scale bar = 25 µm ($N = 5$), 2-Way ANOVA with Fisher's LSD test data presented as mean ± SEM, * $p < 0.05$, ** $p < 0.005$. **B** Representative western blot and quantification of RIPA and UREA fractions from mouse primary cortical neurons (7 DIV) during stress (1 h 250 µM sodium arsenite) and recovery. Quantification found in Fig. S6A. **C** Representative images and quantification of TDP-43 nuclear foci formation in mouse primary cortical neurons (7 DIV) during stress (1 h 250 µM sodium arsenite) and recovery. Cyan arrowheads denote cells with nuclear TDP-43 foci. Scale bar = 25 µm. ($N = 5$), 2-Way ANOVA with Fisher's LSD test data presented as mean ± SEM, ** $p < 0.005$. **D** Representative images and quantification of G3BP1 stress granule dynamics in mouse primary cortical neurons (7 DIV) during repeated stress (30-min 250 µM sodium arsenite treatment) and recovery (30-min washout), repeated 3 times. Scale bar = 25 µm. ($N = 3$), 2-Way ANOVA with Fisher's LSD test data presented as mean ± SEM, * $p < 0.05$, ** $p < 0.005$. **E** Representative images and quantification of TDP-43 nuclear foci formation in mouse primary cortical neurons (7 DIV) during repeated stress (30-min 250 µM sodium arsenite treatment) and recovery (30-min washout), repeated 3 times. Cyan arrowheads denote cells with nuclear TDP-43 foci. Scale bar = 25 µm. ($N = 3$), 2-Way ANOVA with Fisher's LSD test data presented as mean ± SEM, **** $p < 0.0001$. For all immunofluorescent assays at least 50 cells were imaged and quantified per replicate ($N = 3–5$). All assays present wild type mice in grey and K408R/K408R mice in purple

to body weight or motor abilities indicating that blocking TDP-43 SUMOylation does not lead to gross developmental abnormalities (Fig. S7A-C).To determine whether blocking TDP-43 SUMOylation leads to phenotypes in an age-dependent manner, we assessed general wellness biweekly, including measuring body weight and hindlimb clasping scores, and performed a battery of 14 behavioral tests focusing on motor, social, and cognitive function related to ALS and FTD at three time points (2, 9 and 16 months, Fig. S7D-F, S8-10). Of note: TDP-43$^{K408R/+}$ mice are generally omitted from figures for clarity to avoid confounding variables that may arise due to asymmetric regulation of wild type and K408R alleles due to the autoregulatory nature of TDP-43 (i.e. potential dominant negative effects conferred by the mutation and not partial loss of SUMOylation), but are accessible in Table S2 and typically exhibit a milder phenotype than TDP-43$^{K408R/K408R}$.

We were surprised to observe that blocking TDP-43 SUMOylation in TDP-43^{K408R} mice resulted in sex-specific cognitive and social deficits selective to female animals. Starting around 2 months of age, we observed significant barbering in female mice leading to alopecia in the K408R mutants (Fig. 4A). Consistent with this finding, we found that aged female TDP-43$^{K408R/K408R}$ mice were significantly more submissive to their TDP-43$^{+/+}$ counterparts in the tube test (Fig. 4B). Thus, blocking TDP-43 SUMOylation leads to social abnormalities in female mice. In assessing the cognitive behaviors, we observed significant risk taking and hyperactivity in the open field test at 2 months of age (Fig. 4C). This hyperactivity was age-dependent and selectively affected young female mice as they were significantly less active than their TDP-43$^{+/+}$ counterparts at 9 months of age in the open field tests (Fig. 4C). Additionally, these female TDP-43$^{K408R/K408R}$ mice presented with significant impairment during habituation at 9 months in the beam break test (Fig. 4D). As there was no change in motor abilities in the rotarod and digigait tests (Fig. S9C,D), we rationalized that the activity abnormalities were likely due to cognitive and anxiety impairments as opposed to motor impairments. By 16 months of age, female TDP-43$^{K408R/K408R}$ mice performed significantly worse than TDP-43$^{+/+}$ mice in the spontaneous Y-maze, inferring age-dependent cognitive decline in the domain of working memory (Fig. 4E). Together, female mice present with social and cognitive impairment in early age with slight impairments in cognitive performance with aging. There were

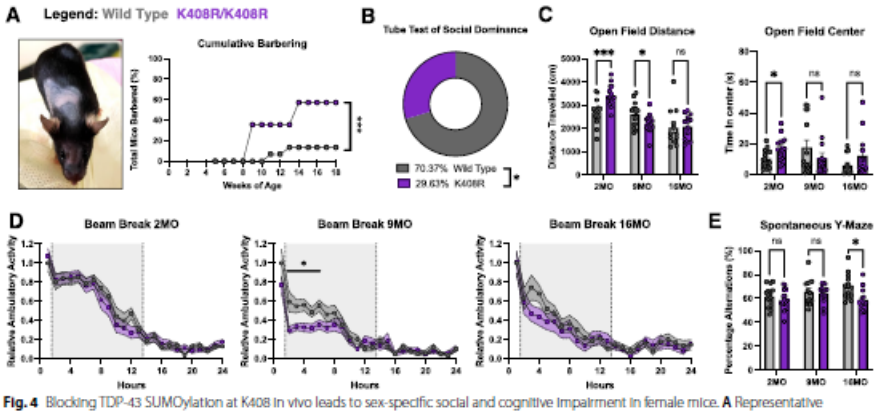

Fig. 4 Blocking TDP-43 SUMOylation at K408 in vivo leads to sex-specific social and cognitive impairment in female mice. **A** Representative image of a barbered female mouse and quantification of cumulative barbering probability. 2-Way ANOVA with Tukey's Multiple Comparisons, *** $p < 0.0005$. **B** Tube test of social dominance at 16 months of age (16MO) displaying the total head-to-head battles and win percentage by genotype comparing wild type against K408R (K408R/+ and K408R/K408R animals). Binomial Test of Observed vs. Expected with Expected due to random chance set to 50%, * $p < 0.05$. **C** Quantification of total distance traveled (cm) and total time in center (s) in the open field test of female mice. Mixed Effects Analysis with Tukey's multiple comparison data presented as mean ± SEM, *** $p < 0.0005$, * $p < 0.05$. **D** Quantification of percent alternations in the spontaneous Y-maze test of female mice at 2, 9, and 16 months of age (2MO, 9MO, 16MO, respectively). Mixed-Effects Analysis with Tukey's multiple comparison data presented as mean ± SEM, * $p < 0.05$. **E** Quantification of relative ambulatory activity normalized to wild type at 1 h of female mice at 2, 9, and 16 months of age (2MO, 9MO, and 16MO, respectively). Grey shading between hours 2 and 14 indicate "lights off" with respect to day/night light cycle. 2-Way ANOVA with Tukey's multiple comparison data presented as mean ± SEM, * $p < 0.05$. All assays present wild type mice in grey and K408R/K408R mice in purple

no significant cognitive effects in male TDP-43$^{K408R/K408R}$ mice, however mild impairments were observed on the rotarod test at 9 months of age (2-way ANOVA $p=0.0273$, Table S2). This deficiency was not observed at 16 months of age, largely due to all mice performing significantly worse at the rotarod task, limiting the interpretation of this assay [93]. Taken together, the age-dependent cognitive and social impairment observed in female TDP-43 SUMO-deficient mutants highlight interesting and unexplored aspects of TDP-43 with important implications for understanding sex-specific roles of TDP-43 SUMOylation.

TDP-43^{K408R} mice present with distinct features of TDP-43 pathology related to ALS and FTD

Next, we aimed to characterize regions of the nervous system vulnerable in ALS/FTD to determine how loss of TDP-43 SUMOylation impacts these regions across aging. We did not observe significant differences in cortical thickness of the primary motor cortex nor prefrontal cortex in male or female mice across all timepoints suggesting that loss of TDP-43 SUMOylation does not lead to widespread cortical degeneration occurring during normal aging (Fig. S11A,B). To gain an additional layer of granularity into vulnerable neuron subpopulations in the cortex, we stained for CTIP2 to highlight neurons in layer V, including upper motor neurons, in the cortex and did not observe significant differences in neuron quantity across aging (Fig. S11C,D). We further stained for CUX1 as a marker of layer II/III neurons which can be vulnerable to TDP-43 pathology in FTD and degeneration in Alzheimer's disease. Again, we did not observe significant changes in male nor female mice across the mouse lifespan supporting the absence of cortical degeneration in TDP-43^{K408R} animals during native aging (Fig. S11C,D). To determine if blocking TDP-43 SUMOylation results in neuroinflammation, we probed for the reactive astrocyte marker GFAP and reactive microglia marker Iba1 and observed no change in neuroinflammation (Fig. S11E-H). Together these data suggest the process of aging does not lead to cortical neurodegeneration nor cortical neuroinflammation.

Cellular and molecular changes are generally thought to precede behavioral changes in mouse models and human disease. Our biochemical and cellular assays show that stress-induced SUMOylation helps to clear TDP-43 during recovery and blocking TDP-43 SUMOylation in neurons leads to impaired recovery from stress and TDP-43 accumulation (Figs. 1E, 3, Fig. S6A,F). Due to the sex-specific social and cognitive impairment in female mice, we posited that TDP-43 accumulation would reflect the behavioural changes. Consistent with the sex-specific social and cognitive impairment described above, we find that insoluble phosphorylated TDP-43 accumulated in the cortex of female, but not male mice (Fig. S12A,B). Furthermore, this accumulation was observed as early as 2 months of age and was maintained throughout aging, which may imply that impaired TDP-43 proteostasis is underlying the social and cognitive phenotypes observed in female TDP-43^{K408R} animals. Interestingly, we observed significant changes in *MAPT* splicing in the cortex of TDP-43^{K408R} mice, specifically the N2/N0 splice isoform (Fig. S12C). Together, this may suggest that there is some degree of TDP-43 loss of function in the TDP-43^{K408R} mice.

We questioned whether motor neurons in the spinal cord present with early-stage pathology as they are subject to excess excitotoxic stress throughout their lifespan [40]. Surprisingly, we observed cytoplasmic mislocalization, but not nuclear depletion, of TDP-43 accompanied by insoluble, phosphorylated TDP-43 accumulation in the lumbar spinal cord of both male and female mice at 9 months of age (Fig. 5A, Fig. S12D,E). Furthermore, by 16 months of age, male TDP-43$^{K408R/K408R}$ displayed a significant denervation of neuromuscular junctions in the tibialis anterior and a reduction in ChAT positive neurons in the spinal cord compared to littermate controls (Fig. 5B,C, Fig. S12F-H). Together, blocking TDP-43 SUMOylation results in altered proteostasis of spinal motor neurons leading to neuromuscular junction denervation and ChAT positive motor neuron loss in an age dependent manner.

As the TDP-43^{K408R} mice continued to age beyond our behaviour timepoints we observed a 24.49% decrease in survival specific to male TDP-43$^{K408R/K408R}$ mice with a median survival of 521 days for the TDP-43$^{K408R/K408R}$ compared to 690 days for TDP-43$^{+/+}$ mice (Fig. 5D, Fig. S7D). Mice were typically found dead or euthanized after reaching a humane endpoint. Surprisingly, a few animals presented with classic hindlimb weakness and paralysis akin to those observed in other models of ALS (Supplemental Video 1). However, these results should be interpreted with caution due to the low statistical power. Taken together, our data supports that TDP-43 SUMOylation plays a protective role in mediating TDP-43 proteostasis in the CNS and that its blockade may confer a risk for ALS/FTD-like pathogenesis in an age-dependent, and sex-specific manner providing insights into molecular substrates underlying sexually dimorphic clinical features of ALS and FTD.

Aberrant SUMOylation is a feature of human aging and disease

Although SUMOylation is well understood to play an essential role in the CNS, its involvement in human aging and neurodegenerative diseases remains largely elusive.

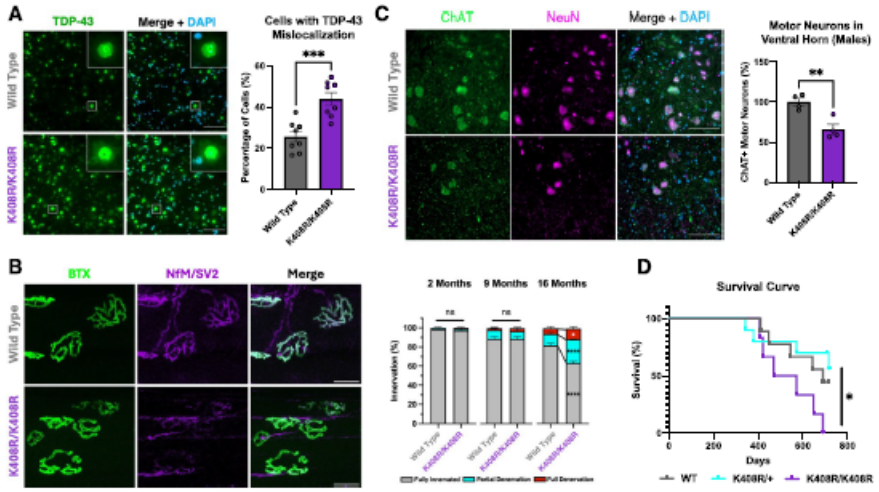

Fig. 5 Male TDP-43^{K408R} mice present with age-specific features of ALS. **A** Representative images and quantification of TDP-43 mislocalization in the lumbar spinal cord of 9-month-old TDP-43^{K408R} male and female mice. Each datapoint represents the average of 4 serial sections, 40 µm apart per individual mouse. Scale bar = 100 µm. ($N = 4$ per sex/genotype) Unpaired t-test, *** $p < 0.0005$. See Fig. S12C for sex comparisons. **B** Representative images at 16 months of age (16MO) and quantification (2MO, 9MO, and 16MO) of neuromuscular junction (NMJ) innervation in the tibialis anterior of male TDP-43^{K408R} mice. > 80 NMJs were quantified per animal. Data presented as mean ± SEM. ($N = 3$–4 per genotype) 2-Way ANOVA with Tukey's multiple comparison analysis, *$p < 0.05$, ****$p < 0.0001$. **C** Representative images and quantification of ChAT + motor neurons in the ventral horn of the lumbar spinal cord of male mice. Each datapoint is the average of 4 serial sections spaced 40 µm apart through the lumbar enlargement of the lumbar spinal cord. Unpaired t-test, ** $p < 0.005$. **D** Survival curve for male TDP-43^{K408R} mice (Females found in Fig. S7D). Curve comparisons analyzed using Log-Rank test and Gehan-Breslow-Wilcoxon test. *$p < 0.05$. All assays present Wild Type mice in grey and K408R/K408R mice in purple

To assess how SUMOylation is normally affected in human aging, we processed samples from human temporal lobe tissue ranging between 0.5 and 88 years of age from individuals unaffected by neurological diseases (Fig. 6A, Table S3, $n = 55$). Complementing our findings that SUMOylation serves as a response to increased proteostatic demands, such as those in our aging TDP-43^{K408R} model, we observed that global SUMOylation was significantly increased in "aged" (>60 years old) human brains (Fig. 6B).

To explore the extent of TDP-43 SUMOylation in human ALS/FTD cases, we performed proximity ligation assays against TDP-43 and SUMO2/3 in prefrontal cortex samples from ALS/FTD cases positive for TDP-43 pathology and age/sex matched unaffected controls (Table S3). Through semiquantitative analysis, patient samples collected from various sites were assessed for relative TDP-43 pathology by a neuropathologist in a blinded manner. We confirmed there was a significant increase in TDP-43 pathology in the prefrontal cortex of ALS/FTD patients relative to controls (Fig. S13A). When assessing the interaction between TDP-43 and SUMO2/3, we observed a significant increase in interactions in the prefrontal cortex of ALS/FTD patients with TDP-43 pathology suggesting the TDP-43 SUMOylation pathway is engaged in disease (Fig. 6C, Fig. S13B). This may be a result of increased stress burden throughout the prefrontal cortex in those affected by ALS/FTD with TDP-43 pathology compared to age and sex matched counterparts. Taken together, SUMOylation as a stress responsive modification is positively correlated with aging in the human brain, potentially linked to the increase demand imposed by age-associated stress. Additionally, the SUMOylation response is enhanced in the frontal cortex of those affected by ALS/FTD providing further in vivo support for its role in disease.

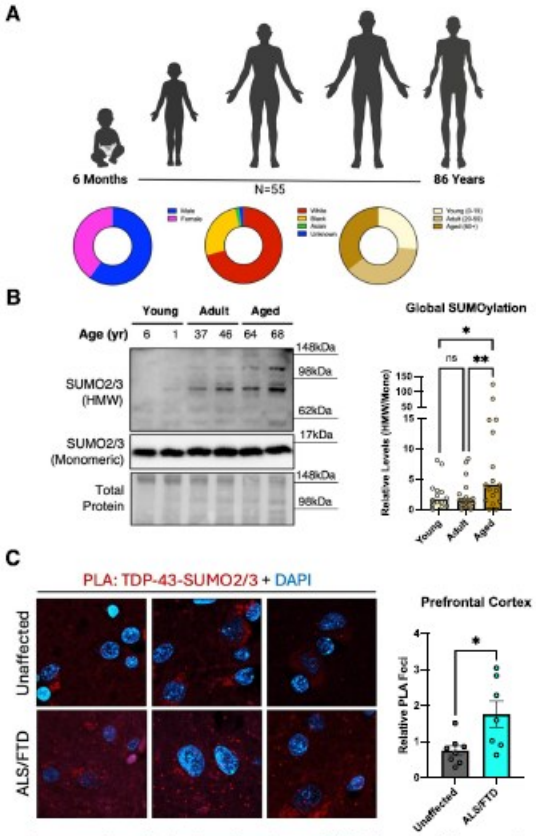

Fig. 6 SUMOylation correlates with aging and is enriched in the prefrontal cortex of ALS/FTD patients. **A** Demographic composition of temporal lobe samples from aging cohort. **B** Representative western blot and box plot of SUMO2/3 across binned age groups. Average Age: "Young" = 6.32 yrs, $N = 14$; "Adult" = 31.11 yrs, $N = 20$; "Aged" = 64.00 yrs, $N = 19$. Kruskall-Wallis with Uncorrected Dunn's multiple comparisons test. * $p < 0.05$, ** $p < 0.005$. **C** Representative images and quantification from proximity ligation assay (PLA) between SUMO2/3 and TDP-43 in the prefrontal cortex from 3 patients diagnosed with ALS/FTD and unaffected controls. ($N = 7–8$) Unpaired T-test. Data presented as mean PLA foci/per field of view ± SEM relative to average of unaffected controls, * $p < 0.05$

Discussion

Although ALS and FTD are highly heterogenous diseases, the nearly universal convergence on TDP-43 proteinopathy emphasizes a need to understand early drivers of this pathogenic process. Mutations in various genes can lead to TDP-43 pathology, however the majority of ALS and FTD cases occur sporadically without a clear genetic cause [3, 22]. Additionally, patients living with disease causing mutations do not present with symptoms of disease until later in life suggesting exogenous factors related to aging play a role in phenoconversion [94]. Cellular stressors are well characterized to induce TDP-43 pathology providing a clue as to how exogenous factors may contribute to disease pathogenesis. Given the postmitotic nature of neurons, maintaining proteostasis in response to lifelong stressors is critical for neuronal

longevity [1]. This is particularly true for motor neurons which endure constant excitotoxic stress [40]. In this study, we found that SUMOylation maintains TDP-43 proteostasis in the nucleus specifically in response to stress. This modification is critical to preserve neuronal function, the absence of which results in neuronal demise and TDP-43 proteinopathy.

Here, we find that SUMOylation of TDP-43 occurs at K408 by SUMO2/3 in response to stress. This is in contrast to what was previously reported for TDP-43 and SUMO1; where it was suggested that SUMO1 modified TDP-43 at lysine 136 [49, 50]. Indeed, mutating K136 to an arginine (R) had no effect on stress-induced TDP-43 SUMOylation by SUMO2/3, though this does not discount the possibility that SUMO1 may modify TDP-43 under conditions where increased SUMO machinery (e.g. UBC9 overexpression) is present. In our hands, expression of TDP-43^{K136R} led to the formation of nuclear TDP-43 puncta as previously reported [49, 50]. However, these puncta were similar to those observed when expressing RNA binding deficient TDP-43. Furthermore, prediction of TDP-43 structure suggests that K136R mutation may impact the structure of the RNA recognition motif and RNA binding. Thus, phenotypes observed in TDP-43 carrying the K136R mutation should be interpreted with caution.

In genetic forms of ALS or FTD caused by mutations in TDP-43, the C-terminal domain harbors the overwhelming majority of disease-causing mutations [95]. Thus, understanding the involvement of the C-terminal domain in TDP-43 biology is critical to uncover pathways that may be linked to disease independent of TDP-43 mutations. Phosphorylation of TDP-43 in the C-terminal domain, particularly S403/404 and S409/410, have garnered much attention in this regard as these residues are characteristically phosphorylated in disease [42]. However, the roles for phosphorylation at these sites remains generally elusive. Few reports have suggested roles in regulating liquid–liquid phase separation and solubility [96, 97]. Our findings suggest that phosphorylation and SUMOylation act antagonistically on TDP-43, indicating potential distinct mechanisms of regulation. We further observed that this region of the C-terminal domain targeted by SUMOylation and phosphorylation is highly conserved throughout vertebrate species. Thus, this PTM-enriched region may play key roles for regulating TDP-43 in vertebrate biology.

Regulation of TDP-43 proteostasis is critical for cells as fluctuations in TDP-43 levels can lead to toxicity in cell and animal models [20, 98–101]. Unsurprisingly, TDP-43 is regulated in a variety of mechanisms including transcriptionally, post-transcriptionally, translationally and post-translationally [11, 20, 102]. Furthermore TDP-43 can be cleared through several pathways including the proteasome, endo-lysosome, autophagy, and extracellular vesicle pathways [103–110]. Here we add another mechanism of regulation through SUMOylation during stress and recovery. We hypothesized that blocking TDP-43 SUMOylation with K408R mutation would result in its accumulation during stress recovery. Interestingly, we observed a significant increase in insoluble phosphorylated TDP-43 in TDP-43$^{K408R/K408R}$ cortical neurons and a delay in stress granule disassembly during stress recovery indicating TDP-43 accumulation. However, this was resolved 3 h post-stress indicating that the neurons could compensate to clear the aberrantly accumulated TDP-43 within this acute stress paradigm. We questioned whether chronic stress may exacerbate phenotypes and found that chronic stress significantly resulted in increased phosphorylated, insoluble TDP-35 fragments which then recovered upon removal of stress. Thus phosphorylation of TDP-43, in addition to cleavage, may be additional mechanisms to regulate TDP-43 proteostasis in the event of SUMOylation-pathway failure. Thus, SUMOylation may be an early line of defense to regulate TDP-43 in response to stress and blocking TDP-43 SUMOylation shifts proteostasis leading to delayed recovery. Future studies exploring repeated and/or divergent stressors will be crucial in determining the degree to which TDP-43 SUMOylation safeguards from cellular demise.

Previous reports have emphasized the status of altered proteostasis as a hallmark of aging in the CNS, culminating in impaired removal of damaged proteins with age [1]. In TDP-43$^{K408R/K408R}$ mice, TDP-43 was found to accumulate in the CNS in an age-dependent manner, suggesting SUMOylation plays important roles during aging. Supporting these findings, in human temporal lobe samples we similarly observed a positive correlation between global SUMOylation and age supporting SUMOylation as a potential protective mechanism during aging in the CNS. Previous studies on global SUMOylation have focused on the dynamic nature of this modification playing roles during development, and associations between SUMOylation and neurodegeneration gaining traction however roles for SUMOylation in the central nervous system during the process of human aging remain understudied [111, 112]. This may be ascribed, in part, to challenges in studying SUMOylation due to the dynamic nature of the modification and lack of specific tools to study its interactions. We employed a PLA approach to assess the interaction between TDP-43 and SUMO in ALS/FTD patients and found significantly increased interactions in the prefrontal cortex relative to age/sex matched unaffected controls. It was interesting to observe that PLA signal occurred and was increased in

both the nucleus and the cytoplasm in ALS/FTD patient samples. We hypothesize that SUMOylation of TDP-43 is an early event regulating TDP-43 proteostasis, however if overwhelmed other systems such as phosphorylation or protein cleavage may help respond to regulate TDP-43. As we are observing late-stage events, SUMOylation in the cytoplasm may be co-occurrent with late-stage regulation of TDP-43. Approaches that provide increased resolution for detecting TDP-43 SUMOylation events are clearly warranted. Recent studies have used RNA aptamers to reveal nuclear changes in TDP-43 in spinal and cortical neurons of ALS patients prior to traditional cytoplasmic pathology in vulnerable cells [19]. Further development of these technologies with respect to TDP-43 SUMOylation may help advance biomarker development that can provide information about TDP-43 stress-response and pathogenesis in ALS/FTD patients.

While the extent of phenotypes observed in TDP-43^{K408R} are relatively mild, they similarly reflect the magnitude of phenotypes observed in mice with significant construct validity to ALS/FTD (i.e. TDP-43^{Q331K}, TDP-43^{M337V}, and TDP-43^{K145R} models) [45, 113, 114]. These knock in models highlight potential shortcomings of other TDP-43 models relying on overexpression to induce behavioural phenotypes in mice which may not reflect the underlying biology of TDP-43 in ALS/FTD. The emergence of predominantly cognitive FTD-like phenotypes in the TDP-43^{K408R} mice is not unusual in TDP-43 knock in models such as TDP-43^{Q331K} and TDP-43^{K145R} mice which present with features of cognitive dysfunction but lacking the entire constellation of ALS/FTD-like phenotypes [45, 113]. However, we were surprised to observe that the cognitive phenotypes were specific to female mice with no behavioural phenotypes being observed in male mice. This may imply that TDP-43 plays important role regulating sex specific behaviours. Alternatively, female and male mice may experience different forms of life stress that may act upon SUMOylation pathways. For example, we observed differences in social behaviors which may indicate social pathways linked with female behaviour may also be associated with SUMOylation. Alternatively, male mice were frequently separated due to fighting behavior, which could contribute to altered baseline social features, regardless of genotype. Future work exploring sex-specific roles of TDP-43 and/or SUMOylation will help provide mechanistic insight into sex-specific behaviour and experience.

As TDP-43 SUMOylation plays roles in regulating TDP-43 clearance during recovery from stress, blocking TDP-43 SUMOylation in the TDP-43$^{K408R/K408R}$ mouse line disrupts this proteostasis and leads to subsequent mislocalization consistent with loss of nuclear function. Additionally, we observe significant increases in insoluble phosphorylated TDP-43 and motor neuron loss in male mice suggesting that gain of function may be occurring, phenocopying disease pathogenesis. While we did observe some motor impairment in 9-month-old mice correlating with TDP-43 mislocalization, we did not observe significant motor impairment in the male mice at 16 months of age, which may be explained by the overall poor performance during motor tests at this age limiting the sensitivity to detect mild changes. Despite this, we did observe molecular and histological evidence supporting early motor impairment with significant neuromuscular junction denervation and reduction in ChAT positive motor neurons in the ventral horn. Additionally, as the male TDP-43$^{K408R/K408R}$ mice displayed a significant decrease in survival, behavioral analysis at 16 months of age may have preceded the onset of significant motor phenotypes. Future refined studies using key pathological centered around key pathological markers of cellular dysfunction will help uncover specific points of phenoconversion and phenotransition to identify the chronology of events leading to phenotypes associated with neurodegeneration.

We have demonstrated that TDP-43 SUMOylation occurs in response to cellular stress, thus careful characterization of the TDP-43^{K408R} mice is critical to determine baseline phenotypes without the addition of exogenous stressors. We initially hypothesized that aging may be a sufficient stressor to interrogate TDP-43 SUMOylation in mice leading to age-dependent phenotypes. However, the various stressors that individuals with ALS/FTD were previously exposed to during their lifetime (i.e. the "exposome") are not experienced by mice in vivaria on a short timescale thus mouse aging likely does not faithfully reflect human aging. The TDP-43^{K408R} model will therefore help facilitate the exploration of how the exposome synergizes with TDP-43 to better understand how ALS/FTD relevant stressors that humans may experience throughout aging (e.g. *C9ORF72* expansions, viral infections, and traumatic brain injury) converge on TDP-43 and uniquely drive aspects of neurodegeneration.

Materials and methods

Materials availability

Plasmids generated in this study will be deposited to Addgene and/or available upon request. Mouse lines generated in this study are available upon request.

Data and code availability

Human tissue data reported in this paper will be shared by the lead contact upon request. Any additional information required to reanalyze the data reported in this paper is available from the lead contact upon request.

Cloning of pEGFP-TDP-43 plasmid and variants

For expression of C-terminally tagged TDP-43-EGFP, human TDP-43 was subcloned out of a wtTDP-43tdTOMATOHA (gift from Zoushang Xu, Addgene # 28205) via XhoI and Kpn1 double digest and inserted into a pEGFP-N3 (Clontech) backbone and validated by sanger sequencing. Site directed mutagenesis was performed using QuikChange II XL (Agilent 200521) following manufacturer instructions. Primers for site directed mutagenesis can be found in Table S4. Several TDP-43 variants were generated through the uOttawa Genome Engineering and Molecular Biology facility or designed and ordered through twist bioscience and were subcloned into the pEGFP-TDP-43 backbone for consistency using XhoI and HindIII double digest, see Table S4 for plasmids used/generated in this study.

Cell culture

HEK293T cells were cultured in DMEM outgrowth media containing 10% FBS (unless otherwise stated) and antibiotic/antimycotics at 37 °C with 5% CO_2.

Generation of pL302-HA-SUMO2 stable HEK293T cell line

To generate a pL302-HA-SUMO2 lentivirus-compatible vector for stable HA-SUMO2 expression, HA-SUMO2 was subcloned from pcDNA-HA-SUMO2 (gift from Guy Salvesen, Addgene #48967) and inserted into the pL302 lentiviral backbone (gift from Jacqueline Burré and Thomas Südhof at Stanford). Briefly, extension PCR was performed to add an Xba1 restriction site to the 5′ and 3′ ends of the HA-SUMO2 insert using PCR amplification using forward primer sequence: *5′- ggctgcaggtcgactctagaaaagcttatggatgcctaccc-3′*, and reverse primer sequence: *5′- tggctgcaggtcgactctagatgcatgctcgagtcaacct-3.′* The PCR amplicon and pL302 backbone were digested with XbaI and the amplicon was ligated into the pL302 backbone. Colonies were screened by sanger sequencing to ensure proper orientation and copy number of the insert. Next the pL302-HA-SUMO2 plasmid was packaged into lentivirus by co-transfection of psPAX2 (Gift from Didier Trono, Addgene #12259), and pMD2-G (Gift from Didier Trono, Addgene #12260) into HEK293T cells and subsequent media collections. Viral media was filtered through a 0.45 µm filter then concentrated by centrifugation at 100,000G for 2 h at 4 °C and the pellet was resuspended in 1X PBS. Fresh HEK293T cells were transduced with pL302-HA-SUMO2 virus to generate a stable polyclonal cell line.

GFP-trap SUMOylation assay

~250,000 HEK293T and/or pL302-HA-SUMO2 HEK293T cells were seeded (experiment dependent) in a 6-well plate. The following day, plasmids were transfected to express TDP-43-GFP (or mutant variants) and/or HA-SUMO variants and allowed to incubate for 48 h for optimal expression. Cells were treated with 250 µM $NaAsO_2$ for one hour (or variations of time, concentration, or chemical depending on assay), after which cells were immediately collected by scraping the bottom of the well and pelleting the samples by centrifugation at 2500G for 5 min at room temperature. The supernatant was then aspirated, and the cells were flash frozen or immediately lysed in 450 uL of ice cold 1X Denaturing Lysis buffer (1X RIPA, supplemented with 1X protease inhibitor, 1X phosphatase inhibitor, 50 mM N-Ethylmalamide, and 5% 2-mercaptoethanol) and boiled at 95 °C for 5 min. After boiling, 450 uL of ice cold 1X Lysis buffer (1X RIPA, supplemented with 1X protease inhibitor, 1X phosphatase inhibitor, 50 mM N-Ethylmalamide) was then added to the sample, and cells were left on ice for 20 min with vortexing every 5 min for 10 s. Next, the cell lysates are centrifuged at ~ 21000G for 20 min at 4 °C and during this time, 30 uL of GFP-Trap beads (Bulldog Bio) per sample were washed 3 times in cold 1X RIPA buffer then aliquoted equally into microcentrifuge tubes for each sample. Following the centrifugation, 1–3% of the supernatant was transferred into a microcentrifuge tube to be used as the *Input* sample. The remainder of the supernatant was transferred into a microcentrifuge tube containing the GFP-Trap beads as the immunoprecipitation sample and was then placed on a rotator for 45 min at 4 °C. After the incubation, the solution was aspirated, and the beads were washed using cold 1X RIPA buffer 5 times. Samples were eluted in 30 µL of 2X Laemmli buffer containing 10% Beta-Mercaptoethanol and boiled at 85 °C for 10 min at 1250 rpm on a thermomixer. The input samples were prepared with 4X Laemmli buffer containing 10% Beta-Mercaptoethanol and then boiled at 85 °C for 10 min. Samples were then analyzed by Western Blot. Quantification of SUMOylation assays was performed through densitometry analysis using ImageLab (BioRad) to quantify the volume of the ~ 95 kDa anti-HA bands from the immunoprecipitation standardized to the anti-GFP pulldown. For quantification of changes in TDP-43 SUMOylation response, conditions were normalized to the 1 h sodium arsenite treatment for wild type TDP-43.

SUMOylation assay

~500,000 HEK293T and/or pL302-HA-SUMO2 HEK293T cells were seeded (experiment dependent) in a 6-well plate. The following day, cells were treated respective of their experiment after which cells were immediately collected by scraping the bottom of the well and pelleting the samples by centrifugation at 2500G for 5 min at room temperature. The supernatant was then aspirated, and the cells were flash frozen or immediately lysed in 100 uL of 1% SDS buffer (1% SDS in IP Lysis Buffer supplemented

with 1X protease inhibitor, 1X phosphatase inhibitor, 100 mM N-Ethylmalamide), vortexed for 20 s then boiled at 95 °C for 10 min. After boiling, 900 µL of ice-cold IP Lysis buffer was then added to the sample, and cells were left on ice for 20 min with vortexing every 5 min for 10 s. Next, the cell lysates are centrifuged at ~ 21000G for 20 min at 4 °C. Following the centrifugation, 1–3% of the supernatant was transferred into a microcentrifuge tube to be used as the *Input* sample. The remainder of the supernatant was transferred into a microcentrifuge tube containing 1 to 10 ug of antibody per sample (See Table S4 for concentrations) and incubated overnight rotating at 4 °C. The next day, 50 µL of Protein G Dynabeads (Thermo Fisher Scientific) per sample were washed 3X in ice cold IP Lysis Buffer. The beads were resuspended in 50 µL IP Lysis Buffer per sample which was then added to each of the samples incubated with antibody. The samples were left to rotate at 4 °C for 45 min. Next, the solution was added to a magnetic rack kept at 4 °C and the supernatant was collected for *flowthrough* to test immunodepletion or aspirated. The beads were washed 5X in ice cold IP Lysis buffer. Samples were eluted using 5 ug of synthetic HA peptide (Sino Biological) per 1ug of antibody and incubating at 37 °C for 15 min at 900 rpm on a thermomixer (for anti-HA immunoprecipitations). The input/flowthrough and HA immunoprecipitation samples were prepared with 4X Laemmli buffer containing 10% Beta-Mercaptoethanol and then boiled at 85 °C for 10 min. Samples were then analyzed by Western Blot using light chain specific secondary antibodies. Quantification of SUMOylation assays was performed through densitometry analysis using ImageLab (BioRad) to quantify the volume of the ~ 65 kDa anti-TDP-43 bands from the immunoprecipitation standardized to the loading control of the input. For quantification of changes in TDP-43 SUMOylation response, conditions were normalized to the 1 h sodium arsenite treatment.

Serial protein extraction from cell culture

Soluble protein was extracted using RIPA buffer (supplemented with protease inhibitor, phosphatase inhibitor, and 50 mM N-Ethylmalamide) during immunoprecipitation assays (taken as *Input* prior to immunoprecipitation) or from lysate in cortical neuron experiments. The remaining pellet after the centrifugation step post-lysis was washed in 1 mL RIPA buffer with vortexing for 10 s followed by centrifugation at ~ 21000G for 20 min at 4 °C. The supernatant was carefully removed, and the pellet was resuspended in 300 µL of 2% SDS buffer in PBS for immunoprecipitation assays, or in 300 µL of 8 M UREA in PBS with 10 mM Tris–HCl pH 7.4. Samples were left to solubilize overnight at room temperature before 2X Laemmli was added prior to Western Blot analysis.

Western blot analysis

Protein sample prepared in Laemmli loading buffer was loaded onto 8% polyacrylamide gel, TGx Mini-PROTEAN 4–15% precast gel (BioRad), or Bolt Bis–Tris Plus mini-Protein Gel 4–12% (Invitrogen) and run at 100–140 constant voltage in Tris–Glycine or MES buffer for their respective gels. Proteins were transferred onto a 0.45 µm nitrocellulose membrane at a constant 340 mA for 2 h at 4 °C. The membranes were blocked in 10% milk diluted in TBS-T, washed 5×5 min in TBS-T then incubated in primary antibody overnight (See supplemental Table S4 for antibody concentrations). The following day the membranes were washed for 5×5 min in TBS-T, then incubated in secondary antibody for 1–2 h at room temperature. Finally, the secondary antibody is washed 5×5 min in TBS-T before being imaged using chemiluminescence Clarity Western ECL or Clarity Max Western ECL on an LAS4000 (GE). Densitometry was performed using the volumes function of the ImageLab (BioRad) software.

Total protein analysis

Total protein was stained using Ponceau for all blots except those presenting UREA fraction in which memcode stain was performed. Ponceau stain was performed before probing with primary antibody. Blots were rinsed with 1X TBS-T then incubated in Ponceau stain for 1–3 min. Ponceau was rinsed with MilliQ H_2O 5 times until background was removed and then imaged using white light setting on LAS4000. Ponceau was removed by washing 5×5 min in 1X TBS-T. Blots were then blocked and prepared for primary antibody incubation. Memcode staining was performed following manufacturer instructions and imaged using white light setting on LAS4000. Blots were destained following manufacturer instructions then prepared for primary antibody incubation.

Immunofluorescent microscopy analysis in HEK293T cells

Micro Coverglass #1.5 coverslips (Electron Microscopy Sciences) coverslips were washed in 2 M HCl overnight at 55 °C, washed 5 times in sterile H_2O, then pre-coated with 300 µL poly-D-lysine (10 µg/mL) overnight at 37 °C, then washed with distilled water three times and air-dried at room temperature for at least 2 h or stored at 4 °C until required. 400 000 HEK293T cells were seeded in a 6 well dish and incubated overnight. 1000 ng of plasmid for protein expression was transfected into cells using Lipofectamine 3000 protocol (Thermo Fisher Scientific). Media was changed 4 h post transfection to reduce toxicity. The following day transfected HEK293T cells were split onto coverslips plating ~ 50 000 cells per coverslip. Cells were allowed to adhere for 24 h prior to experimentation (i.e. stress treatment). Cells were fixed using 10% buffered formalin for 10 min, then permeabilized

in blocking buffer (10% serum, 1% Triton X-100, in 1X PBS) for 1 h, then primary antibody diluted in blocking buffer was applied overnight (See Table S4 for antibody concentrations). The following day coverslips were washed 5X in 1X PBS for 5 min then secondary antibody diluted in blocking buffer was applied for 2 h at room temperature. Samples were stained with 1X DAPI (and/or 1:10000 dilution of CellMask Membrane Stain) in PBS for 10 min. Samples were washed 4 more times in PBS for 5 min each. Coverslips were briefly air dried and then mounted on slides using Vectashield Antifade Mounting Medium with DAPI. Z-stack images were obtained on a Zeiss AxioObserverZ1 LSM800 Confocal Microscope at 40× magnification with a 5× digital zoom or 63× magnification with 2X digital zoom through a Z distance of 10–12 µm per image using optimal spacing per slice with dimensions set to 1024× 1024 pixels with 4X averaging per frame. At least 10 cells were imaged per replicate. Images were analyzed and quantified using ImageJ. For Fig.S1A, Z-stack images were obtained on a Zeiss AxioObserverZ1 LSM880 Confocal Microscope at 20× magnification with a 2× digital zoom through a Z distance of 10–12 µm per image using optimal spacing per slice with dimensions set to 1024× 1024 pixels with 2X averaging per frame.

E3 SUMO ligase screen

One day prior to transfection 62,000 HEK293T or HEK293T stably expressing HA-SUMO2 were plated in a 6 well dish. Samples were co-transfected using 800 ng of pCLIP-Dual-sgRNA for each of the SUMO E3 ligases alongside 1200 ng pLenti-Cas9-BLAST and media was changed after 4 h to minimize toxicity. Forty-eight hours after transfection, cells were selected using 2 µg/mL puromycin for 2–3 days. After selection was complete, cells were recovered in outgrowth media. On day 7 post transfection, 6-well plates were coated with 10 µg/mL poly-D-lysine for 1 h at 37 °C then washed 3X in 1X PBS. 200,000 cells were plated into a 6 well dish for each knockout condition and respective controls. The following day, 500 ng of pEGFP-N3 or pEGFP-TDP-43 was transfected for each respective condition and media was changed after 4 h. Cells were incubated for 48 h (10 days post Cas9/sgRNA transfection). Cells were then stressed for 1 h using 250 µM sodium arsenite and GFP-Trap SUMOylation Assay and Western Blot analysis was performed as previously described. Samples were quantified using densitometry by quantifying the volume of the primary SUMOylated TDP-43 band at ~ 98 kDa, standardizing to the volume of the immunoprecipitated TDP-43-GFP signal at ~ 70 kDa, and normalizing to the stressed positive control sample without sgRNA on each blot.

AlphaFold3 TDP-43 structure prediction

TDP-43 structure was predicted using the AlphaFold3 server (https://alphafoldserver.com/) using FASTA sequence of Human TDP-43 (Uniprot TADBP_HUMAN, Q13148) with relevant mutations. UG×6 (5'-UGUGUG UGUGUG-3') RNA sequence was included for structure predictions [115].

Conservation analysis of TDP-43 K408

Representative FASTA amino acid sequences of TDP-43 paralogs were aligned for phylogenetic analysis using MUSCLE multiple alignment and PhyML maximum likeliness for phylogenetic tree generation [116]. Pairwise alignment of the C-terminal domain was performed using Geneious Prime 2022.1.1 (https://geneious.com) performing a MUSCLE multiple alignment of 300 FASTA amino acid sequences of TDP-43 paralogs between Humans and Actinopterygii representing the emergence of [human] K408 curated from the OrthoDB database (Table S1).

TDP-43^{K408R} mouse line generation

At The Centre of Phenogenomics (SickKids, Toronto, ON, Canada), the *TDP-43*^{K408R} mice were generated on a C57BL6/N background based on previous methods [117] using CRISPR/Cas9-mediated gene editing of the endogenous *Tardbp* locus. In brief, spCas9 loaded with an sgRNA to target exon 6 of *Tardbp (MGI:2387629; 5'-TGG GGGCTTTGGCTCGAGCA-3')* was electroporated into embryos alongside a single stranded oligonucleotide (ssODN) repair template (5'-*CTAAATCTACCTAACC TAATAACCAACCTACTAACCACCCCCCACCACC TACATTCCCCAGCCAGAAGACcTAGAATCCATG-gaCGAGCCAAAGCCCCCATTAAAACCACTGCCCGA TCCTGCATTTGATGCTGACCCCCAACCAAGGGG GGC-3'*). Embryos were screened via allelic discrimination (see "TDP-43^{K408R} genotyping" below) to identify founders. Four founders were crossed to C57BL6/N mice to ensure germline transmission of knock-in allele.

Mouse husbandry

All mouse procedures were carried out in accordance with the Canadian Council on Animal Care and approved by the University of Ottawa Animal Care Committee. All mice were group housed (3–5 per mice cage) with access to food and water ad libitum on a standard 12-h light dark cycle. Exceptions included adult male mice who were separated and single housed if persistent fighting and fight wounds were observed in the cage. All experimental mice were given crinkle paper in addition to the standard nestlet and hut enrichment material. Husbandry was completed by University of Ottawa Animal Care and Veterinary Services except for cohorts

actively undergoing behavior testing for which husbandry was completed by the experimenter.

Mouse wellness monitoring

Mice were monitored weekly starting at age P21 and included assessment of hindlimb clasping, kyphosis, weight, and general health. The hindlimb function was assessed following previous methods [118]. Briefly, the mouse was suspended in the air for approximately 5–10 s by the base of the tail. Features of the limbs were assessed to give a score from 0–4. Kyphosis was assessed by allowing the mice to briefly walk on the flat table top in the housing room and visually observing the straightness of the spine. A score of 0–3 was given based on previously described methods [119]. Weight was measured every other week by placing individual mice on a digital weigh scale. Notably, mice exhibiting barbered patches were monitored and recorded.

Sex and age of experimental mice

Experiments were performed using both male and female mice sufficiently powered to detect sex differences. In some instances where no sex differences were observed, male and female mice were grouped together to assess genotypic differences independent of sex. Experiments involving primary cortical neurons cultures dissected from individual embryos were used involving a mixture of male and female embryos. Experimental animals underwent behavioral testing as early as P21 and as late as 16 months of age. See Table S2 for number of animals used (distinguished by sex and genotype), raw behavior data, and specific statistical analyses for each behavior experiment.

TDP-43^{K408R} genotyping

Tail samples were collected prior to weaning and again postmortem for genomic DNA (gDNA) isolation and genotyping. Tails were solubilized in 300 µL solubilization buffer (10X SET, 100 mM NaCl, 100 µg/mL Proteinase K (Bio Basic PB0451-250)) at 55 °C overnight. Cell debris was precipitated by adding 150 µL of "Tail Salts Buffer" (4.31 M NaCl, 0.63 M HCl, 10 mM Tris–HCl, pH7.4) then samples were centrifuged at ~ 21,000 *g* for 15 min at 4 °C. Supernatant containing gDNA was transferred into 600 µL of chilled 100% ethanol to precipitate nucleic acids which were then pelleted by centrifugation for 10 min at ~ 21,000 *g* at 4 °C. The supernatant was carefully removed, and the pellet was washed in 600 µL of chilled 70% ethanol then centrifuged at ~ 21,000 *g* at 4 °C for 5 min. The supernatant was carefully removed, and residual supernatant was left to evaporate for 5 min. The gDNA pellet was resuspended in double distilled H2O at 55 °C for 10 min. Genotyping reaction was prepared in a 10 µL reaction containing ~ 5 ng of gDNA, 250 nM *K408R Genotyping Forward* primer (5'-*CCACCATTC TAAATCTACCTAACCTAATA-3'*), 250 nM *K408R Genotyping Reverse* primer (5'-*GGATCGGGCAGTGGTTTT A-3'*), 125 nM wild type Locked Nucleic Acid (LNA) probe (*HEX-TCT + A + A + GT + CT + TCT + GGC-IowaBlack FQ*), 125 nM K408R LNA probe (*FAM-TCT + A + G + GT + CT + T + CT-IowaBlack FQ*), and 2X PerfeCTa qPCR Tough Mix (QuantaBio). Reactions were run on a BioRad CFX96 qPCR thermocycler with the following cycling parameters: Initial annealing at 95 °C for 2 min, followed by 40 cycles of 95 °C for 15 s then 60 °C for 60 s. Results were analyzed via allelic discrimination in the BioRad Maestro software. See Fig. S2b.

Primary cortical neuron cultures

Pregnant mice were euthanized between gestation E13.5–15.5 with 120 mg/kg Pentobarbital Sodium (Bimeda-MTC, 8015E) delivered via intraperitoneal injection. The embryos were removed and placed into ice cold 1X PBS. For each embryo, the cortices were carefully isolated and meninges removed and then placed in ice cold HBSS (Sigma Aldrich). Cortices were dissociated for 20 min with trypsin (Thermo Scientific) at room temperature on a rotator before trypsin inhibitor with DNase solution was added to quench the reaction. Cells were pelleted at 2,500 × *g* for 5 min at 4 °C. The supernatant was carefully removed and the pellet was washed with trypsin inhibitor plus DNase solution. Cortical neurons were pelleted at 2,500 × *g* for 5 min at 4 °C. The supernatant was carefully removed and the neurons were resuspended in 1 mL of ice cold outgrowth media (Neurobasal media (Thermo Scientific), supplemented with 1X B-27 (Thermo Scientific), 1X N-2 (Thermo Scientific), 500 µM L-Glutamine (Wisent Bioproducts), and 0.5% penicillin/streptomycin (GE Healthcare Life Sciences)). Culture dishes and coverslips were prepared in advanced coated with 50 µg/mL Poly-D-Lysine overnight at 37 °C specific to each experiment detailed below. Cultures were maintained for 7–9 days in vitro prior (DIV) to experimentation.

Murine primary neuron culture maintenance

Primary cortical neurons were dissected and maintained in Neurobasal media (Thermo Scientific), supplemented with 1X B-27 (Thermo Scientific), 1X N-2 (Thermo Scientific), 500 µM L-Glutamine (Wisent Bioproducts), and 0.5% penicillin/streptomycin (GE Healthcare Life Sciences) at 37 °C with 5% CO_2. Each neuron culture was harvested from a single embryo representing one biological replicate. The sex of the embryos/cultures were not determined thus experiments contain a mix of both male and female replicates.

Endogenous SUMOylation assay from ex vivo embryonic mouse brains

Mouse embryos were harvested following *Cortical Primary Neuron Culture* methods described above. Brains were dissected from embryos and stored in ice cold HBSS (Sigma Aldrich). Brains were cut using a razor blade down the midline evenly to separate hemibrains and each hemibrain was transferred into a 1.5 mL microcentrifuge tube containing neurobasal complete media used in cortical *Primary Cortical Neuron Culture Maintenance* described above. One hemibrain was subjected to 42 °C heat shock for 1 h while the complementary hemibrain was maintained at 37 °C for 1 h as a control. Samples were briefly centrifuged at 2000 g for 2 min to pellet hemibrain, then supernatant was carefully removed. The hemibrain pellets were immediately lysed in 100 µL of 1% SDS buffer (1% SDS in IP Lysis Buffer supplemented with 1X protease inhibitor, 1X phosphatase inhibitor, 100 mM N-Ethylmalamide), and homogenized with a pestle then boiled at 95 °C for 10 min. After boiling, 900 µL of ice-cold IP Lysis buffer was then added to the sample then samples were vortexed aggressively for 10 s and passed through a 18G insulin needle. Lysates were left on ice for 20 min with vortexing every 5 min for 10 s to ensure complete lysis. Next, the lysates were centrifuged at ~ 21000G for 20 min at 4 °C. Following the centrifugation, 1–3% of the supernatant was transferred into a microcentrifuge tube to be used as the *Input* sample. The remainder of the supernatants were equally divided (~ 450 uL each) into two separate 1.5 mL microcentrifuge tubes containing 10 µg of normal mouse IgG (Alpha Diagonstic 20008–250) or 10 ug of anti-SUMO2/3 clone [8A2] (Abcam ab8137) per sample. Samples were incubated overnight rotating at 4 °C. The next day, 50 µL of Protein G Dynabeads (Thermo Fisher Scientific) per sample were washed 3X in ice cold IP Lysis Buffer. The beads were resuspended in 50 µL IP Lysis Buffer per sample which was then added to each of the samples incubated with antibody. The samples were left to rotate at 4 °C for 45 min. The solution was added to a magnetic rack kept at 4 °C and the supernatant was collected for *flowthrough* to test immunodepletion or aspirated. The beads were washed 5X in ice cold IP Lysis buffer. Samples were eluted using 30uL (at 1 mg/mL) of synthetic SUMO2/3 peptide (Amino Acid Sequence: *IRFRFDGQPI*, synthesized through Genscript) per sample and incubating at 37 °C for 15 min at 900 rpm on a thermomixer. The input/flowthrough and immunoprecipitation samples were prepared with 4X Laemmli buffer containing 10% Beta-Mercaptoethanol and then boiled at 85 °C for 10 min. Samples were then analyzed by Western Blot using light chain specific secondary antibodies. Quantification of SUMOylation assays was performed through densitometry analysis using ImageLab (BioRad) to quantify the volume of the ~ 62 kDa anti-TDP-43 bands from the immunoprecipitation standardized to the loading control of the input. For quantification of changes in TDP-43 SUMOylation response, conditions were normalized to the 1 h sodium arsenite treatment.

Immunofluorescence in primary cortical neurons

Micro Coverglass #1.5 coverslips (Electron Microscopy Sciences) coverslips were washed in 2 M HCl overnight at 55 °C, washed 5 times in sterile H_2O, then pre-coated with poly-D-lysine (50 µg/mL) overnight at 37 °C, then washed with distilled water three times and air-dried at room temperature for at least 2 h. Primary mouse cortical neurons were seeded at 75,000–100,000 cells per coverslip and cultured as described above. On day 7, neurons were fixed for 10 min using 10% phosphate buffered formalin for (Fisher Chemical, SF100-4) followed by 3× 5-min washes in 1 mL of 1X PBS. Neurons were blocked in 500 µL of blocking buffer (1% Triton X-100, 10% cosmic calf serum in 1X PBS) for 1 h, then incubated in 300 µL of primary antibody diluted in blocking buffer overnight at 4 °C (See Table S4 for antibody concentrations). The following day, the neurons were washed for 5× 5-min in 1 mL of 1X PBS then incubated in 300 µL of secondary antibody diluted in blocking buffer for 2 h at room temperature. Neurons were then washed in 1 mL 1X PBS, then stained with DAPI for 10 min at room temperature followed by 4× 5-min washes in 1X PBS before being mounted using antifade fluorescence mounting media (Dako, S3023). Z-stack images were obtained on a Zeiss AxioObserverZ1 LSM800 Confocal Microscope at 40× magnification with a 2× digital zoom through a Z distance of 10–12 µm per image using optimal spacing per slice with dimensions set to 1024× 1024 pixels with 4X averaging per frame. At least 50 cells were imaged and quantified per replicate. For TDP-43 foci colocalization, Z-stack images were obtained on a Zeiss AxioObserver Z1 LSM880 AiryScan2 confocal microscope at 63× magnification with 3X digital zoom at 512× 512 resolution. At least 10 cells presenting with TDP-43 foci were imaged per replicate. Images were analyzed and quantified using ImageJ.

TDP-43 colocalization with HSPA1L

HSPA1L colocalization experiment was designed similar to previous approaches that identified TDP-43 forming anisosomes in response to stress [92]. HSPA1L-mRuby2 was designed and synthesized in a pTwist-Lenti-Puro backbone (Twist Bioscience). Next the pTwist-Lenti-HSPA1L-mRuby2 plasmid was packaged into lentivirus by co-transfection of psPAX2 (Gift from Didier Trono, Addgene #12259), and pMD2-G (Gift from Didier Trono, Addgene #12260) at equimolar concentrations

into HEK293T cells. After 24 h, media was changed and discarded. Media was collected 48 h and 72 h post transfection. Viral media was filtered through a 0.45 µm filter then concentrated by centrifugation at 100,000 g for 2 h at 4 °C and the pellet was resuspended in 1X PBS. Cortical primary neurons were cultured as previously described and lentiviral infection was performed at the time of plating (0 DIV). Cells were cultured to 7 DIV then were stressed with 250 µM sodium arsenite for 1 h and recovered for 3 h to induce TDP-43 foci formation. Cells were fixed in 10% formalin for 10 min and immunofluorescent staining was performed for TDP-43 as described above. Z-stack images were obtained on a Zeiss AxioObserver Z1 LSM880 AiryScan2 confocal microscope at 63× magnification with 3X digital zoom at 512×512 resolution. At least 10 cells presenting with TDP-43 foci and HSPA1L foci were imaged per replicate. Images were analyzed and quantified using ImageJ.

Proximity ligation assay in primary cortical neurons

Primary mouse cortical neurons were cultured and fixed as described in *primary cortical neuron cultures* and *immunofluorescence in primary cortical neurons*. Fixed coverslips were transferred into 12-well plates and outlined with a hydrophobic pen and blocked using 40 µL of Duolink blocking buffer (Sigma Aldrich, DUO82007) at 37 °C for 1 h. Coverslips were then washed for 3×5 min in 1 mL 1X PBS. Next, coverslips were incubated in 300 µL of primary antibody (anti-TDP-43 1:750, PTGLabs; anti-SUMO2/3 [8A2] 1:500 Sigma) diluted in blocking buffer (1.5% Triton X-100, 10% cosmic calf serum in 1X PBS) overnight at 4 °C. The next day, the coverslips were washed for 3×5 min in 1 mL of Duolink Wash Buffer A (0.01 M Tris-Base, 0.15 M NaCl, 0.05% Tween-20, pH 7.4) followed by incubation at 37 °C for 1 h in 40 µL of dilute probe mixture containing a 1:5 dilution of Duolink PLA MINUS (Sigma Aldrich, DUO82004) and PLUS probes (Sigma Aldrich, DUO82002) in antibody diluent (Sigma Aldrich, DUO82008). Duolink PLA probes were diluted in antibody diluent (Sigma Aldrich, DUO82008) at a 1:5 dilution. Coverslips were washed for 3×5 min in Duolink Wash Buffer A and then incubated in 40 µL of ligase (Sigma Aldrich, DUO82027) diluted in 1X ligation buffer (Sigma Aldrich, DUO82009) at a 1:40 dilution at 37 °C for 30 min. The coverslips were then washed for 3×5-min washes in Duolink Wash Buffer A and then incubated in 40 µL of polymerase (Sigma Aldrich, DUO82028) diluted 1:80 in 1X amplification buffer (Sigma Aldrich, DUO82011) at 37 °C for 90 min. Next, the coverslips were washed 2×10 min in Duolink Wash Buffer B (0.2 M Tris-Base, 0.1 M NaCl, pH 7.5) and then again in 1 mL of Duolink Wash Buffer B diluted at 1:100 in 1X PBS for 1 min. Coverslips were briefly air dried and then mounted on slides using Vectashield Antifade Mounting Medium with DAPI. Z-stack images were obtained on a Zeiss AxioObserverZ1 LSM800 Confocal Microscope at 63× magnification with a 5× digital zoom through a Z distance of 10–12 µm per image using optimal 0.27 µm spacing per slice with dimensions set to 512×512 pixels with 2X averaging per frame. ~ 5 images were randomly obtained around the coverslip sampling > 15 cells per condition per replicate. Images were analyzed and quantified using the Spots function on the Imaris (ver. 9.9.1 Bitplane, Switzerland) software.

Behavior testing general information

All adult behavior testing was performed in the University of Ottawa Behaviour and Physiology Core. During behavior testing periods the mice were minimally disturbed: food and water were only added/changed as needed and cages were changed by the experimenter with a transfer of old bedding material. Apart from nesting and Beam Break testing, all behavior tests were performed in the light phase of the cycle. The experimenter was blinded to the genotype of the mice during behavior testing and until the mice were end pointed. Mice were brought to the testing room to habituate in dim white light at least 30 min prior to commencing testing with the exceptions of nest building and fear conditioning for which there was no habituation period. The behavior cohort consisted of males and females with 12–15 animals per sex per genotype. These mice had been backcrossed three times to C57BL/6N background. All mice used for histology, biochemistry, and RNA analyses performed the fear conditioning test 1 week prior to dissections to control for potential molecular changes induced by this behavior test.

Developmental testing

A small battery of behavior tests was completed at P8 and P21. At P8, these tested included (I) weight, (II) righting reflex, (III) hindlimb suspension, and (IV) forelimb suspension. (I) Weight was measured every other week by placing individual mice on a digital weigh scale. (II) Mice were placed on their back on a tabletop and timed for how long it took them to right themselves onto their paws. (III) Mice were placed facing downward in a 50 mL Falcon tube (VWR 21008–940) and timed for their latency to fall. (IV) Mice were placed to grasp a wire suspended by a pencil holder and timed for latency to fall. At P21, hanging wire was performed in which the mouse was allowed to grasp a wire 30 cm off the ground and time for its latency to fall. Each mouse completed three trials with a maximum time of 60 s.

Beam break

The Beam Break test was used to assess general locomotor activity and habituation to a novel cage environment. The apparatuses used to record and analyze the mice activity included the Micromax analyzer/Fusion Software (Omnitech Electronics; Columbus, OH, USA) at the 2-month time point and the Photobeam Activity System (San Diego Instruments; San Diego, CA, USA) at the 9 and 16-month timepoints. Clean cages with only a thin layer of corncob bedding, food, and water were loaded into the recording frame. Mice were singly housed in one of these cages 2 h prior to the start of their dark cycle. For a 24-h period at the standard 12-h dark/light cycle, the activity of the mice was monitored by infrared beam emitters and receptors. When the test was completed, the sum of the infrared beam breaks in 5-min, 1-h, and 24-h sampling bins was analyzed.

Digigait

The Digigait treadmill Imager and Analysis Software (Mouse Specifics Inc.) were used to record and analyze parameters of gait, respectively. Mice were placed on the unmoving treadmill surface and once recording was started the speed was increased to 18 cm/s with 0 degree incline. A 3 s video of each mouse walking continuously, with no stopping or starting, was captured. A mouse was excluded from the test if it was unable to walk for 3 s at the 18 cm/s speed. Digiait data was analyzed using FactoMinR [120] and visualized using FactoExtra [121] packages in R (version 4.2.3).

Fear conditioning

Contextual and cued fear conditioning were tested using a 3-day protocol to assess associative fear learning and memory. Naïve age and sex matched mice were initially used to determine the optimal shock value. On day 1 (training), the mice were placed into a Phenotyper box (Noldus Information Technology) with a grid shock floor (Med Associates). The testing room was set to 60 lx light level and 70 dB of white noise (context A). The mice were left in the apparatus for 6 min during which they receive 3 tone-shock pairings (30 s tone co-terminated with a 2 s foot shock). On day 2 (Context), the mice were placed in the same apparatus (Context A) with no tone or foot shock delivered for the 6-min trial. On day 3 (cue), the animals were placed in the test apparatus with an altered context (context B) including red light, no white noise, vanilla scent, textured mat covering the shock floor and plastic inserts in the apparatus. The mice are allowed to explore this context with no tone for 3 min, and then are presented with the same tone from Day 1 for the last 3 min. The time freezing was analyzed with EthoVision software for all 3 testing days.

Grip strength

A grip strength meter (Chatillon DFE II, Columbus Instruments) was used to assess the maximal forelimb grip strength of the mice. The grip strength meter was rotated vertically and temporarily mounted on a flat surface prior to testing. The mouse was brought near the triangular attachment and allowed to grasp the lower bar with its forepaws. The mouse was pulled directly downward, by the tail, in one smooth motion. Each mouse was tested, and the grip strength recorded for 5 consecutive trials with a 1-min intertrial interval. If a trial was deemed unsuccessful by the blinded experimenter, the trial was redone. Causes of an unsuccessful trial included the mouse prematurely losing its grip on the bar or grasping the bar with its hindfoot. The average grip strength for the 5 successful trials was analyzed.

Hanging wire

The hanging wire test was used to assess muscle strength and coordination. A metal wire was secured to the top of a tall plastic box with padding on the bottom. The mouse was brought near and allowed to grasp the wire with its forepaws. A timer was started once the experimenter released the mouse to allow it to hang freely. When the mouse fell from the wire the time was recorded. Mice had three trials and were allowed to hang for a maximum of 600 s with a 60 s intertrial interval in between. If a mouse hung for 600 s, it did not complete any additional trials. The maximum hanging time from the trials was used for analysis.

Light/dark box

The light dark paradigm was used to assess anxiety-like or disinhibited, exploratory behavior. The testing apparatus (Med Associates) has two equal sized rectangular compartments the mouse can move freely between. The one is fully illuminated whereas the other is covered by a black plastic insert. The position of the mouse in the apparatus testing field is recorded using infrared beams. To start the test, the mice are placed into the lit side and allowed to explore for 10 min. The time spent in each compartment and number of entries into each compartment was recorded and analyzed by Activity Monitor software (Med Associates).

Marble burying

The marble burying assay can assess the motor function required to bury objects as well as cognitive changes related to apathy or perseverance. Cages were filled with 10 cm of fresh corncob bedding and one mouse was placed to habituate for 5 min. After habituation, 20 glass marbles were laid out evenly in a 4 by 5 pattern. The mouse was returned to the cage and left alone for 30 min

in 60 lx light. With the completion of the trial, the number of marbles buried by at least two thirds was scored by a blinded experimenter.

Nest building

Nest building is an innate behavior of mice in their daily lives. This complex behavior requires both executive planning and sensorimotor coordination. Directly following Beam Break testing, a single square nestlet (5 cm^2 cotton pad) was placed in each Beam Break cage for 16 – 18 h, of which 12 of these hours was during the dark cycle. At the end of the test, images were taken of the nests and scored blindly for quality as previously described on a scale from 1–5.

Open field

The open field test was used to assess anxiety and locomotor activity in a novel environment. The apparatus consists of white plastic square arenas measuring 45 cm on each side. The mice were placed in a corner of the arena and allowed to freely explore for 10 min with light levels at 300 lx. The distance travelled, time spent in the corners and center of the field was recorded and analyzed by EthoVision software (Noldus Information Technology).

Rotarod

The rotarod (IITC Life Science, Ugo Basile) was used to test the motor performance of mice including coordination and resistance to fatigue. Mice were placed in the stationary rotarod bar for 10 s before the rotarod program was initiated. The bar accelerated from 4 to 40 rpm for 5 min and the latency to fall for each mouse was recorded. The time was stopped when the mouse fell from the bar or rotated passively. Mice were completed four trials per day, with a 10-min intertrial interval in their home cage, for 3 consecutive days.

Spontaneous Y-maze

The spontaneous Y-Maze test was used to assess spatial working memory. The Y-shaped maze has three identical arms at 120 °C around a center point triangle. The mice were placed in the center point and allowed to freely explore the arms for 8 min. The movement of the mouse was tracked including the sequence of arm entries by EthoVision (Noldus Information Technology). An alternation is defined as the mouse making consecutive, sequential entries into each of the three arms without revisiting an arm. The alternation index was calculated as (number of alternations/(total number of arm entries minus two)) and reported as a percent.

Tail suspension

The automated Tail Suspension apparatus (Med Associates) was used to assess apathetic-like behaviors of the mice. Mice were taped and suspended by the tail to a vertical steel bar which measures strain gauge as the mouse moves during a 6-min trial. The cumulative time spent immobile, hanging passively (below lower threshold) was measured by the Tail Suspension software.

Three chamber sociability

The Three Chamber test was conducted to measure the sociability of mice when allowed to interact with a novel mouse or a similarly sized inanimate object. The testing apparatus is a 19×45 cm plastic box divided into three equal chambers with clear plastic wall dividers. The two external chambers each have a single weighted metallic mesh pencil holder and the central chamber is empty. The mice are habituated to the apparatus for 5 min by being placed in the central chamber and allowed to freely explore and enter all chambers. The mouse has a 5-min intertrial interval in its home cage. In the test trial, a sex and age matched wild type mouse (social target) is placed beneath one mesh pencil holder, and an inanimate plastic toy (non-social target) is placed beneath the other. To commence the test trial, the mouse is paced in the central chamber. The time spent in each chamber and interacting with the social or non-social target is recorded and analyzed by EthoVision software (Noldus Information Technology).

Tube test of social dominance

Tube test was used to assess social dominance and within cage social hierarchy. Cage mates were paired against each other for testing in a round-robin design. The tube test was conducted on a flat tabletop, which the mice were allowed to run around on for 5 min prior to commencing the testing. One foot of vinyl tubing was used. Mice were habituated to the tube prior to testing on the same day by encouraging them to run through the empty tube from either side 5 times. A blinded experimenter placed a mouse on either end of the tube, and released their tales when they completely entered the tube. The first mouse to step its hind paws out of the tube lost the battle. The battle was redone if after 2 min no mouse had won.

Collection and preparation of mouse tissue

Mice were harvested for both histology and biochemistry/molecular analyses to reduce total animal numbers. Mice were first acclimated for 2 h prior to dissection to help control for activity-induced changes and all dissections were performed at zeitgeber hours ZT6 to ZT11 to control for potential circadian affects. Mice were

randomly dissected by cage to limit batch effects and additional stress. Mice were anesthetized using isoflurane inhalation, blood was collected, and then mice were sacrificed via decapitation and the brains were quickly isolated, weighted, then cut into 2 hemispheres where the left hemisphere was drop fixed in 10% buffered formalin and the right hemisphere was dissected by region and flash frozen on dry ice. Spinal cords were removed using hydraulic extrusion and the lumbar spinal cord was isolated. The lumbar enlargement was isolated for histology whereas the remaining lumbar spinal cord was used for molecular analysis. Tibialis anterior and soleus muscles were isolated and drop fixed in 10% buffered formalin for imaging studies and gastrocnemius muscle was flash frozen.

Real Time-Quantitative PCR (RT-qPCR) assay

RNA was extracted from mouse cortex tissue using RNeasy Mini Kit (QIAGEN) following manufacturer's instructions. cDNA was synthesized using 5X All-in-One RT Master Mix (Bio Basic) following manufacturer's instructions. RT-qPCR was performed using Green-2-Go qPCR Master Mix (Bio Basic). Reactions were run on a BioRad CFX96 thermocycler (protocol: 95 °C for 5 min, 40 cycles of 95 °C for 15 s and 60 °C for 60 s, followed by a standard melting curve). Relative change is splicing was quantified using *MAPT* isoform values standardized to the average of *GAPDH* and *HPRT1* Ct values, then the ratio of each isoform (1N/0N and 2N/0N) were calculated before normalizing to the average of the wild type samples.

Preparation of mouse tissue for analysis by histology

Tissue was collected as described in *Collection and preparation of mouse tissue*. Following fixation for 48 h, samples were transferred to a 70% ethanol solution and sent to the Louise Pelletier Histology Core facility at the University of Ottawa for paraffin embedding and microtome sectioning. The samples were sectioned at a thickness of 5 µm. Serial sectioning was performed at four levels within the tissue each separated by 40 µm. For staining, slide-mounted sections were deparaffinized in 100% xylenes (Fisher Scientific X3P-1GAL) for 10 min, then transferred into a second container of fresh 100% xylenes for an additional 10 min. The slides were then rehydrated in descending ethanol solutions: two 5 min treatments in 100% ethanol, 5 min in 70% ethanol, and 5 min in 50% ethanol. The slides were then immersed in 1X PBS for at least 5 min to rinse residual ethanol.

Cresyl violet staining

Slides containing PPFE mounted sections were slowly dipped 20 times in 70% ethanol followed by 95% ethanol, 100% ethanol, 95% ethanol, and 70% ethanol. Slides were then submerged in ddH2O for 1 min. Next the sections were incubated in 0.25% Cresyl Violet stain for 2 min. Samples were then dipped 10 times in ddH2O followed by 70% ethanol, 95% ethanol, 0.25% glacial acetic acid, 95% ethanol, and finally 100% ethanol. Permount was applied to sections and mounted with coverslips.

Immunofluorescence analysis in mouse tissue

Antigen was performed by placing slides in 1X sodium citrate buffer (2.94 g sodium citrate 0.5 mL Tween-20 in 1L 1X PBS, pH6) at 95 °C for 30 min then rinsed in 1X PBS. Tissue sections were then blocked in blocking buffer containing 1% Triton-X and serum (5% horse serum, 5% cosmic calf serum, or 1% bovine serum albumin) in 1X PBS for 2 h at room temperature. Next the tissue sections were incubated with primary antibody (See Table S4 for antibody concentrations) overnight at 4 °C. The next day, the sections were washed twice in PBS 1X + 0.1% Triton-X for 5 min each and then 3X in 1X PBS for 5 min each. The slides were then incubated in secondary antibody at room temperature for 2 h. The slides were then washed in 1X PBS + 0.1% Triton-X for 5 × 5-min, before mounting with #1.5 coverslips (Thermo Fisher Scientific 12-544E) and fluorescent mounting media (Dako S3023). The coverslips were sealed with clear nail polish and allowed to dry before imaging. Images of each ventral horn were taken on a Zeiss Axio Imager 2 at 20X magnification. Cells were counted manually per image using Fiji (ImageJ).

Neuromuscular junction analysis

Tissue was collected as described in *Collection and preparation of mouse tissue*. After 24 h of fixation, tibialis anterior muscles were stored in a solution of 1X PBS. Muscle bundles were carefully teased apart from the tissue into 4–5 bundles with forceps. The muscle bundles were transferred to 6-well plate cell culture plate containing 1% Triton-X in 1X PBS overnight at 4 °C under gentile agitation for permeabilization. The next day, the muscle bundles were washed three times in 1X PBS for 5 min at room temperature. They were placed in a blocking buffer solution of 4% bovine serum albumin and 1% Triton-X in 1X PBS at 4 °C overnight. The following day, the muscles were incubated in primary antibody (BTX and NfL/SV2 cocktail, see Table S4) diluted in blocking buffer solution overnight at 4 °C. The next day, the muscle bundles were washed with 1X PBS three times for 5 min and incubated with secondary antibody diluted in

blocking buffer solution at room temperature for 2 h. The muscle bundles were then washed 3 times in 1X PBS for 5 min. The bundles were then placed on slides, mounted with VECTASHIELD® HardSet™ Antifade Mounting Medium (#H-1400), and #1.5 coverslips placed above the muscle bundles. The slides were left at room temperature overnight in the dark to allow the mounting media to cure. Images were taken on a Zeiss LSM800 Confocal Microscope at 20X through a Z-stack with optimal spacing (0.61 µm). Images were taken throughout the entirety of the muscle tissue such that at least 80 neuromuscular junctions per animal were captures. Images were scored manually per image using Fiji (ImageJ). See Fig. S8E for scoring examples.

SUMOylation analysis in human brain tissue

20 mg of frozen human brain tissue was homogenized in 300 µL of RIPA buffer supplemented with protease inhibitor, phosphatase inhibitor, and 50 mM N-Ethylmalamide and vortexed every 5 min for 20 min while incubating on ice. The samples were centrifuged at 21000G for 20 min at 4 °C and the supernatant (RIPA soluble fraction) was carefully removed. 4X laemmli buffer was added and samples were boiled for 5 min at 95 °C then stored overnight at 4 °C. The remaining pellet after the centrifugation step post-lysis was washed in 1 mL RIPA buffer with vortexing for 10 s followed by centrifugation at ~ 21000G for 20 min at 4 °C. The supernatant was carefully removed, and the pellet was resuspended in 300 µL of of 8 M UREA in PBS with 10 mM Tris–HCl pH 7.4. Samples were vortexed and left to solubilize overnight at room temperature before 4X Laemmli was added prior to Western Blot analysis. RIPA and UREA samples were randomly loaded onto gels (separated by fraction) with 4 control samples consistently loaded (aged 20–30) on each gel for normalization. Western blot was performed as described above. Samples were standardized to ponceau signal then normalized to control samples.

Collection and preparation of FFPE human brain tissue

Frontal cortex tissues were collected antemortem from three sporadic ALS/FTLD patients (a 74-year-old male, 67-year-old female and 59-year-old female) obtained through the ALS Clinic at Sunnybrook Health Sciences Centre, Toronto. ALS was diagnosed using the revised El Escorial Criteria (Brooks et al., 2000) and informed consent was obtained with approval from the local ethical review board. The presence of TDP-43 proteinopathy within the frontal cortex was verified through immunohistochemical labeling using rat anti-phosphorylated TDP-43 (p409/410) antibody on formalin fixed paraffin embedded sections. Genetic analyses confirmed absence of mutations in key ALS/FTD-associated genes: *C9orf72*, *SOD1*, *FUS* and *TARDBP*.

Neuropathological assessment of all human PFC tissues from various sites

Human FFPE PFC samples collected from the NIH Neurobiobank, CHEO, and University of Toronto were independently assessed and scored by a neuropathologist to verify TDP-43 pathology. Immunohistochemistry staining was performed on FFPE tissue sections using the Leica bond system. Sections were pre-treated using sodium citrate buffer (pH 7.0, epitope retrieval solution 1) for 20 min and then incubated using a 1:2000 dilution of anti-phosphorylated TDP-43 S409/410 (Cosmo Bio Co. Ltd, #TIP-PTD-P07) for 40 min at room temperature and detected using an HRP conjugated compact polymer system. Slides were then stained using DAB as the chromogen, counterstained with Hematoxylin, mounted on slides and covered with coverslips. TDP-43 pathology was assessed by a score of 0–4 looking for neuronal cytoplasmic inclusions and glial cytoplasmic inclusions, particularly within layers II and V/VI. Scoring: 0 = negative, 1 = very rare inclusions, 2 = inclusions readily visible, 3 = moderate density of inclusions, 4 = highest density of inclusions.

Proximity ligation assay in human FFPE tissue

Formalin fixed paraffin-embedded human brain Sects. (5 µm sections) were deparaffinized using two 10-min washes with xylenes, two 5-min washes with 100% ethanol, one 5-min wash with 70% ethanol, and one 5-min was with 50% ethanol. Deparaffinized sections then underwent sodium citrate antigen retrieval (10 mM sodium citrate, 0.05% Tween-20, pH 6) for 2 h at 80 °C. Sections were then blocked with Duolink blocking buffer (Sigma Aldrich, DUO82007) for 1 h at room temperature. Next, sections were incubated with primary antibodies (anti-TDP-43 1:750, PTGLabs; anti-SUMO2/3 [8A2] 1:500 Sigma) diluted in blocking buffer (1.5% Triton X-100, 10% cosmic calf serum in 1X PBS) overnight at 4 °C. The following day, the sections were washed in Duolink Wash Buffer A (0.01 M Tris-Base, 0.15 M NaCl, 0.05% Tween-20, pH 7.4), followed by incubation in Duolink PLA MINUS (Sigma Aldrich, DUO82004) and PLUS probes (Sigma Aldrich, DUO82002) at 37 °C for 1 h. Duolink PLA probes were diluted in antibody diluent (Sigma Aldrich, DUO82008) at a 1:5 dilution. Sections were washed in Duolink Wash Buffer A and then incubated in ligase (Sigma Aldrich, DUO82027) at 37 °C for 30 min. Ligase was diluted in 1X ligation buffer (Sigma Aldrich, DUO82009) at a 1:40 dilution. Then, the sections were washed in Duolink Wash Buffer A and then incubated in polymerase (Sigma Aldrich, DUO82028) at 37 °C

for 90 min. Polymerase was diluted in 1X amplification buffer (Sigma Aldrich, DUO82011) at a 1:80 solution. The sections were then washed in Duolink Wash Buffer B (0.2 M Tris-Base, 0.1 M NaCl, pH 7.5) and then again in Duolink Wash Buffer B diluted at 1:1000. Finally, sections were incubated with DAPI at room temperature for 15 min. DAPI was diluted at 1:1000 in PBS. Fluorescent mounting media (Dako, S3023) and #1.5 coverslips were then placed over the sections and sealed using clear nail polish. Images were taken on a Zeiss LSM800 Confocal Microscope. 5 images per tissue were randomly collected from grey matter at 63X magnification and 2X digital zoom through a Z stack of 10–12 µm with optimal spacing (0.27 µm) at a resolution of 512×512 pixels. PLA foci were manually counted per image using Fiji (ImageJ).

Statistical analyses

Statistical tests were performed using PRISM 10.2.2. Test type was selected based on the number of comparisons made, repeated measures, and gaussian distribution of the data. Levels of statistical significance are indicated in figure legends.

Supplementary Information

The online version contains supplementary material available at https://doi.org/10.1186/s13024-025-00826-z.

Supplementary Material 1.
Supplementary Material 2.
Supplementary Material 3.
Supplementary Material 4.
Supplementary Material 5.

Acknowledgements

This project was supported in part by an NSERC Discovery Grant and Discovery Launch Supplement to M.W.C.R. (RGPIN-2019-04133 and DGECR-2019-00369); the Canada Research Chairs program to M.W.C.R; the ALS Society of Canada in partnership with the Brain Canada Foundation through the Brain Canada Research Fund, with the financial support of Health Canada, for financial support through the ALS Trainee Award Program 2019 (T.R.S.) and the Discovery Grants Program 2021 (M.W.C.R.); the J.P. Bickell Medical Research Fund (M.W.C.R.); Canadian Institute of Health Research Project Grant (PJT-195691, M.W.C.R.). The Eric Poulin Center for Neuromuscular Disease through the Student Translational Research Awards (T.R.S., V.S.G.); The Canadian Institute of Health Research through the CGS-M award (C.E.P., J.L.Z., V.S.G.); The Ontario Graduate Scholarship Program Award (C.E.P.); NSERC Undergraduate Summer Research Award (T.T.N.); Medical Student Summer Research Program Award (T.T.N); Rising Star in ALS Research 2024 Award in memory of Madeleine Blanc through the Brain Canada Foundation (J.L.Z.); Christopher Chiu senior postdoctoral fellowship (P.M.M.); James Hunter and Family ALS Initiative (J.R.). Human tissue was received from the NIH NeuroBioBank at the University of Maryland, University of Pittsburgh, and Sepulveda sites. The authors also thank all members of the Rousseaux lab for important discussions and critical feedback on the manuscript. The authors also thank the following Core facilities from the University of Ottawa and the Ottawa Hospital Research Institute (OHRI) for use of their facility, equipment, and expertise: the Cell Biology and Imaging Acquisition Core (RRID:SCR_021845), STEMCore Laboratories (RRID:SCR_012601), Genome Engineering and Molecular Biology (GEM) Core (RRID:SCR_022954), Animal Behaviour and Physiology Core (RRID:SCR_022882), Louise Pelletier Histology Core (RRID: SCR_021737). Figs. 1, 2, 6, and S4 were generated in part with Biorender.com.

Authors' contributions

Conceptualization: TRS, CEP, MWCR. Methodology: TRS, CEP, TTN, JLZ, VSG, PMM, BN, SMC, JR. Investigation: TRS, CEP, TTN, JLZ, MMH, ACG, VSG, PMM, BN, JR. Visualization: TRS, CEP, JLZ, MWCR. Funding acquisition: TRS, CEP, MWCR. Project administration: JMW, JR, MWCR. Supervision: JR, MWCR. Writing – original draft: TRS, MWCR. Writing – review & editing: TRS, MWCR.

Declarations

Competing interests

Authors declare that they have no competing interests.

Received: 13 June 2024 Accepted: 9 March 2025
Published online: 28 March 2025

References

1. Hipp MS, Kasturi P, Hartl FU. The proteostasis network and its decline in ageing. Nat Rev Mol Cell Biol. 2019;20(7):421–35.
2. Spires-Jones TL, Attems J, Thal DR. Interactions of pathological proteins in neurodegenerative diseases. Acta Neuropathol. 2017;134(2):187–205.
3. Hardiman O, Al-Chalabi A, Chio A, Corr EM, Logroscino G, Robberecht W, Shaw PJ, Simmons Z, Van Den Berg LH. Amyotrophic lateral sclerosis. Nat Rev Dis Primers. 2017;3(1):1–19.
4. Grossman M, Seeley WW, Boxer AL, et al. Frontotemporal lobar degeneration. Nat Rev Dis Primers. 2023;9(1):1–19.
5. Burrell JR, Halliday GM, Kril JJ, Ittner LM, Götz J, Kiernan MC, Hodges JR. The frontotemporal dementia-motor neuron disease continuum. Lancet. 2016;388:919–31.
6. Nelson PT, Dickson DW, Trojanowski JQ, et al. Limbic-predominant age-related TDP-43 encephalopathy (LATE): consensus working group report. Brain. 2019;142:1503–27.
7. Meneses A, Koga S, O'Leary J, Dickson DW, Bu G, Zhao N. TDP-43 pathology in Alzheimer's disease. Mol Neurodegener. 2021;16(1):1–15.
8. Nicks R, Clement NF, Alvarez VE, et al. Repetitive head impacts and chronic traumatic encephalopathy are associated with TDP-43 inclusions and hippocampal sclerosis. Acta Neuropathol. 2023;145:395–408.
9. Thammisetty SS, Pedragosa J, Weng YC, Calon F, Planas A, Kriz J. Age-related deregulation of TDP-43 after stroke enhances NF-κB-mediated inflammation and neuronal damage. J Neuroinflammation. 2018;15:1–15.
10. Coyne AN, Baskerville V, Zaepfel BL, Dickson DW, Rigo F, Bennett F, Patrick Lusk C, Rothstein JD. Nuclear accumulation of CHMP7 initiates nuclear pore complex injury and subsequent TDP-43 dysfunction in sporadic and familial ALS. Sci Transl Med. 2021;13:1923.
11. Suk TR, Rousseaux MWC. The role of TDP-43 mislocalization in amyotrophic lateral sclerosis. Mol Neurodegener. 2020;15:45.
12. Ma XR, Prudencio M, Koike Y, et al. TDP-43 represses cryptic exon inclusion in the FTD–ALS gene UNC13A. Nature. 2022;603(7899):124–30.
13. Brown AL, Wilkins OG, Keuss MJ, et al. TDP-43 loss and ALS-risk SNPs drive mis-splicing and depletion of UNC13A. Nature. 2022;603(7899):131–7.
14. Melamed Z, López-Erauskin J, Baughn MW, et al. Premature polyadenylation-mediated loss of stathmin-2 is a hallmark of TDP-43-dependent neurodegeneration. Nat Neurosci. 2019;22:180–90.
15. Klim JR, Williams LA, Limone F, et al. ALS-implicated protein TDP-43 sustains levels of STMN2, a mediator of motor neuron growth and repair. Nat Neurosci. 2019;22:167–79.
16. Gasset-Rosa F, Lu S, Yu H, Chen C, Melamed Z, Guo L, Shorter J, Da Cruz S, Cleveland DW. Cytoplasmic TDP-43 De-mixing independent of stress granules drives inhibition of nuclear import, loss of nuclear TDP-43, and cell death. Neuron. 2019;102:339-357.e7.

17. Baughn MW, Melamed Z, López-Erauskin J, et al. Mechanism of STMN2 cryptic splice-polyadenylation and its correction for TDP-43 proteinopathies. Science (1979). 2023;379:1140–9.
18. Agra Almeida Quadros AR, Li Z, Wang X, et al. Cryptic splicing of stathmin-2 and UNC13A mRNAs is a pathological hallmark of TDP-43-associated Alzheimer's disease. Acta Neuropathol. 2024;147(1):1–18.
19. Spence H, Waldron FM, Saleeb RS, et al. RNA aptamer reveals nuclear TDP-43 pathology is an early aggregation event that coincides with STMN-2 cryptic splicing and precedes clinical manifestation in ALS. Acta Neuropathol. 2024;147:1–15.
20. Hergesheimer RC, Chami AA, De Assis DR, Vourc'h P, Andres CR, Corcia P, Lanznaster D, Blasco H. The debated toxic role of aggregated TDP-43 in amyotrophic lateral sclerosis: a resolution in sight? Brain. 2019;142:1176–94.
21. Zou ZY, Zhou ZR, Che CH, Liu CY, He RL, Huang HP. Genetic epidemiology of amyotrophic lateral sclerosis: a systematic review and meta-analysis. J Neurol Neurosurg Psychiatry. 2017;88:540–9.
22. Ghasemi M, Brown RH. Genetics of amyotrophic lateral sclerosis. Cold Spring Harb Perspect Med. 2018. https://doi.org/10.1101/CSHPERSPECT.A024125.
23. Mackenzie IR, Nicholson AM, Sarkar M, et al. TIA1 mutations in amyotrophic lateral sclerosis and frontotemporal dementia promote phase separation and alter stress granule dynamics. Neuron. 2017;95:808-816.e9.
24. Walker AK, Soo KY, Sundaramoorthy V, et al. ALS-associated TDP-43 induces endoplasmic reticulum stress, which drives cytoplasmic TDP-43 accumulation and stress granule formation. PLoS One. 2013;8: e81170.
25. Tam OH, Rozhkov NV, Shaw R, et al. Postmortem cortex samples identify distinct molecular subtypes of ALS: retrotransposon activation, oxidative stress, and activated glia. Cell Rep. 2019;29:1164-1177.e5.
26. Wolozin B, Ivanov P. Stress granules and neurodegeneration. Nat Rev Neurosci. 2019;20:649–66.
27. Lin MT, Beal MF. Mitochondrial dysfunction and oxidative stress in neurodegenerative diseases. Nature. 2006;443:787–95.
28. Ratti A, Gumina V, Lenzi P, et al. Chronic stress induces formation of stress granules and pathological TDP-43 aggregates in human ALS fibroblasts and iPSC-motoneurons. Neurobiol Dis. 2020;145: 105051.
29. D'Amico E, Factor-Litvak P, Santella RM, Mitsumoto H. Clinical perspective on oxidative stress in sporadic amyotrophic lateral sclerosis. Free Radic Biol Med. 2013;65:509–27.
30. Colombrita C, Zennaro E, Fallini C, Weber M, Sommacal A, Buratti E, Silani V, Ratti A. TDP-43 is recruited to stress granules in conditions of oxidative insult. J Neurochem. 2009;111:1051–61.
31. Zuo X, Zhou J, Li Y, et al. TDP-43 aggregation induced by oxidative stress causes global mitochondrial imbalance in ALS. Nat Struct Mol Biol. 2021;28(2):132–42.
32. Ueda T, Takeuchi T, Fujikake N, et al. Dysregulation of stress granule dynamics by DCTN1 deficiency exacerbates TDP-43 pathology in Drosophila models of ALS/FTD. Acta Neuropathol Commun. 2024;12:1–15.
33. Iguchi Y, Katsuno M, Takagi S, Ishigaki S, Niwa J, Hasegawa M, Tanaka F, Sobue G. Oxidative stress induced by glutathione depletion reproduces pathological modifications of TDP-43 linked to TDP-43 proteinopathies. Neurobiol Dis. 2012;45:862–70.
34. Liu-Yesucevitz L, Bilgutay A, Zhang YJ, et al. Tar DNA binding protein-43 (TDP-43) associates with stress granules: analysis of cultured cells and pathological brain tissue. PLoS One. 2010;5:e13250.
35. McDonald KK, Aulas A, Destroismaisons L, Pickles S, Beleac E, Camu W, Rouleau GA, Vande VC. TAR DNA-binding protein 43 (TDP-43) regulates stress granule dynamics via differential regulation of G3BP and TIA-1. Hum Mol Genet. 2011;20:1400–10.
36. Luan W, Wright AL, Brown-Wright H, Le S, San Gil R, Madrid San Martin L, Ling K, Jafar-Nejad P, Rigo F, Walker AK. Early activation of cellular stress and death pathways caused by cytoplasmic TDP-43 in the rNLS8 mouse model of ALS and FTD. Mol Psychiatry. 2023;28(6):2445–61.
37. Fung G, Shi J, Deng H, Hou J, Wang C, Hong A, Zhang J, Jia W, Luo H. Cytoplasmic translocation, aggregation, and cleavage of TDP-43 by enteroviral proteases modulate viral pathogenesis. Cell Death, Differentiation. 2015;22(12):2087–97.
38. Ash PEA, Stanford EA, Al Abdulatif A, et al. Dioxins and related environmental contaminants increase TDP-43 levels. Mol Neurodegener. 2017;12:1–14.
39. Dubinski A, Gagne M, Peyrard S, Gordon D, Talbot K, Vande Velde C. Stress granule assembly in vivo is deficient in the CNS of mutant TDP-43 ALS mice. Hum Mol Genet. 2023;32:319–32.
40. Odierna GL, Vucic S, Dyer M, Dickson T, Woodhouse A, Blizzard C. How do we get from hyperexcitability to excitotoxicity in amyotrophic lateral sclerosis? Brain. 2024;147:1610–21.
41. Zhang P, Fan B, Yang P, Temirov J, Messing J, Kim HJ, Taylor JP. Chronic optogenetic induction of stress granules is cytotoxic and reveals the evolution of ALS-FTD pathology. Elife. 2019. https://doi.org/10.7554/eLife.39578.
42. Neumann M, Kwong LK, Lee EB, et al. Phosphorylation of S409/410 of TDP-43 is a consistent feature in all sporadic and familial forms of TDP-43 proteinopathies. Acta Neuropathol. 2009;117:137–49.
43. Neumann M, Sampathu DM, Kwong LK, et al. Ubiquitinated TDP-43 in frontotemporal lobar degeneration and amyotrophic lateral sclerosis. Science (1979). 2006;314:130–3.
44. Arai T, Hasegawa M, Akiyama H, et al. TDP-43 is a component of ubiquitin-positive tau-negative inclusions in frontotemporal lobar degeneration and amyotrophic lateral sclerosis. Biochem Biophys Res Commun. 2006;351:602–11.
45. Necarsulmer J, Simon J, Evangelista B, et al. RNA-binding deficient TDP-43 drives cognitive decline in a mouse model of TDP-43 proteinopathy. Elife. 2023. https://doi.org/10.7554/ELIFE.85921.2.
46. McGurk L, Gomes E, Guo L, Mojsilovic-Petrovic J, Tran V, Kalb RG, Shorter J, Bonini NM. Poly(ADP-Ribose) prevents pathological phase separation of TDP-43 by promoting liquid demixing and stress granule localization. Mol Cell. 2018;71:703-717.e9.
47. Henley JM, Craig TJ, Wilkinson KA. Neuronal SUMOylation: mechanisms, physiology, and roles in neuronal dysfunction. Physiol Rev. 2014;94:1249–85.
48. Wilkinson KA, Henley JM. Mechanisms, regulation and consequences of protein SUMOylation. Biochem J. 2010;428:133–45.
49. Maraschi AM, Gumina V, Dragotto J, Colombrita C, Mompean M, Buratti E, Silani V, Feligioni M, Ratti A. SUMOylation regulates TDP-43 splicing activity and nucleocytoplasmic distribution. Mol Neurobiol. 2021;58:5682–702.
50. Maurel C, Chami AA, Thépault RA, Marouillat S, Blasco H, Corcia P, Andres CR, Vourc'h P. A role for SUMOylation in the formation and cellular localization of TDP-43 aggregates in amyotrophic lateral sclerosis. Mol Neurobiol. 2020;57:1361–73.
51. Marino R, Buccarello L, Hassanzadeh K, Akhtari K, Palaniappan S, Corbo M, Feligioni M. A novel cell-permeable peptide prevents protein SUMOylation and supports the mislocalization and aggregation of TDP-43. Neurobiol Dis. 2023;188: 106342.
52. Pichler A, Melchior F. Ubiquitin-related modifier SUMO1 and nucleocytoplasmic transport. Traffic. 2002;3:381–7.
53. Wang L, Wansleeben C, Zhao S, Miao P, Paschen W, Yang W. SUMO 2 is essential while SUMO 3 is dispensable for mouse embryonic development. EMBO Rep. 2014;15:878–85.
54. Enserink JM. Sumo and the cellular stress response. Cell Div. 2015;10:1–13.
55. Seyfried NT, Gozal YM, Dammer EB, Xia Q, Duong DM, Cheng D, Lah JJ, Levey AI, Peng J. Multiplex SILAC analysis of a cellular TDP-43 proteinopathy model reveals protein inclusions associated with SUMOylation and diverse polyubiquitin chains. Mol Cell Proteomics. 2010;9:705–18.
56. Dammer EB, Fallini C, Gozal YM, et al. Coaggregation of RNA-binding proteins in a model of TDP-43 proteinopathy with selective RGG motif methylation and a role for RRM1 ubiquitination. PLoS One. 2012. https://doi.org/10.1371/JOURNAL.PONE.0038658.
57. Dewey CM, Cenik B, Sephton CF, Dries DR, Mayer P, Good SK, Johnson BA, Herz J, Yu G. TDP-43 is directed to stress granules by sorbitol, a novel physiological osmotic and oxidative stressor. Mol Cell Biol. 2011;31:1098–108.
58. Chang HY, Hou SC, Der WT, Wong CH, Wang IF. Heat-shock protein dysregulation is associated with functional and pathological TDP-43 aggregation. Nat Commun. 2013;4:1–11.
59. Suk TR, Nguyen TT, Fisk ZA, et al. Characterizing the differential distribution and targets of Sumo1 and Sumo2 in the mouse brain. iScience. 2023;26:106350.

60. Lu J, Wu T, Zhang B, Liu S, Song W, Qiao J, Ruan H. Types of nuclear localization signals and mechanisms of protein import into the nucleus. Cell Commun Signal. 2021;19:1–10.
61. Lange A, Mills RE, Devine SE, Corbett AH. A PY-NLS nuclear targeting signal is required for nuclear localization and function of the saccharomyces cerevisiae mRNA-binding protein Hrp1. J Biol Chem. 2008;283:12926–34.
62. Sun Y, Zhao K, Xia W, et al. The nuclear localization sequence mediates hnRNPA1 amyloid fibril formation revealed by cryoEM structure. Nat Commun. 2020;11(1):1–8.
63. Mann JR, Gleixner AM, Mauna JC, et al. RNA binding antagonizes neurotoxic phase transitions of TDP-43. Neuron. 2019;102:321–338.e8.
64. Kelten-Schmitz J, Wagner K, Piller T, Kaulich M, Alberti S, Müller S. The nuclear SUMO-targeted ubiquitin quality control network regulates the dynamics of cytoplasmic stress granules. Mol Cell. 2020;79:54–67.e7.
65. Kagey MH, Melhuish TA, Wotton D. The polycomb protein Pc2 is a SUMO E3. Cell. 2003;113:127–37.
66. García-Gutiérrez P, Juárez-Vicente F, Gallardo-Chamizo F, Charnay P, García-Domínguez M. The transcription factor Krox20 is an E3 ligase that sumoylates Its Nab coregulators. EMBO Rep. 2011;12:1018–23.
67. Oh SM, Liu Z, Okada M, Jang SW, Liu X, Chan CB, Luo H, Ye K. Ebp1 sumoylation, regulated by TLS/FUS E3 ligase, is required for its antiproliferative activity. Oncogene. 2009;29(7):1017–30 2010.
68. Eisenhardt N, Chaugule VK, Koidl S, et al. A new vertebrate SUMO enzyme family reveals insights into SUMO-chain assembly. Nature Structural, Molecular Biology. 2015;22(12):959–67.
69. Payne F, Colnaghi R, Rocha N, et al. Hypomorphism in human NSMCE2 linked to primordial dwarfism and insulin resistance. J Clin Invest. 2014;124:4028–38.
70. Kahyo T, Nishida T, Yasuda H. Involvement of PIAS1 in the sumoylation of tumor suppressor p53. Mol Cell. 2001;8:713–8.
71. Kotaja N, Karvonen U, Jänne OA, Palvimo JJ. PIAS proteins modulate transcription factors by functioning as SUMO-1 Ligases. Mol Cell Biol. 2002;22:5222–34.
72. Nakagawa K, Yokosawa H. PIAS3 Induces SUMO-1 modification and transcriptional repression of IRF-1. FEBS Lett. 2002;530:204–8.
73. Sachdev S, Bruhn L, Sieber H, Pichler A, Melchior F, Grosschedl R. PIASy, a nuclear matrix–associated SUMO E3 ligase, represses LEF1 activity by sequestration into nuclear bodies. Genes Dev. 2001;15:3088–103.
74. Chu Y, Yang X. SUMO E3 ligase activity of TRIM proteins. Oncogene. 2010;30(9):1108–16 2011.
75. Pichler A, Gast A, Seeler JS, Dejean A, Melchior F. The nucleoporin RanBP2 Has SUMO1 E3 ligase activity. Cell. 2002;108:109–20.
76. Reynolds A, Qiao H, Yang Y, et al. RNF212 is a dosage-sensitive regulator of crossing-over during mammalian meiosis. Nat Genet. 2013;45(3):269–78.
77. Liang Q, Deng H, Li X, Wu X, Tang Q, Chang T-H, Peng H, Rauscher FJ, Ozato K, Zhu F. Tripartite motif-containing protein 28 is a small ubiquitin-related modifier E3 ligase and negative regulator of IFN regulatory factor 7. J Immunol. 2011;187:4754–63.
78. Yamashita D, Moriuchi T, Osumi T, Hirose F. Transcription factor hDREF is a novel SUMO E3 ligase of MI2α*. J Biol Chem. 2016;291:11619–34.
79. Karvonen U, Jääskeläinen T, Rytinki M, Kaikkonen S, Palvimo JJ. ZNF451 is a novel PML body- and SUMO-associated transcriptional coregulator. J Mol Biol. 2008;382:585–600.
80. Warner LE, Mancias P, Butler IJ, McDonald CM, Keppen L, Koob KG, Lupski JR. Mutations in the early growth response 2 (EGR2) gene are associated with hereditary myelinopathies. Nat Genet. 1998;18(4):382–4.
81. Nishida T, Yasuda H. PIAS1 and PIASxα function as SUMO-E3 ligases toward androgen receptor and repress androgen receptor-dependent transcription. J Biol Chem. 2002;277:41311–7.
82. Zhao Q, Xie Y, Zheng Y, Jiang S, Liu W, Mu W, Liu Z, Zhao Y, Xue Y, Ren J. GPS-SUMO: a tool for the prediction of sumoylation sites and SUMO-interaction motifs. Nucleic Acids Res. 2014;42:W325–30.
83. Ren J, Gao X, Jin C, Zhu M, Wang X, Shaw A, Wen L, Yao X, Xue Y. Systematic study of protein sumoylation: development of a site-specific predictor of SUMOsp 2.0. Proteomics. 2009;9:3409–12.
84. Lumpkin RJ, Gu H, Zhu Y, Leonard M, Ahmad AS, Clauser KR, Meyer JG, Bennett EJ, Komives EA. Site-specific identification and quantitation of endogenous SUMO modifications under native conditions. Nat Commun. 2017;8(1):1–11.
85. Hendriks IA, Lyon D, Su D, Skotte NH, Daniel JA, Jensen LJ, Nielsen ML. Site-specific characterization of endogenous SUMOylation across species and organs. Nat Commun. 2018;9(1):1–17.
86. Chen S, Francioli LC, Goodrich JK, et al. A genomic mutational constraint map using variation in 76,156 human genomes. Nature. 2023;625(7993):92–100.
87. Kraemer BC, Schuck T, Wheeler JM, Robinson LC, Trojanowski JQ, Lee VMY, Schellenberg GD. Loss of Murine TDP-43 disrupts motor function and plays an essential role in embryogenesis. Acta Neuropathol. 2010;119:409–19.
88. Khalfallah Y, Kuta R, Grasmuck C, Prat A, Durham HD, Vande Velde C. TDP-43 regulation of stress granule dynamics in neurodegenerative disease-relevant cell types. Sci Rep. 2018;8:7551.
89. Sidibé H, Khalfallah Y, Xiao S, et al. TDP-43 stabilizes G3BP1 mRNA: relevance to amyotrophic lateral sclerosis/frontotemporal dementia. Brain. 2021. https://doi.org/10.1093/brain/awab217.
90. Shelkovnikova TA, Kukharsky MS, An H, Dimasi P, Alexeeva S, Shabir O, Heath PR, Buchman VL. Protective paraspeckle hyper-assembly downstream of TDP-43 loss of function in amyotrophic lateral sclerosis. Mol Neurodegener. 2018;13:1–17.
91. Wang C, Duan Y, Duan G, et al. Stress Induces dynamic, cytotoxicity-antagonizing TDP-43 nuclear bodies via paraspeckle LncRNA NEAT1-mediated liquid-liquid phase separation. Mol Cell. 2020;79:443-458.e7.
92. Yu H, Lu S, Gasior K, et al. HSP70 chaperones RNA-free TDP-43 into anisotropic intranuclear liquid spherical shells. Science (1979). 1979. https://doi.org/10.1126/SCIENCE.ABB4309/SUPPL_FILE/ABB4309_YU_SM.PDF.
93. Geertsma HM, Suk TR, Ricke KM, Horsthuis K, Parmasad JLA, Fisk ZA, Callaghan SM, Rousseaux MWC. Constitutive nuclear accumulation of endogenous alpha-synuclein in mice causes motor impairment and cortical dysfunction, independent of protein aggregation. Hum Mol Genet. 2022;31:3613–28.
94. Yu B, Pamphlett R. Environmental insults: critical triggers for amyotrophic lateral sclerosis. Transl Neurodegener. 2017;6:1–10.
95. Kirola L, Mukherjee A, Mutsuddi M. Recent updates on the genetics of amyotrophic lateral sclerosis and frontotemporal dementia. Mol Neurobiol. 2022;59(9):5673–94.
96. Wang A, Conicella AE, Schmidt HB, et al. A single N-terminal phosphomimic disrupts TDP-43 polymerization, phase separation, and RNA splicing. EMBO J. 2018;37: e97452.
97. Brady OA, Meng P, Zheng Y, Mao Y, Hu F. Regulation of TDP-43 aggregation by phosphorylation andp62/SQSTM1. J Neurochem. 2011;116:248–59.
98. Wegorzewska I, Bell S, Cairns NJ, Miller TM, Baloh RH. TDP-43 mutant transgenic mice develop features of ALS and frontotemporal lobar degeneration. Proc Natl Acad Sci U S A. 2009;106:18809–14.
99. Campbell KM, Xu Y, Patel C, et al. Loss of TDP-43 in male germ cells causes meiotic failure and impairs fertility in mice. J Biol Chem. 2021. https://doi.org/10.1016/j.jbc.2021.101231.
100. Milstead RA, Link CD, Xu Z, Hoeffer CA. TDP-43 knockdown in mouse model of ALS leads to dsRNA deposition, gliosis, and neurodegeneration in the spinal cord. Cerebral Cortex (New York, NY). 2023;33:5808.
101. Yang C, Qiao T, Yu J, et al. Low-level overexpression of wild type TDP-43 causes late-onset, progressive neurodegeneration and paralysis in mice. PLoS One. 2022;17:e0255710.
102. Buratti E. TDP-43 post-translational modifications in health and disease. Expert Opin Ther Targets. 2018. https://doi.org/10.1080/14728222.2018.1439923.
103. Chatterjee M, Özdemir S, Fritz C, et al. Plasma extracellular vesicle tau and TDP-43 as diagnostic biomarkers in FTD and ALS. Nat Med. 2024;30(6):1771–83.
104. Feiler MS, Strobel B, Freischmidt A, et al. TDP-43 is intercellularly transmitted across axon terminals. J Cell Biol. 2015;211:897–911.
105. Iguchi Y, Eid L, Parent M, et al. Exosome secretion is a key pathway for clearance of pathological TDP-43. Brain. 2016;139:3187–201.
106. Leibiger C, Deisel J, Aufschnaiter A, Ambros S, Tereshchenko M, Verheijen BM, Büttner S, Braun RJ. TDP-43 controls lysosomal pathways thereby determining its own clearance and cytotoxicity. Hum Mol Genet. 2018;27:1593–607.

107. Liu G, Byrd A, Warner AN, Pei F, Basha E, Buchanan A, Buchan JR. Cdc48/VCP and endocytosis regulate TDP-43 and FUS toxicity and turnover. Mol Cell Biol. 2019. https://doi.org/10.1128/mcb.00256-19.
108. Liu G, Coyne AN, Pei F, Vaughan S, Chaung M, Zarnescu DC, Buchan JR. Endocytosis regulates TDP-43 toxicity and turnover. Nat Commun. 2017;8:2092.
109. Scotter EL, Vance C, Nishimura AL, et al. Differential roles of the ubiquitin proteasome system and autophagy in the clearance of soluble and aggregated TDP-43 species. J Cell Sci. 2014;127:1263–78.
110. Wang X, Fan H, Ying Z, Li B, Wang H, Wang G. Degradation of TDP-43 and its pathogenic form by autophagy and the ubiquitin-proteasome system. Neurosci Lett. 2010;469:112–6.
111. Yau TY, Molina O, Courey AJ. SUMOylation in development and neurodegeneration. Development. 2020. https://doi.org/10.1242/DEV.175703.
112. Princz A, Tavernarakis N. The role of SUMOylation in ageing and senescent decline. Mech Ageing Dev. 2017;162:85–90.
113. White MA, Kim E, Duffy A, et al. TDP-43 gains function due to perturbed autoregulation in a Tardbp knock-in mouse model of ALS-FTD. Nat Neurosci. 2018;21:1138.
114. Fratta P, Sivakumar P, Humphrey J, et al. Mice with endogenous TDP-43 mutations exhibit gain of splicing function and characteristics of amyotrophic lateral sclerosis. EMBO J. 2018. https://doi.org/10.15252/embj.201798684.
115. Abramson J, Adler J, Dunger J, et al. Accurate structure prediction of biomolecular interactions with AlphaFold 3. Nature. 2024;630(8016):493–500.
116. Dereeper A, Guignon V, Blanc G, et al. Phylogeny.fr: robust phylogenetic analysis for the non-specialist. Nucleic Acids Res. 2008;36:W465–9.
117. Gertsenstein M, Nutter LMJ. Engineering point mutant and epitope-tagged alleles in mice using Cas9 RNA-guided nuclease. Curr Protoc Mouse Biol. 2018;8:28–53.
118. Miedel CJ, Patton JM, Miedel AN, Miedel ES, Levenson JM. Assessment of spontaneous alternation, novel object recognition and limb clasping in transgenic mouse models of amyloid-β and tau neuropathology. JoVE (Journal of Visualized Experiments). 2017;2017:e55523.
119. Guyenet SJ, Furrer SA, Damian VM, Baughan TD, la Spada AR, Garden GA. A simple composite phenotype scoring system for evaluating mouse models of cerebellar ataxia. J Vis Exp. 2010;39:e1787.
120. Lê S, Josse J, Husson F. FactoMineR: an R package for multivariate analysis. J Stat Softw. 2008;25:1–18.
121. Alboukadel K, Fabian M. Extract and visualize the results of multivariate data analyses [R package factoextra version 1.0.7]. 2020. https://CRAN.R-project.org/package=factoextra. Accessed 8 Apr 2024.

Publisher's Note